Master's thesis

NTNU
Norwegian University of Science and Technology
Faculty of Natural Sciences
Department of Materials Science and Engineering

Martha Seim Gunstad

Development of Piezoelectric Composite Ceramic Coatings on Metal Substrates for Biomedical Applications

Master's thesis in Chemical Engineering and Biotechnology
Supervisor: Julia Glaum
Co-supervisor: Freya Sofia Andersen
June 2022

NTNU
Norwegian University of Science and Technology

Martha Seim Gunstad

Development of Piezoelectric Composite Ceramic Coatings on Metal Substrates for Biomedical Applications

Master's thesis in Chemical Engineering and Biotechnology
Supervisor: Julia Glaum
Co-supervisor: Freya Sofia Andersen
June 2022

Norwegian University of Science and Technology
Faculty of Natural Sciences
Department of Materials Science and Engineering

NTNU
Norwegian University of
Science and Technology

Preface

This Master's Thesis is written as a part of the course *TMT 4900 - Materials Chemistry and Energy Technology, Master's Thesis* at the Norwegian University of Science and Technology (NTNU). The thesis finishes the Master's degree program Chemical Engineering and Biotechnology. The work was carried out from January to June 2022. The work has been done in collaboration with the Nordic Institute of Dental Materials (NIOM) in Oslo. It is a continuation of the specialisation project *Development of piezoelectric composite ceramic materials on metal substrates for biomedical application* from January 2022. The work has been supervised by professor Julia Glaum (IMA, NTNU), with Freya Sofia Andersen (NIOM) as a co-supervisor.

XRD measurements have been performed by PhD candidate Viviann Hole Pedersen and PhD candidate Caitlin Guzzo. The samples were prepared by the author prior to the measurements. All other work presented in this study has been carried out be the author at the Department of Materials Science and Engineering (IMA) at NTNU and at NIOM in Oslo.

Acknowledgements

I would first like to extend my deepest gratitude to my supervisor Julia Glaum and co-supervisor Freya Sofia Andersen for their guidance, encouragement and input. You have always been available for my questions, both in our weekly meetings and whenever new questions popped up. Your knowledge, patience and experience have been invaluable. Thank you for taking the time to help with experimental work, answering questions and providing feedback. I have greatly appreciated our weekly meetings and conversations.

I would also like to thank the Biomedical ceramics group and the FACET group at IMA for our weekly meetings. These meetings have been a great opportunity to discuss research and connect with other professors, post docs, PhD students, and master students at the department. I appreciate the good social environment and the many opportunities to present my work, ask questions and get feedback from you all. I would also like to thank the technical staff and engineers at the Department of Materials Science and Engineering for training and assistance in the experimental work. I also have to thank everyone at NIOM who welcomed me and have been of great help in the experimental work. A special thank you to Heidi Holm at NIOM for help, training on working with porcelains, patience, insightful explanations and her interest in my work.

Finally I would like to thank my friends for their support, our conversations, our daily lunch breaks (and some dinner breaks), and for five great years at NTNU. Thank you also to my family for always being supportive, encouraging and cheering me on.

Abstract

The healing of damaged bones can be promoted by increasing the bone growth using electrical stimulation. This electrical stimulation can be applied by using piezoelectric implant materials. Piezoelectric ceramics lack the mechanical properties necessary for implant materials. On the other hand, metallic implants have the mechanical properties but lack the piezoelectric properties of the ceramics. Piezoelectric coatings on metal substrates are therefore considered in order to combine these properties. However, densification of ceramics requires high temperatures, which can damage the metal substrates. Combining the piezoelectric ceramic with dental porcelains is thought the make dense piezoelectric coatings possible at lower temperatures. This is because dental porcelains fused to metals is a system which has been successfully used for dental restorations for decades.

In this study, two calcium and zirconium doped barium titanate (BCZT) powders have been used together with dental porcelains to prepare BCZT/porcelain coatings on Ti-6Al-4V substrates. The BCZT powders have been prepared through solid-state synthesis, resulting in two powders of different particle sizes. The effect of different amounts and different particle sizes of BCZT on the coatings have been evaluated. The procedure used for dental restorations in porcelains on metal has been adapted for the preparation of these coatings.

The porosity of the BCZT/porcelain coatings increased as the amount of BCZT powder was increased. Smaller BCZT particles resulted in a higher amount of pores compared to larger particles. The bond strength of the coatings was found to be highest for coatings with 40 wt% BCZT powder. The dielectric response of the coatings improved with increasing amounts of BCZT powder. However, it was not possible to measure the piezoelectric response of these coatings.

Further improvements can be made to the coating procedure and the material system. This can increase the bond strength and piezoelectric properties of the coatings. Still, these results are promising for the use of BCZT/porcelain coatings for implant materials.

Sammendrag

Helbredelse av skadede ben kan forbedres ved å øke benveksten. Dette kan gjøres ved hjelp av elektrisk stimulering. Piezoelektriske implantatmaterialer er en mulighet for å oppnå denne stimuleringen. Piezoelektriske keramer har ikke de nødvendige mekaniske egenskapene for implantatmaterialer. På den andre siden har metaller de mekaniske egenskapene, men ikke de piezoelektriske egenskapene. Piezoelektriske belegg på metallsubstrater er derfor en måte å kombinere disse egenskapene. Keramer må generelt sintres ved høye temperaturer for å oppnå tilstrekkelig lav porøsitet. De høye temperaturene kan ha en negativ effekt på metallsubstratet. Ved å kombinere piezoelektriske keramer med porselen kan det være mulig å lage tette piezoelektriske belegg ved lavere temperaturer. Porselen smeltet til metall er et materialsystem som har blitt brukt til tannrestaureringer i flere tiår.

I denne masteroppgaven har to bariumtitanat pulver dopet med kalsium og zirkonium (BCZT) blitt kombinert med porselen for å lage BCZT/porselensbelegg på Ti-6Al-4V substrater. BCZT-pulverne har blitt fremstilt via faststoffsyntese, og to ulike partikkelstørrelser ble fremstilt. Effekten av ulike mengder og partikkelstørrelser av BCZT-pulver på disse beleggene har blitt undersøkt. Prosedyren som er blitt brukt til å lage beleggene har tatt utgangspunkt i metodene tannteknikere bruker når de jobber med porselen på metall.

Porøsiteten i BCZT/porselensbeleggene økte med økt mengde BCZT-pulver. Mindre BCZT-partikler resulterte i flere porer enn det større BCZT-partikler gjorde. Bindingsstyrken var høyest for beleggene med 40 vt% BCZT-pulver. Den dielektriske responsen forbedret seg med økende mengde BCZT-pulver. Det var imidlertid ikke mulig å måle den piezoelektriske responsen til beleggene.

Prosedyren for å lage beleggene og materialsystemet kan forbedres. Dette kan lede til økt bindingsstyrke og forbedrede piezoelektriske egenskaper i beleggene. Resultatene av denne oppgaven er likevel lovende for bruk av BCZT/porselensbelegg til implantatmaterialer.

Table of Contents

List of Figures

List of Tables

1 Introduction

1.1 Background and Motivation

There has been an increasing need for medical implants in the last decades, a trend that is expected to continue partly because of an aging population. As of 2007, around 500 000 total hip and knee joint replacements were done annually in Europe and the United States. Medical implants have a limited lifetime and will need to be replaced after some time.[1] A total hip prosthesis will for example, on average need to be replaced every 15 years.[2] By getting these implants earlier in life, the need for replacements will increase. Replacement of existing implants amounted to approximately one quarter of the hip and knee joint surgeries in 2007. Because of this the development of implants is becoming more important, with a focus on durability especially.[3] An improvement of these implants could reduce the need for replacement surgeries, which would improve the patients quality of life as well as save on healthcare costs.[1]

Materials have been used to promote healing and restoration of damaged tissue for a long time. Around 4000 years ago linen thread was used to help heal wounds in Egypt and bamboo sticks were used as dental implants in China. Still, it is only in the last 150 years that there has been a systematic examination of how the body reacts to implanted materials.[2] The first metallic implant was a stainless steel alloy, introduced in the 1920's. This was followed by materials with low degrees of corrosion, then 316L stainless steel, cobalt alloys and titanium alloys. These materials were tolerated well by the body while at the same time having desirable mechanical properties. There are a couple of drawbacks with metals as implant materials. Generally, they do not form chemical bonds with the surrounding living tissue. This means that they do not form strong bonds with the tissue. Some metals have also been found to release metal ions while implanted, which could be toxic.[3]

When working with implants it is useful to define a couple concepts. Firstly, one definition of a biomaterial is *"A biomaterial is a nonviable material used in a medical device, intended to interact with biological systems."* (Williams, 1987).[4]The important property biocompatibility is defined as *"Biocompatibility" is the ability of a material to perform with an appropriate host response in a specific application.* (Williams, 1987).[4] This means that biomaterials are designed to perform a function while in the body, and that they are to be tolerated by the body. They should for example not elicit an inflammatory response in the surrounding tissue.

Biomaterials can be classified into three categories, or generations, based on their properties. The first generation of biomaterials include bioinert materials, where the materials ideally do not trigger a response in the immune system and the foreign body reaction is minimal. Second generation biomaterials are bioactive and biodegradable, which means that they can interact with the environment to improve bonding between the material and the surrounding tissue, for example. One of the most common causes for implant failure is that they loosen at the bone-implant interface. Improving the bonding can therefore reduce failure and increase durability of implants.[5] The third generation of biomaterials are designed with specific

cellular responses in mind. These materials can stimulate these processes at the molecular level. A comprehensive overview of biomaterials can be found in these review articles.[3] [6]

The use of ceramics came with the introduction of bioactive glass. Bioactive glass and other bioactive materials have the ability to chemically bond with human bones. Treatments with these materials have shown good results, but only for applications where there is little to no load.[3] Ceramic biomaterials are limited by their stiffness and brittle behaviour[2], which limits the use of ceramics in load-bearing applications. There are advantages and disadvantages with all material classes when used as a biomaterial. Combining different materials to achieve a material system with as many desirable properties as possible is therefore looked into. One such combination can be a metal, with its preferred mechanical properties, and a bioactive material. This can for example be done as a bioactive ceramic coating on a metal substrate.[3]

One application of biomaterials and implants is bone repair and regeneration. Bone is continuously remodelled to adapt to the current functional demand, and new bone will be formed to heal injuries. Even though bone is able to regenerate itself and heal, in 5-10% of patients problems can occur during the healing process. This can lead to pain and can affect the daily lives of the patients. By designing biomaterials that help promote the natural regeneration of bones, healing of fractured bones can be improved and the natural wear on surrounding bones caused by implants can be reduced.[7] [8]

It has been shown that mechanical stress can influence the normal remodelling and healing of fractures.[7] This stress results in generation of electrical potentials in the bones, where the potential is electronegative during compression and electropositive during tension. Formation of new bone occurs under electronegative potentials while bone resorption occurs under electropositive potentials. Bone is a piezoelectric material, which is why these potentials can be observed.[8] [9] These potentials were demonstrated already in the 1950s by Fukada and Yasuda.[10] Studies, done both *in vivo* and *in vitro*, have demonstrated that electrical stimulation is useful for healing of bones as it leads to proliferation of the bone cells.[9] [11] Piezoelectric materials generate a voltage when under mechanical stress. For piezoelectric implants the idea is that this will happen in the same way electrical potentials in bones are generated, i.e. by the movement of a human body. This means that by using piezoelectric implant materials it is possible to remove the need for an external energy source in order to apply electrical stimulation. Piezoelectric materials are therefore considered as materials with the potential to accelerate bone growth and healing.[11] [12]

A broad range of piezoelectric materials exists however, most of the commercially-available piezoelectrics are lead-based. Because of the toxicity of lead, these are avoided for biomedical applications. Barium titanate, and compositions based on it, provide alternatives to these lead-based materials. Barium calcium zirconium titanate (BCZT) have shown good piezoelectric properties, as well as being noncytotoxic. BCZT ceramics therefore have the potential to be used as biomaterials. Currently, the primary use of BCZT as a biomaterial is thought to be in regeneration of bone tissues.[11] [12] [13]

BCZT ceramics are, like most ceramics, brittle and would ideally be combined with

a metal substructure that could provide the necessary mechanical properties of implants. However, the high temperatures required to densify BCZT have a negative effect on the metal substructures. Ceramic-composite coatings with lower densification temperatures would therefore be beneficial for the development of piezoelectric coatings for biomedical applications.

1.2 Aim and Scope of the Work

The aim of this master thesis is to make dense ceramic-composite coatings for use on implants that are currently used to replace and repair hard tissue in the human body. The goal is that these coatings will stimulate bone growth and healing, thus improving the quality of life of the patients with hard-tissue implants. Hard tissue implants include bone and teeth implants. Ceramic-composite coatings have been chosen for their lower densification temperatures. Dental porcelains are biocompatible, have lower densification temperatures, and are used for metal-ceramic dental restorations. This makes them a good candidate for these coatings. The metal substrate used in this thesis is Ti-6Al-4V, as it is a commonly used implant material.

The scope of this thesis is to prepare ceramic-composite coatings on metal substrates and determine if this is a viable option for making piezoelectrically active and biocompatible coatings for had-tissue implants. This scope includes synthesis of a calcium/zirconium doped barium titanate (BCZT) powder and to make coatings with BCZT and dental porcelains on metal substrates, as well as characterisation of various properties. A standard application method used for preparing metal-ceramic restorations with porcelain is adapted and used to prepare these coatings. The work is done in collaboration with the Nordic Institute of Dental Materials (NIOM) in Oslo, Norway.

The bond strength and the piezoelectric properties of the coatings will be evaluated. In addition the coatings will be imaged using SEM, EDS and an XRD analysis will be performed. The BCZT powder will also be characterised with SEM, XRD, BET analysis and a PSD analysis to evaluate morphology, chemical composition and particle size distribution. Lastly, the BCZT powder will be pressed into pellets. The density and piezoelectric properties of these will be determined.

2 Theory

2.1 Dental Restorations

Dental restorations aim to fulfill both the functional and aesthetic needs of the patient. The restoration should have a normal contour, and restore the comfort, speech and health of the patient. The use of dental implants varies between countries, but for most countries a long term growth of 12 - 15% is expected.[14] There are multiple reasons for this increase, some of which are an aging population, tooth loss related to age, psychological aspects of tooth loss such as impacted self-confidence, as well as an increased public awareness. There are different types of dental restorations, some of which are shown in Figure 2.1. Another example is a fixed partial denture. This is commonly used for posterior missing teeth, i.e. the teeth in the back of the mouth. This denture can have three units, with one crown on each side of the missing tooth. A single missing tooth can also be replaced with a single-tooth implant.[14] These implants can be attached with screws, as shown in Figure 2.2, or directly to tooth substance. Screw-attached implants are built up of three components; the implant fixture, the abutment, and the restoration. The restoration, e.g. a porcelain crown, can be combined with the abutment. These porcelain crowns are often used in combination with a metal, crystalline ceramic or glass-ceramic.[15]

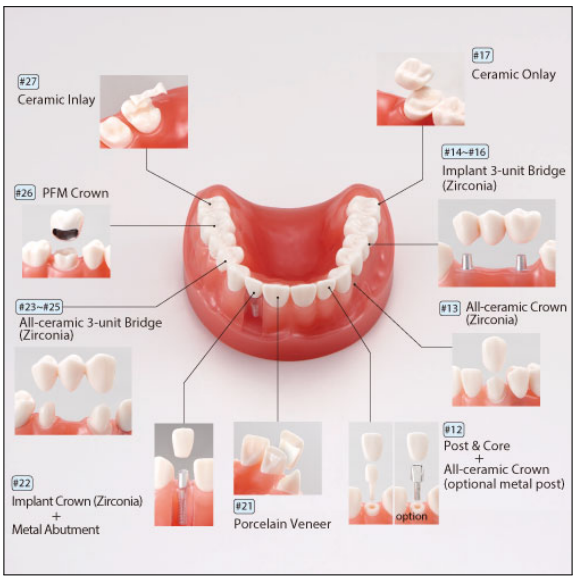

Figure 2.1: Examples of different dental restorations, here shown for ceramic materials.[16]

The field of dental materials and restorations has gone through an explosive evolution from the first porcelain dentures in 1774 to today's materials and techniques. The majority of the development has happened in the same time period, even though dental materials and technology has existed since approximately 700 BC. Duchateau and Dubois de Chemant both made porcelain dentures in 1774. Prior to this dental restorations had been in the form of ivory, animal teeth, human teeth and porcelain teeth.[17] [18] [19]

While the first porcelain dentures were made in 1774, it was not until 1838 that the colour and translucency of the porcelain matched that of natural teeth. The low strength of crowns and veneers made of porcelains made it difficult to use them for dental restorations. The introduction of PFM porcelain in the 1960s was important for the use of porcelain as a dental material as this provided the restorations with the necessary strength. PFM stands for Porcelain Fused to Metal. Porcelain veneers were introduced in the 1980s. Porcelain is still used for dental restorations and many of these are handmade.[18] [19]

Other developments have been made in addition to those related to porcelains. One important discovery was commercially pure titanium's ability to osseointegrate with natural bone, providing stability to the dental implant.[18] [19] New methods like the Computer Aided Design/Computer Aided Manufacturing (CAD/CAM) technique , LED curing and selective laser melting have all contributed to the development of the field of dental materials and restorations. In later years, polywave curing lights and 3D printing in dentistry have been introduced.[18] An introduction to some of the methods for producing dental restorations is given in the next section.

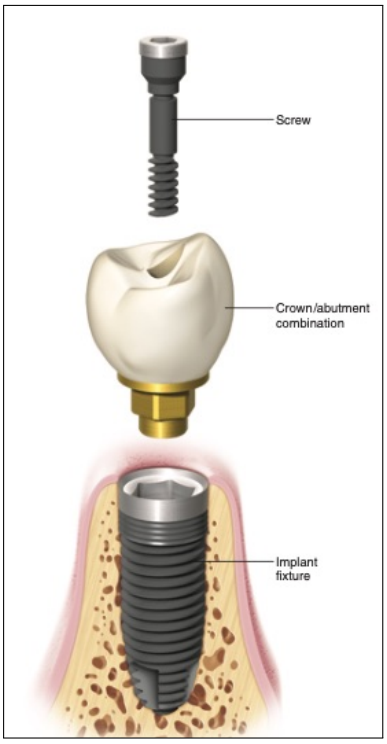

Figure 2.2: Illustration of a screw-retained single-tooth implant, where the abutment and the restoration are combined.[15]

2.1.1 Methods for Producing Dental Restorations

During the 1960s developments were made to dental feldspathic ceramics that made them suitable for dental restorations in spite of their low strength. There were two different approaches to the problem, but they both involved adding a second layer in the form of a substructure. The porcelain-jacket crown (PJC) was made by casting a metallic substructure, then firing a thin veneer of the ceramic placed on top of the substructure. Due to the mismatched coefficients of thermal expansion between the ceramic and the metal substructure, leucite was added to the feldspathic ceramic as this resulted in a closer match. An alternative substructure was made by high-strength ceramics. This was the result of adding alumina to the feldspathic ceramic. Minor modifications have been made to these systems since, and they are still in use today. Adding these substructures was an important development in terms of more aesthetic dental restorations.[18] [19] Optical properties such as colour and translucency of these feldspathic ceramics were improved with the introduction of vacuum firing as the porosity of the ceramics was reduced. These improvements were made in 1949 and 1838, respectively.[17]

Computer-aided design/computer-aided manufacturing (CAD/CAM) technology first entered the field of dental restoration in the 1980s. The technology was adapted from

other industries such as automotive and aerospace, as well as watch-making.[20] The first generation of this technology was only able to work with a two dimensional view of scanned images and the fabrication time was long. This has since improved, and the software makes it possible to render three dimensional scanned images and make adjustments. The fabrication time has also decreased significantly, with many systems being able to manufacture restorations in less than an hour. A scan of the patients teeth are made using an intraroal digital scanner. This makes it possible to replace traditional elastomeric impressions. However, a digital scan can also be made of these impressions.[21] There are currently more than 20 different CAD/CAM systems that have been introduced.[20]

The CAD/CAM technology can be used to manufacture frameworks in zirconia, alumina or metal, in addition to inlays, veneers and all-ceramic full-contour crowns.[20] Based on the digital scan a porous ceramic block is machined down into a core with the correct shape, but with slightly larger dimension. This is then sintered to achieve a dense structure. There is some shrinkage during sintering, which is why the original core is oversized.[18] Using ceramic blocks to create dental restorations of only one material eliminates the challenge of mismatched coefficients of thermal expansion.[21] Another advantage of this technology is that it automates parts of the process with dental restoration and can eliminate some of the more labour-intensive procedures. This also makes the methods more consistent and precise.[20]

Digital processing made it possible to create dental ceramics made of zirconia. The same method of machining an oversized shape from a porous block of yttria-stabilised zirconia followed by densification was used.[18] The use of high-strength zirconia ceramics as dental implant fixtures is a relatively new practice. Zirconia has advantages compared to both metals and to aluminium oxide. While with metallic implants there is a risk of ion release, zirconia shows minimal ion release and is considered to be inert. It is especially yttria-stabilised tetragonal zirconia that show better mechanical properties in terms of fracture resilience and fracture strength, compared to aluminium oxide.[15] Zirconia is therefore used to replace metals as a substructure material.[19]

A digital model from computer-aided design (CAD) is used to created 3D objects with additive manufacturing. Additive manufacturing is, like CAD/CAM, a technology with uses within different industries. It is used for applications in aerospace, art, medical, and defence industries. In dentistry additive manufacturing is used to create dentistry models personalized to each patient and can be used to prepare dental restorations.[22] [23]

Additive manufacturing can be divided into four categories: 1) extrusion printing, 2) inkjet printing, 3) laser melting/sintering, and 4) lithography printing. Extrusion printing is a process where the material is extruded through a nozzle. In inkjet printing polymer-based inks are deposited as droplets, and the final shape is built up layer by layer. Laser melting and sintering differs from these as the material is not deposited. A powder is instead sintered and new powder is added on top to create the next layer. Lithography printing uses light-sensitive polymers, which are subjected to light to create the desired structure.[22] [23] The methods used in dentistry are selective laser sintering (SLS) and stereolithography apparatus (SLA).

Using additive manufacturing methods could also result in more accurate dental restorations than by machining a larger block of material into the desired shape.[24]

There are different methods in use for the fabrication of dental restorations. In this project, ceramic restorations and the techniques related to porcelain-metal systems are of interest.

2.2 Metal-Ceramic Systems with Dental Materials

The aesthetics of a dental restoration is an important property, and all-ceramic restorations are generally able to simulate the look of natural teeth. However, the brittle behaviour of ceramics combined with the risk of fracture while in the oral environment represent disadvantages of these restorations. The necessary mechanical properties can be achieved by using all-metal and all-alloy restorations. These however, lack the desired aesthetics. In order to get both the strength and toughness of the metal and the visual look of the ceramics a composite structure can be created. This type of structure is also called metal-ceramic systems or porcelain-fused-to-metals (PFM).[19]

In addition to providing strength and support to the dental porcelain, the metal substructure restores a tooth's contours. The substructure also provides the fit of the restoration. Lastly, the surface oxides on the metallic substructure are crucial for the bonding between the dental porcelain and the substructure.[25]

2.2.1 Composition and Properties of Dental Porcelains

Dental porcelains are both aesthetically pleasing and chemically stable, making them a good class of biomaterials for dentistry. They are able to mimic the look of a natural tooth due to their colour, shade and luster. The main component of these ceramics is a silicon-based inorganic material, which generally is a combination of silica, quartz or feldspar. Ceramics with feldspar as a main component are traditionally referred to as porcelains.[19] These porcelains have a composite nature, as they consist of a glassy matrix with a crystalline phase dispersed within it. The glassy matrix is generally silica-based.[26]

The crystalline phase can have different components, as it is added to alter the properties of the porcelain and the different components have different effects. The glass phase can be strengthened and toughened by adding ceramic and glass-ceramic particles. The colour and opacity of the porcelain can be adjusted by adding metallic oxides.[25] The crystalline phase can consist of feldspar, quartz, mullite, pigments and sometimes alumina. In some cases an organic dye is also added to the crystalline phase. This is done to make it easier to distinguish between the different porcelains when working with them prior to firing. Because these dyes are organic they will burn away upon firing.[26] The composition of dental porcelains vary with type of porcelain and product brand.[25] This is because the different types of porcelain have different "roles" in the porcelain build-up and therefore need to have slightly different properties. Some porcelains are designed to create adhesion, while others

are mainly responsible for the shape and final colour of the restoration.

The dental porcelains often have an alumino-silicate matrix, which together with feldspar forms the glass matrix. The feldspar used in dentistry are potassium- and sodium-based, namely potash feldspar and sodium feldspar. The ratio between these differ in mined materials, and is important for the handling characteristics of the final dental porcelain. The potash feldspar can give the final porcelain more translucent properties, in addition to helping maintain the form of the porcelain body during firing. The is because the viscosity of the molten glass is increased. Sodium feldspar makes the porcelain more susceptible to pyroplastic flow by lowering the fusion temperature. Most porcelains used today are synthetic and the compositions of them can be tailored to a larger degree.[25]

Quartz (SiO_2) is added to the porcelain to act as a framework that the other components can flow around. It also stabilizes the mass at higher temperatures, which prevents pyroplastic flow from occurring. Alumina (Al_2O_3) is added as it increases the viscosity of the melt and the overall strength of the porcelain. It does however have a lower coefficient of thermal expansion than the porcelain. The coefficient of thermal expansion of the porcelain can be increased by adding oxides of potassium, sodium and calcium to better match the thermal expansion of the metal. The increase is caused by these oxides breaking up cross-linking of oxygen in the silica-network. It is however important to avoid too much disruption of this cross-linking as that can lead to the glass recrystallizing.[25]

Different porcelains have different functions, and therefore different compositions. Because bonder porcelains are applied first to the substrate, they are designed to create good adhesion between the porcelain and the substrate. Opaque porcelains have a similar function to the bonder, as they wet the substrate forming a metal-porcelain bond. In addition the opaque porcelains are coloured in order to begin building the correct shade of the restoration and to cover the colour of the metal substrate.[25] Opaque porcelain has also been found to increase the debonding strength of a metal-ceramic restoration.[27] The main component of the porcelain body is the dentin porcelain, This is therefore designed to have the desired colour of the restoration and to build the shape of the restoration. Porcelains can come in different shades, but it is also possible to use stains to colour the final restoration. The glaze porcelain is applied last. It flows well at high temperatures, making it suited for filling in irregularities and porosity on the surface. Glazes are generally colourless and provide a shine to the restoration.[25]

Thermal compatibility between the metal and the porcelain is important in these metal-ceramic restorations. The porcelains used in these restorations are generally classified as low-fusing porcelains. This means that they become molten at temperatures below 850 °C, and the particles can fuse together. This low glass transition temperature is an important property because it allows the porcelain to become molten at temperatures below the melting range of the metallic substructure. If the substructure is exposed to too high temperatures it can deform and no longer be the correct fit for the restoration. The coefficient of thermal expansion (CTE) of the porcelain should be close to that of the substructure, but slightly lower. This is because if the porcelain has a lower CTE it will be under compression after firing,

which is beneficial for the strength of the restoration.[25] This is further discussed in Section 2.2.5 - Thermal Expansion.

Values for the glass transition temperature (T_g) and for the CTE of the bonder and dentin porcelain used in this project are given in Table 2.1. These porcelains are designed for use with titanium substrates, the properties will therefore be different for porcelains used with other metallic alloys. The CTE values are listed by the supplier for the whole product series and not for each porcelain type. They are given for the 25-500°C temperature range. The glass transition temperature has also been found in the product information from the supplier.

Table 2.1: Coefficient of thermal expansion, CTE, and glass transition temperature, T_g, for bonder and dentin porcelain for use with titanium.[28]

Porcelain	**CTE [$\mathbf{K^{-1}}$]**	**$\mathbf{T_g}$ [°C]**
Bonder	$8.6 \cdot 10^{-6}$	575
Dentin	$8.6 \cdot 10^{-6}$	575

2.2.2 Fabrication of Metal-Ceramic Systems

The application of porcelain to the metallic substructure is one of the most demanding processes related to metal-ceramic systems in dentistry. A metal die acts as the substructure or substrate for the dental porcelain, and can be used to replace a missing tooth. The die has the shape of the tooth that is to be replaced.[26] Multiple methods have been developed for the process, one of which is a build-up technique done by hand. This is an incremental technique where different types of porcelains are layered to create the final porcelain structure. This can result in very natural restorations, however it is very time-consuming and a sensitive technique. This places high demands on the dental technician.[25]

Commercial dental porcelains often come as powders, with accompanying modelling liquids. If there is no modelling liquid for a specific porcelain, distilled water can be used.[25] These dry powders are mixed with a small amount of modelling liquid to form a slurry. The desired viscosity of the slurry varies for the different porcelains and their designed use.[26] Metal equipment is avoided in the mixing process as they can be abraded by the ceramic particles and result in contamination. Instead, glass or ceramic mixing slabs and rods are used.

Once the slurry has the desired viscosity it can be applied to the metal substructure, using either a porcelain brush or a spatula. Porcelain brushes are generally better suited to build up the porcelain body and allows for greater precision. The shaped porcelain body should be consolidated prior to firing. This can be done by simply blotting the wet body with absorbent paper, or one can apply vibration as well. This allows excess liquid to rise to the surface, which can then be removed with paper. Capillary action will also draw out liquid from the porcelain body to the paper placed on the surface. A consolidation step is necessary because there will be pores in the fired ceramic if there is air or liquid left in the porcelain body during

firing. Pores will have a negative impact on the strength, colour and translucency of the fired ceramic. Additionally, proper consolidation can reduce the shrinkage of the ceramic during firing. The shrinkage can be compensated for, so that the final restoration has the correct shape and dimensions. This can be done by building the porcelain body 10 - 15 % larger than the wanted, final dimensions, and as mentioned by consolidating the porcelain body prior to firing.[25] [26]

Porcelains are subjected to a sintering process where some components melt and the end result is a homogeneous body. The glassy matrix in the porcelain becomes molten at the glass transition temperature, above this temperature the glass phase becomes viscous. However, the melting of feldspar-based glasses is slow and the melt is quite viscous. It possible to fire the porcelain for each layer that is built on the substrate because the melt is viscous enough that the porcelain will not lose its shape. This makes it easier to create these layered dental restorations. Prolonged heating of porcelain can result in slumping, i.e. that the porcelain loses its shape. To avoid this it might be necessary to fire each layer at subsequently lower temperatures.[26] Depending on the powders made by the supplier, the porcelain body is made by layering three or four different porcelains. The four general layers are: (1) bonder, (2) opaque, (3) dentin, and (4) glaze. Not all suppliers make a bonder porcelain, the bonder-layer is then skipped. Other porcelains can also be used to for example give certain optical effects.

At the beginning of the sintering process the particles are fused together at their contact points. Upon further heating more of the glassy phase will flow, and this flow will remove some of the air that was present prior to firing. As this continues more porosity is removed from the porcelain and any remaining pores are no longer connected to each other. The pores start out as irregularly shaped, however as the porcelain is fired longer they gradually transition into spherical shapes.[26] An illustration of the sintering process, showing the change in porosity is given in Figure 2.3.

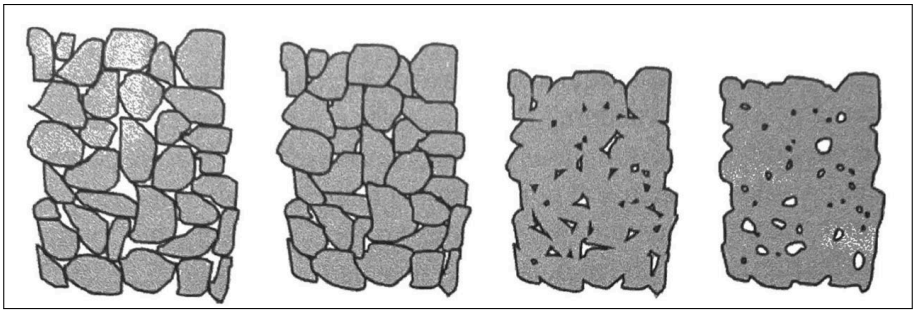

Figure 2.3: The change in microstructure during sintering of a porcelain.[26]

Porcelain firing can be done in vacuum or in air. By firing in air, 5 vol% of porosity will be left in the ceramic. Because of the previously mentioned risk of slumping, increasing the time spent at high temperatures would not be beneficial enough. Vacuum firing reduces the porosity, but there is still a chance of porosity. This is due to the pressure within the bubbles. The pressure inside the air bubbles, P_b, will be raised above ambient pressure, P_a, during firing by the liquid phase's surface tension[26]:

$$P_b = P_a + \Delta P \tag{2.1}$$

ΔP is the expected increase in pressure from ambient pressure. It depends on the initial radius of the bubble. The Laplace equation for a spherical droplet with a meridian on the surface, is given by

$$\Delta P = \frac{F}{\pi r^2} = \frac{2\pi r\gamma}{\pi r^2} = \frac{2\gamma}{r} \tag{2.2}$$

In this equation F is the force acting on the meridian, r is the radius of a cross section, and γ is the specific surface energy of the bubble.[26]

When the porosity becomes discontinuous during sintering, the remaining pores can be considered as fixed masses of gas at ambient pressure. The radius of these pores will be gradually reduced by the surface tension until an equilibrium is reached. At the same time there will be a concentration gradient driven dissolution of air. When the radius is reduced and the air dissolves, the excess pressure inside the pore increases as shown in Equation 2.2. This results in a more rapid process, but the process is still slow and has a limited effect. This makes it difficult to remove all porosity during air firing without significantly increasing the firing time.[26]

By firing under vacuum, or at least reduced pressure, instead of air firing the porosity can more easily be removed without increasing the firing time. The reduced pressure means that the air trapped within a pore has a lower mass, while the surface tension of the liquid is unchanged. Because of the unchanged surface tension, the excess pressure is the same as for air firing. The ratio between the ambient pressure and the pressure within the pores is increased, and the initial compression will also be increased.[26] The ratio between the two pressures can be written as

$$\frac{P_b}{P_a} = \frac{P_a + \Delta P}{P_a} \tag{2.3}$$

The equilibrium bubble size is smaller for vacuum firing than for air firing. The porosity is reduced to a greater degree, but there might still be pores left after firing. These will generally be smaller, and not affect the optical properties much. However, they will affect the strength like any other porosity.[26]

2.2.3 Adhesion Mechanisms

A metal-ceramic implant requires good adhesion between the layers to be durable enough. The adhesion is dependent on mechanical and chemical factors. It can be difficult to separate the two as they affect each other.[26]

The mechanism for porcelain-metal adhesion is not known but there are collectively, four theories that are suggested to explain the behaviour happening on the interface between the two components. These are, from most to least significant: (1) chemical

bonding, (2) compressive forces, (3) mechanical retention, and (4) Van der Waals forces of attraction.[25]

Van der Waals forces results in secondary bonding where instead of an exchange of electrons there are attractive forces between oppositely charged particles in the metal and porcelain. There is little attraction between molecules, therefore the van der Waals bonds are considered weak. These forces have been found to be dependent on the degree of wetting by the porcelain. If the porcelain is able to wet the substrate properly the van der Waals forces will be greater. A too rough substrate surface, and any contamination, will reduce the bond strength of the forces while a slightly textured substrate surface can promote the bond strength. This increase is because of the improved wetting.[25]

Wetting is also important for the mechanical retention. The molten porcelain will flow during firing, and can fill any microscopic irregularities on the surface if the wetting is good enough. The wetting of porcelains is further looked into in Section 2.2.4 - Wetting of Particles and Surfaces. These irregularities also contribute to the overall surface area available for porcelain attachment. In order to increase the mechanical retention any stress concentrations or stress raisers, often in the form of microscopic metal projections and other irregularities, should be removed. This can be done by airborne-particle abrading of the surface followed by steam cleaning. In addition to removing these sources of stress, the abrading results in an increased surface area and a clean substrate. Because porcelain is able to adhere to smooth metal surfaces as well, mechanical retention cannot be the most significant factor in porcelain-metal adhesion.[25]

Dental porcelains should be under compression rather than subjected to tensile forces as this increases the fracture strength. Placing the porcelains under compression also reduces the chance of cracking. This compression can be achieved by using metal substrates that have a higher coefficient of thermal expansion (CTE) than the porcelain. When the metal-ceramic restoration is cooled the porcelain will be placed under compression. The compressive forces can be aided by the substrate geometry. There will for example be a wrap-around effect in veneers with complete porcelain coverage but not in partially covered veneers. The wrap-around effect is seen because when the porcelain completely covers the substrate it is only under compression, while there will also be shear stresses where the porcelain meets the substrate for partially covered veneers. Thus, the effect of having complete porcelain coverage is increased compression of the porcelain. The metallic substrate will be under tension in both cases. However, it is still possible to get good adhesion in partially covered veneers, suggesting that compressive forces is not the principal adhesion mechanism.[19] [25]

Chemical bonding is considered the most significant mechanism in terms of establishing and maintaining porcelain-metal attachment. The chemical bonding is attributed to oxides on the metallic substructure and in the dental porcelain, with two proposed theories. The first theory, the "Sandwhich" theory, suggests that there is an oxide layer between the substructure and the porcelain and that there is no oxide migration between the oxide layer and the porcelain. This oxide layer should not be too thick as that weakens the adhesion. Over-oxidation of the substructure could

result in a too thick oxide layer. It is however known that metallic oxides migrate. Thus, this theory cannot explain the chemical bonding in itself.[25]

The second theory is called the oxide dissolution theory. In this theory, the porcelain layer dissolves some of the oxides from the substrate surface. This effect is illustrated in Figure 2.4. This dissolution results in contact between the atoms in the porcelain and the oxide layer on the substrate. This makes electron sharing between the components possible, resulting in enhanced chemical bonding and better wetting. The oxide layer should not be too thick, as in the "sandwich" theory. It might even be sufficient with only one layer of oxides.[25] [29]

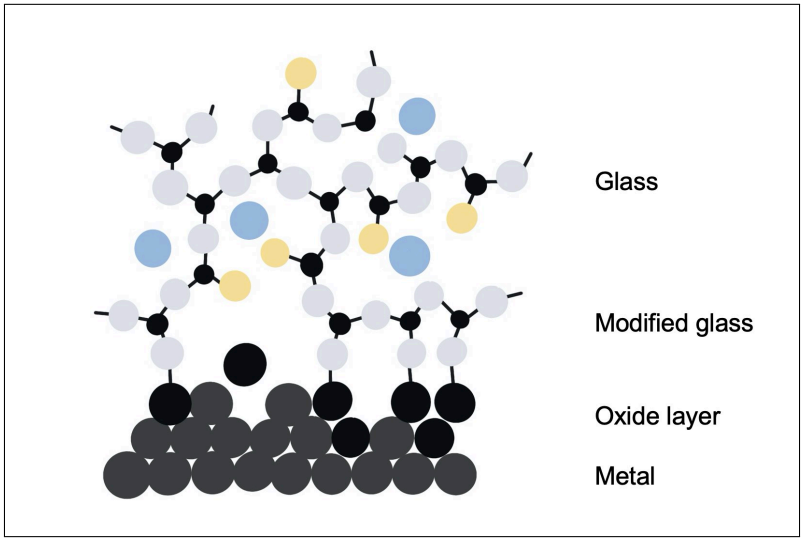

Figure 2.4: Illustration of the bonding between the glassy phase in the porcelain and the oxide layer from the metallic substrate surface. The illustration is based on Figure 6-5a in *Introduction to Metal-Ceramic Technology.*[25] [30]

2.2.4 Wetting of Particles and Surfaces

A liquid has to be able to wet a solid surface in order to establish and maintain contact with it. This wettability is dependent on the solid and liquid, and given by cohesive and adhesive intermolecular interactions.[31] Wetting is determined from the contact angle between the solid and the liquid. Examples of contact angles and spreading of droplets at these angles are given in Figure 2.5. The angle is measured between a plane tangent to the liquid's surface and a plane tangent to the solid's surface, with the measurement being done through the liquid. From the examples one can see that a smaller contact angle corresponds to a higher degree of wetting, and that liquids that wet the surface to a small degree have a large contact angle. The figure also shows that the droplet changes shape as the contact angle decreases. This is because of the thermodynamic principle that liquids will change shape to reduce their total energy. This is achieved by reducing their surface area, as this results in a lower total surface energy. When no work is performed on the liquid the droplets will form spherical shapes.[26]

Adding liquids to solid surfaces creates two interfaces: (1) a liquid-solid interface,

and (2) a liquid-vapour interface. The second interface is created due the volatile liquid's vapour pressure. All interfaces have an individual interfacial energy. The liquid-solid interface often has a lower interfacial energy than the liquid-vapour interface. In those cases the liquid will spread onto the surface to reduce the total energy in the system. As the surface area of this interface is increased, the area of the liquid-vapour interface is reduced.[26]

The surface area of the liquid-solid interface, and with that the degree of wetting, is also affected by the liquid's surface tension and the solid surface's energy. A lower surface tension increases the wettability of the liquid, while solid surfaces with high energy are more easily wetted. Most ceramic materials will not be wetted by liquids with high surface tension. Combining a liquid with low surface tension and a solid surface with high energy results in strong interactions between the two materials. This lowers the interfacial energy, promoting wetting. Increasing the surface area of the solid, for example by adjusting the surface roughness, increases the interface area. Thus the specific surface energy is increased.[26]

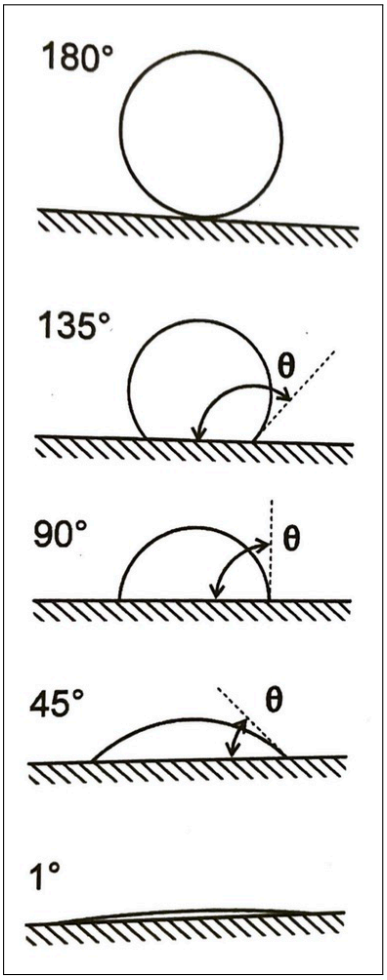

Figure 2.5: Illustration showing a droplet on a surface, with different contact angles.[26]

Wetting is important in dentistry as it drives the flow of the glass phase. Good wettability is crucial for making dense ceramics where the porcelain-metal adhesion is good. The flow will be hindered by any contaminants and other particles present, affecting the porcelains ability to wet the substrate. When working with porcelains where ceramic particles are included it is beneficial if the glass phase is able to wet these particles as well as the substrate.[26] Bernardo et al.[32] found that rigid inclusions could decrease the viscous flow ability of the glass phase. There are examples of glass phases being able to wet ceramic powders. El-Kheshen et al.[33] found that borosilicate glasses are able to wet mullite and magnesium aluminate spinel particles.[33]

In this project only two of the four wetting situations relevant for dentistry is of interest.[26] The first situation is the formation of a coating mixture by mixing liquid and solid components, in the form of powder. The second wetting situation is immersion. In this situation there is an excess of liquid, which is spread by mechanical intervention for example by using a brush. As long as the contact angle is less than 180°, a solid substrate will be wetted by any excess amount of liquid. The contact angle between the liquid and solid substrate is therefore no longer relevant in this wetting situation. Still, the work of adhesion has to be non-zero for there to be interaction between the liquid and the solid.[26]

2.2.5 Thermal Expansion

Temperature changes induces a change in dimension in most materials. This dimension change is referred to as *thermal expansion*. It is measured either as percent, ppm, or as the coefficient of thermal expansion (CTE). The CTE, α, is given as

$$\alpha = \frac{\Delta l / l_0}{\Delta T} \tag{2.4}$$

where ΔT is the difference between temperature T_1 and T_2, l_0 is the material length at T_1, and Δl is the change in length between the two temperatures.[34]

The arrangement of atoms within the material, and the bond strength between them, affects the thermal expansion. Stronger bonds reduces the thermal expansion, this applies both for ceramics and metals. Glasses differ from this, as the glasses' thermal history also will affect the thermal expansion. In silicate glasses and porcelains the CTE is changed at the glass transition temperature. At and above this temperature the porcelain is more viscous than solid, the CTE is increased to reflect this. The heating rate of glasses also affect their CTE.[34] [26]

It is especially important to consider the coefficient of thermal expansion in material systems with more than one material in close contact. When the materials have different coefficients they will expand and contract at different rates during heating and cooling. If the difference is large, high stresses can be introduced to materials. This can then increase the chance of distortion and fractures. Materials with similar coefficients result in reduced thermal stresses.[34] When working with porcelain-metal systems, where there also is a filler ceramic material in the porcelain, the ratio between the coefficients have to be considered for the porcelain-metal system and for the porcelain-filler system. If the CTE of the porcelain and the metal differ with more than 10^{-6} K^{-1} there is a larger risk of the porcelain delaminating from the metal.[35]

Since both the porcelain and the ceramic filler particles are brittle materials, almost no plastic deformation of these is possible. This makes it even more important to reduce the tensile strain in the porcelain. The glassy phase making up the matrix of the porcelain will be placed under tension if the matrix contracts more than the filler particles, while the matrix-filler interface is placed under tension if the particles contracts more than the matrix. The porcelain would therefore be more prone to failure.[26] When the filler particles have a higher coefficient of thermal expansion than the matrix, tangential compressive and radial tensile stresses will develop in the matrix close to the particles.[32]

2.2.6 Integration of Dental Implants with Bone

The long-term success and healing of a dental implant, as well as other implants, is dependent on the osseointegration of the implant.[36] Osseointegration is defined as *"a direct structural and functional connection between living ordered bone and the surface of a load carrying implant."*.[37] This process starts immediately after

implantation and can continue for several months. The implanted material is integrated into the surrounding bone. Osseointegration depends on factors such as biocompatibility of the implant material, design and surface conditions of the implant, health and bone quality, and loading conditions on the implant.[36] [37] [38] The biocompatibility of the implant, placement of the implant and degradation of the implant material can contribute to bone loss in the surrounding area of the implant. This reduces the mechanical stability and osseointegration of the implant.[38]

Currently there is a lot of work being done in relation to improving the osseointegration of implants. Many studies focus on the surface properties of the implants.[36] Some studies have shown that the binding to bone of titanium alloys can be improved by treating the surface. These surface treatments can be divided into (1) addition of material, (2) removal of material, and (3) modification of material.[39] One such surface treatment is the addition of a bioactive coating, for example hydroxyapatite or other calcium phosphates. These are used due to their ability to stimulate bone growth, as this increases the cell attachment to the metal implant.[36]

Slight loading of dental implants and bones has been shown to increase bone formation.[38] The loading results in the generation of electrical potentials in the bone, due to the piezoelectric nature of bones. It is these electrical potentials that stimulate bone growth. Externally applied electric stimulation has the same effect on bone growth. The integration of implants with bones can therefore be improved by applying an electrical stimulation to these implants. Coating the implants with a piezoelectric material can be a method of applying this electrical stimulation without the need of external sources.[8] [9] [11] [12]

2.3 Electrical and Dielectric Properties

2.3.1 Piezoelectricity

The piezoelectric effect was first discovered in 1880, by Pierre and Jacques Curie. They observed that some single crystals, such as quartz, topaz and Rochelle salt, developed an electric charge on the surface when they were under mechanical stress. This is called the direct piezoelectric effect. There is also a converse piezoelectric effect, where the application of an electric field results in a deformation of the material. The resulting surface charge from the direct piezoelectric effect is either positive or negative, depending on the direction of the mechanical stress.[34] [40] [41] [42] A compressive stress generates a negative charge while tensile stress generates a positive charge.[9]

Even though the effect was discovered in 1880, piezoelectric materials were not used until the early 1900s. Some of the earliest uses were in phonographs and to better tune radios to broadcast channels. In 1930 piezoelectrics were used in microphones, from then on piezoelectric ceramics have found more and more applications. They are for example used in ultrasonic cleaners, actuators, transformers, and to make noises such as alarm clocks, smoke alarms, and even in musical greeting cards.[43] Some medical devices also use piezoelectric materials, such as insulin pumps, ultra-

sonic cataract-removal devices, and for ultrasonic therapy.[44]

Piezoelectric materials can be divided into two categories: (1) natural, and (2) man-made. The natural piezoelectric materials include organic substances like wood, bone, hair, silk, enamel and rubber, as well as crystal materials such as quartz, topaz and Rochelle salt.[45] Fukada and Yasuda observed the piezoelectric properties of bone in the 1950s.[10] Bones consists of collagen fibers with hydroxyapatite particles. This collagen has a spiral structure called triple helix, and it is in these collagen fibers that the piezoelectric effect generates a surface charge.[46]

2.3.2 Properties of Piezoelectrics

Piezoelectrics are a subset of dielectric materials. Dielectric materials are electrical insulators that do not conduct electric current under application of an external electric field. However, there is a small change in the charge balance within the material leading to formation of an electrical dipole.[34] In other words, when no electric field is present the polarisation of a dielectric is zero. Piezoelectric materials are dielectrics that develop a surface charge under mechanical stresses, without the need of an external electric field. There is also a subset of piezoelectric materials; pyroelectrics. In these materials a change in temperature is able to induce a change in polarisation. They have been found to have spontaneous polarisation, which does not require either an electric field or mechanical stress. If this spontaneous polarisation can change direction when an electric field is applied the material is ferroelectric, which is a subset of pyroelectric materials.[40] Ferroelectric properties in piezoelectric materials will prove to be useful, especially for polycrystalline materials.

As stated earlier, the Curie brothers first discovered piezoelectricity in single crystals. The piezoelectric effect in single crystals results in a net positive charge on one side and a net negative charge on the other side. This requires a non-uniform distribution of positive and negative charges, which is only possible in non-centrosymmetric crystals. Of the 32 crystal classes, 20 do not have a center of symmetry and can therefore exhibit piezoelectricity.[34] In polycrystalline ceramics the crystallites, also known as grains, will be randomly oriented and divided by grain boundaries. In ferroelectric piezoelectrics there are ferroelectric domains, within each domain the polarisation is uniform. These domains are also randomly oriented.[41] The ceramic itself will have a center of symmetry and the piezoelectric effect in the grains will cancel each other out, resulting in a zero net polarisation. In other words, the ceramic has no piezoelectric properties.[47]

The piezoelectric effect in these ceramics can only be utilized if the net polarisation is non-zero. This can be achieved by poling the material. Poling is a process where the orientation of the ferroelectric domains are switched to line up with the crystallographic direction closest to the direction of the electric field. This re-orientation is driven by an external electric field. The poling process results in an increased net polarisation, with the maximum level of polarisation being achieved when the alignment of all the ferroelectric domains is parallel to the field. As the electric field is reduced some of the domains will switch back but there will still be a net polarisation when the electric field is zero. This polarisation is known as the remnant

polarization, P_r. Figure 2.6 shows the change from the unpoled state to the poled state. [41] [47] [48]

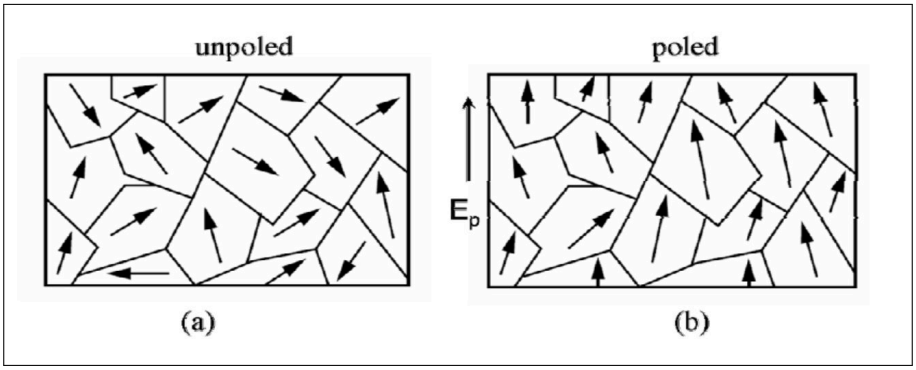

Figure 2.6: Sketch showing the change from unpoled (a) to poled domains (b) within a piezoelectric material. [48]

The switching of the ferroelectric domains can be observed in a polarisation-electric field hysteresis loop and a strain-electric field hysteresis loop. An example of both these loops is given in Figure 2.7. Ideally these loops are symmetric but there are multiple factors affecting both shape and symmetry. Some examples of these factors include charged defects, grain size, sample thickness, thermal treatment, mechanical stresses, and composition of the material [13] [41] [49] In addition to these loops, the piezoelectric coefficient d_{xy} is an important property of piezoelectric materials. The coefficient d_{33} gives information about the displacement parallel to the electric field, per unit applied electric voltage. [48] [50]

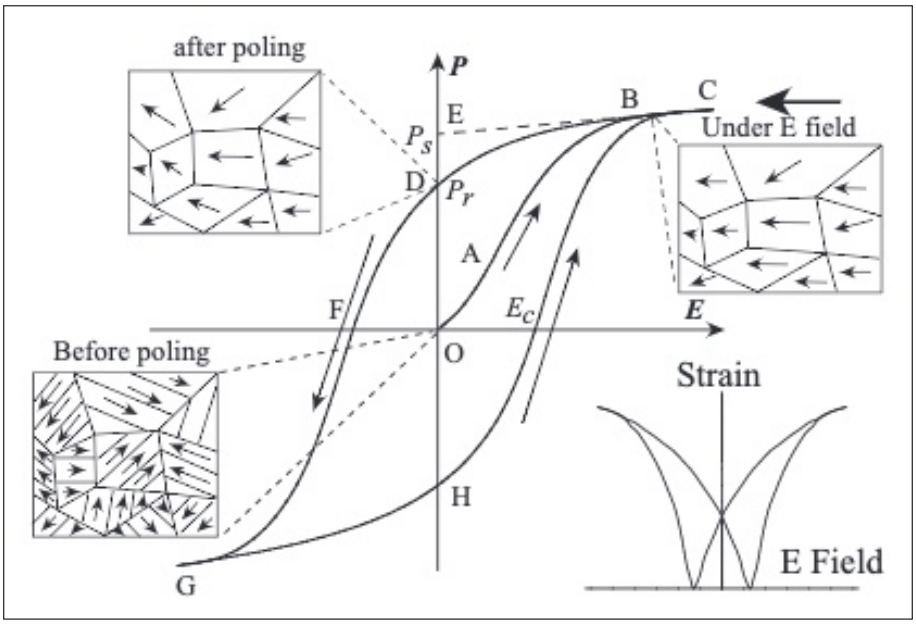

Figure 2.7: The polarization-electric field hysteresis loop of an ideal ferroelectric material, together with sketches of the domains at certain points in the hysteresis loop. In the bottom right corner a strain-electric field loop is included. [49]

2.3.3 Effect of Pores and Inclusions on Electric Properties

In porous ferroelectrics there will be a reduced amount of ferroelectric mass compared to a dense ferroelectric. This will contribute to a reduction in piezoelectric properties in porous ferroelectrics.[51] [52] However, the reduction in remnant polarisation with increasing porosity is too rapid for it to be explained completely by a volume-fraction relationship. Thus, the polarisation is reduced by something in addition to the reduction in ferroelectric material due to the presence of pores.[51]

The electric field distribution in a dense, bulk ferroelectric material will be relatively homogeneous. The same is the case for isotropic insulators like glass. When the applied electric field is homogeneously distributed in a ferroelectric, the ferroelectric domains will feel the same electric field. For fields greater than the coercive field of the ferroelectric, the result will be a fully poled material.[40] [51]

In materials with pores and in materials consisting of a matrix and a filler material, there can be differences in their relative permittivity ϵ_r.[51] [53] [54] The relative permittivity is often also referred to as the dielectric constant. It is given by the ratio between the permittivity of a dielectric material (ϵ) and the permittivity of vacuum (ϵ_0)[44] [51]:

$$\epsilon_r = \frac{\epsilon}{\epsilon_0} \tag{2.5}$$

Pores have a lower permittivity than bulk ferroelectrics. When porous ferroelectrics are placed under an electric field, a concentration of the electric field in the porous regions can be observed. Thus, the electric field is inhomogeneously distributed throughout the material. This distribution of the electric field can have a negative effect on the polarisation of the material, as different areas of the material will experience different electric fields. Porous ferroelectrics have been found to have lower saturation polarisation and remnant polarisation compared to a dense, bulk material.[51] [53] [54] [55]

The difference in permittivity, resulting in inhomogeneous distribution of the electric field, has been found to have an effect on the overall properties of the ferroelectric. In addition to affecting the electric field, stress can become concentrated around the pores during the poling process. This can then lead to constrained or enhanced domain wall motion, ultimately affecting the piezoelectric properties. The shape of these pores have also been found to have an effect. A study found that BCZT with irregular pores showed lower piezoelectric and ferroelectric properties than when the pores were spherical.[51] [52] [53] [54]

Studies have been performed on the electrical properties of hydroxyapatite-barium titanate composites and on polymer-ceramic composites.[56] [57] [58] [59] Even though the material system in this study is different, these materials are similar and can provide some insights. Tavangar et al.[56] found that the volume fraction and dimensional ratio of the barium titanate particles, together with the shape and amount of porosity in the hydroxyapatite matrix, affected the electrical properties of the composites. The electrical properties of the composite was improved by including

barium titanate, when compared to pure hydroxyapatite. The same study also found that the permittivity of the composite was significantly lower than that of the bulk barium titanate.[56] The permittivity of the composites were found to increase as the amount of barium titanate particles were increased.[57]

Prakasam et al.[58] found that the permittivity was highest for composites with the largest amount of barium titanate, which was expected. However, they did not observe a piezoelectric coefficient in the composites when the amount of barium titanate was lower than 80%. In the study performed by Wang et al.[59], the matrix material (polymer) had a lower permittivity than the filler material (ceramic). Around the interfaces of the two phases, a concentration of charge carriers was found.

The permittivity of a composite material is expected to increase more once the amount of high-permittivity particles reaches the percolation threshold. Above this point, the particles are able to form a continuous network.[60]

2.4 Barium Titanate Doped with Calcium and Zirconium

Barium titanate ($BaTiO_3$) has been of interest since it was the first developed piezoelectric perovskite in 1946. It is a highly stable material, both chemically and mechanically. This combined with a high dielectric constant and low dielectric loss has made the material very useful in capacitors. $BaTiO_3$ is also a ferroelectric material, for temperatures higher than or equal to room temperature. It has a piezoelectric coefficient $d_{33} \approx 190$ pC/N. This can be improved by doping the $BaTiO_3$. Doped compositions of $BaTiO_3$ have been used for semiconductors and for piezoelectric materials.[61] [62] [63]

The perovskite crystal structure of $BaTiO_3$ typically has a ABO_3 chemical formula. There are two types of cations, the A-site cation and the B-site cation. The A-site cations are the Barium ions, these are placed in the corners of the structure. The B-site ions are Titanium, which is placed in the middle of the structure. Oxygen are the anions, these are placed at the faces of the crystal structure.[63] A sketch of barium titanate's perovskite structure is given in Figure 2.8, showing the placement of these ions. Barium titanate can be doped with Ca and Zr because it forms solid solutions with $CaTiO_3$ and $BaZrO_3$. Other dopants are Sr and La, which together with Ca substitute A-site cations, as well as Zr, Nb and Ta for the B-site cations.[61]

Doping barium titanate with Ca and Zr to the following composition, $(Ba_{0.85}Ca_{0.15})(Zr_{0.1}Ti_{0.9})O_3$ (BCZT), creates an interesting material with good piezoelectric properties. This is because the morphotropic phase boundary of the solution is found within the $(Ba_{0.85}Ca_{0.15})(Zr_{0.1}Ti_{0.9})O_3$ composition in the phase diagram. For ferroelectric materials, the best properties are generally found at this phase boundary.[62] BCZT goes through a phase transformation from rhombohedral to tetragonal, which is the ferroelectric properties are best, and another transition from tetragonal to cubic.[65] [61] In this region Tian et al.[62] reported d_{33} values of 572 pC/N for this BCZT composition, made via solid-state synthesis. However, d_{33} values as high as 620 pC/N have been reported for $(Ba_{0.85}Ca_{0.15})(Zr_{0.1}Ti_{0.9})O_3$.[61]

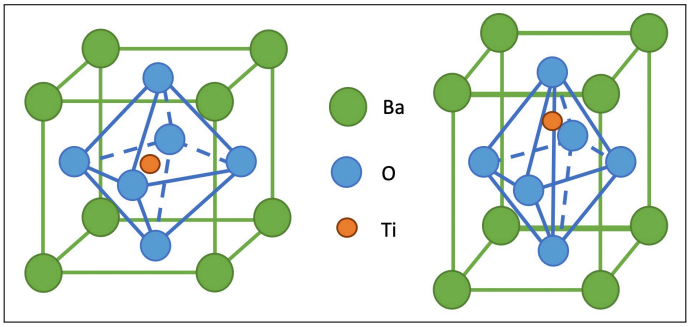

Figure 2.8: The cubic (left) and tetragonal (right) perovskite of barium titanate. Redrawn from [64].

Another important aspect of adding dopants is their effect on the Curie temperature, T_C. At this temperature the spontaneous polarisation disappears. The BCZT transitions from tetragonal to cubic, which is a centrosymmetric structure. [65] [66] Pure barium titanate has a $T_C = 120\,°C$. [67] Dopants can either increase or decrease this. From Figure 2.9 it is clear that Zr as a substitute for Ti will lower the T_C, while Ca in place of Ba will leave it relatively unchanged. Thus, BCZT will have a lower T_C than $BaTiO_3$. [66]

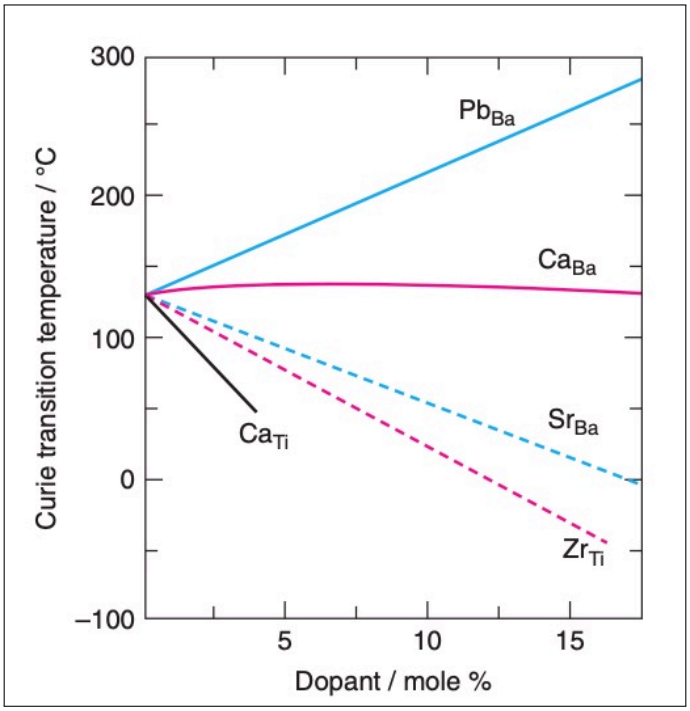

Figure 2.9: Plot showing how different dopants affect the Curie temperature of barium titanate. [66]

The grain size in a piezoelectric ceramic also affects the piezoelectric properties. The grain size in the final ceramic is dependant on the whole synthesis, i.e. from raw powders to the final sintering stage in solid-state synthesis. The grain size will affect the size of the formed domains within the BCZT, thus being of importance for the piezoelectric properties. [65] $(Ba_{0.85}Ca_{0.15})(Zr_{0.1}Ti_{0.9})O_3$ has been chosen for its good

piezoelectric properties. Values for the piezoelectric coefficient and Young's modulus for this composition are given in Table 2.2. An approximate value is given for the coefficient of thermal expansion because no value could be found for the specific composition. Other similar compositions have reported values of CET = $8.31 \cdot 10^{-6}$ K^{-1} [68] and CET = $8.19 \cdot 10^{-6}$ K^{-1} [62]. Based on these values the approximate value has been set to $8 \cdot 10^{-6}$ K^{-1}.

Table 2.2: Some properties of $(Ba_{0.85}Ca_{0.15})(Zr_{0.1}Ti_{0.9})O_3$.[69] [61] [68] [62] d_{33} is the piezoelectric charge coefficient, E is the elastic modulus, and CTE is the coefficient of thermal expansion.

Property	Value	Unit
d_{33}	620	pC/N
E	117.9	GPa
CTE	$\sim 8 \cdot 10^{-6}$	K^{-1}

Biocompatibility is an important aspect of any material designed for use in the human body. BCZT has been found to be biocompatible, with one study[13] looking at the compatibility of BCZT with osteoblast and endothelial cells. Barium-ions could however be toxic. It is therefore important to have barium-compounds that are not soluble in the body.[13] Pisitpipathsin et al.[70] found that adding BCZT to a bioglass enhanced the bioactivity of the glass, resulting in apatite layers forming on the surface after soaking the composite in simulated body fluid (SBF).

2.5 Synthesis of Ceramics

2.5.1 Solid-State Synthesis

Solid-state synthesis is a common and simple method for processing many conventional ceramics. The ceramics go from a fine powder to a dense ceramic through a series of steps. The first step of the solid-state synthesis is the powder preparation. In order to achieve the correct composition in the final ceramic, precursor powders containing the necessary elements are mixed together into a homogeneous powder. These precursors are often oxides of the necessary elements. There are different ways of mixing the precursors however, ball milling is one of the most frequently used methods. This is because in addition to thoroughly mixing the powders the ball milling reduces the particle size.[34]

A smaller particle size is preferable due to the higher reactivity of small particles. When particles are smaller their surface area is higher, and they therefore have high surface free energy. This leads to a higher driving force for densification as a lower surface energy is thermodynamically preferred. By bonding together the particles reduce their overall surface area, thus the ceramic becomes denser.[34]

A small particle size alone will not give maximum densification. If all the particles have the same size and are packed in the most optimal way, voids will still make up around 30% of the total space prior to densification. The space taken up by voids

will be reduced by having a range of particle sizes. A good particle size distribution can also be achieved through ball milling. During the milling process the particles will be broken into smaller particles to a varying degree.[34]

The particle size distribution will be affected by whether the ball milling is done wet or dry. In dry ball milling the powder is added to a milling jar together with milling media, often shaped as balls. In wet milling a liquid is added to the milling jar as well. During the milling the jar will be rotated, allowing the milling media to cascade and crush the particles. By using a wet milling method one can achieve a smaller particle size as well as a more narrow particle size distribution.[34]

There are some drawbacks with ball milling, with contamination being one of the biggest issues. As the milling media cascades within the milling jar and crushes the particles, it will also wear on the walls in the milling jar. The milling media will gradually be degraded. Thus, both the milling jar and the milling media can be sources of contamination. This effect can be reduced by choosing appropriate materials for the walls in the milling jar and for the milling media. Different ceramic particles can have different requirements for these materials to reduce the contamination.[34]

Once the precursor powder has a good particle size distribution and mean particle size it can be shaped, very often pressed into a die, to be calcined. There are multiple pressing methods, but the most common are uniaxial pressing and isostatic pressing. In uniaxial pressing the pressure is applied to the die in one direction. Cold isostatic pressing is a method where the pressure is applied from all directions. The compaction from cold isostatic pressing is more uniform than that of uniaxial pressing. Non-uniform density in the green body after uniaxial pressing can be caused by friction between the die wall and the powder, as well as between the powder particles. Uniaxial pressing can also result in cracking.[34]

The precursors react with each other, resulting in the wanted chemical composition, in a process called calcination. Calcination is a process where the precursors are heat treated at high temperatures, promoting the solid state reaction between the precursors. This is a diffusion dependent and often slow process. The high surface area of small particles are therefore beneficial, in addition to a large contact area between the precursor particles. Pressing the precursor powder into e.g. pellets increases the contact area between the particles. The precursors are often calcined for a long time to ensure complete reaction. The calcined pellets are crushed and milled into a powder prior to the next step in the synthesis.[34]

Sintering of ceramics is done to achieve a dense, fine-grained microstructure. Prior to sintering the ceramic powder should be compacted in a way that leaves close-packed and uniformly distributed particles. Ideally the green body has 50% or less porosity. During sintering pores in the green body are removed, and the green body shrinks. Adjacent particles will grow together and be strongly bonded. The densification during sintering requires the presence of a mechanism for material transport, and a source of energy to drive this material transport. The primary source for this energy is heat. There are also energy gradients from contact between particles and surface tension that contribute. Different materials have different requirements to the temperatures during calcination and sintering. For $(Ba_{0.85}Ca_{0.15})(Zr_{0.1}Ti_{0.9})O_3$

there are examples of calcination temperatures of 1350 °C and sintering temperatures of 1450 °C.[65]

In solid-state sintering the mechanism for material transport is volume diffusion. The material being transported can either be atoms or vacancies. The transport can go through the volume of the material, or it can go along either the grain boundaries or the surface.[34] An illustration of this material transport is given in Figure 2.10.

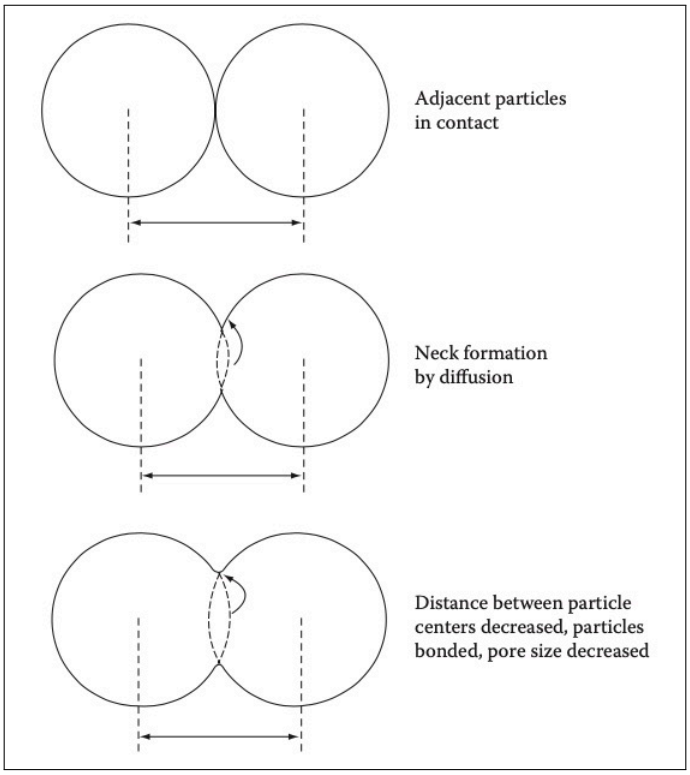

Figure 2.10: Illustration of the material transport during solid-state sintering.[34]

The sintering process can be divided into three different stages. In the *initial stage*, particles are rearranged and neck formation begins at the contact points of the particles. This is where the surface energy is highest and material transport most easily can occur. The majority of the densification and shrinkage happens in the next stage, which is called *intermediate sintering*. The necks between the particles grow more and the distance between the centers of the original particles is reduced. Together with this the porosity decreases. As the neck growth and porosity removal continues, the green body geometry is adapted to accommodate these changes. The particles become grains, with grain boundaries separating them. These grain boundaries move during this stage because grains grow and consume neighbouring grains.[34] An illustration of changing microstructure in the different sintering stages is given in Figure 2.11.

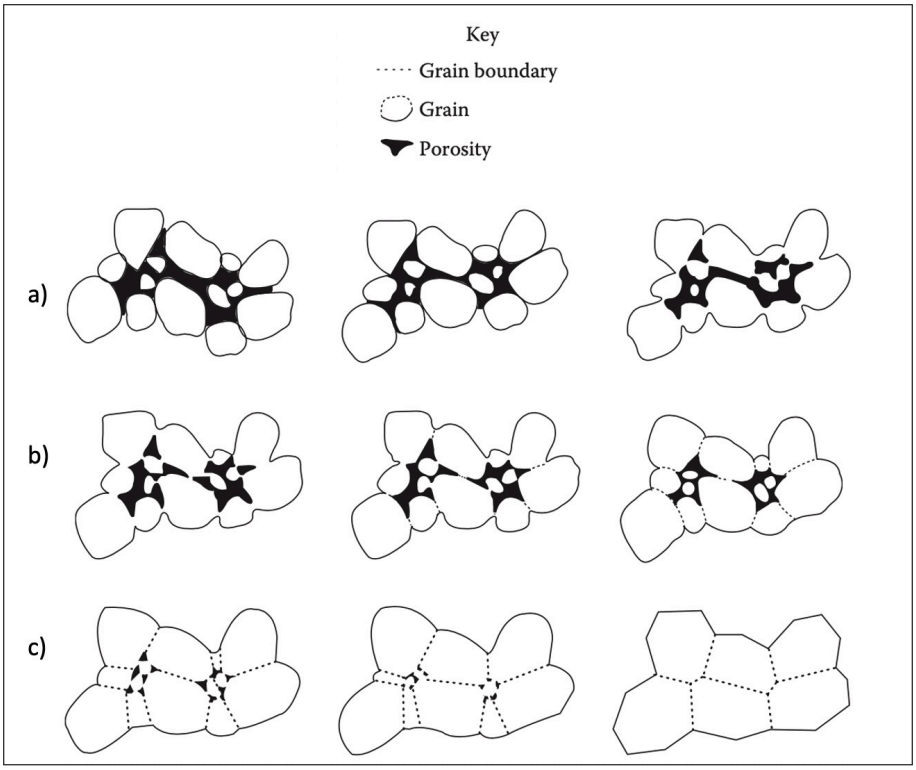

Figure 2.11: Illustration of the sintering stages; (a) initial stage, (b) intermediate sintering stage, (c) final sintering stage.[34]

Gradually the pores are removed and the remaining pores are isolated. When this happens the ceramic is in the *final sintering* stage. The remaining pores are removed by vacancy diffusion, happening along the grain boundaries. For optimal pore removal the pores have to be close to the grain boundaries. There is grain growth in this stage. This means that the grain boundaries are moved, which can improve the pore removal. However, it is important that this grain growth is controlled. If the grain growth is uncontrolled the grain boundaries may move too fast compared to the pores. This can result in pores being isolated within the grains.[34]

The driving force for the solid-state sintering is difference in chemical potential, alternatively free energy, of the particle surfaces and the contact points between the particles[34]. When the material is transported via lattice diffusion from a contact point to the neck region, the model of the transport mechanism is:

$$\frac{\Delta L}{L_0} = \left(\frac{K\gamma \cdot a^3 \cdot D * \cdot t}{k \cdot T d^n} \right)^m \tag{2.6}$$

However, this model fits best with the *initial stage* of solid-state sintering. In this model $\frac{\Delta L}{L_0}$ is the linear shrinkage, which corresponds to the sintering rate. K is a geometry-dependant constant, γ is surface energy, a^3 represents the volume of a diffusing vacancy, t is the time, and D^* is a self-diffusion coefficient. k and T correspond to the Boltzmann constant and the temperature, respectively. The particle diameter is d. The two exponents n and m are typically close to 3 and 0.3-0.5, respectively.[34]

Based on this model it is clear that the particle diameter and the temperature are important factors during sintering. This also shows why smaller particles are preferred during sintering as they result in a higher sintering rate. In order to achieve the same sintering rate at lower temperatures one can reduce the particle size.[34]

2.5.2 Liquid Phase Sintering

Ceramics can also be made through liquid-phase sintering. This is a sintering method where there is a viscous liquid promoting the sintering. Many silicate systems are densified either with liquid-phase sintering or with viscous composite sintering. Multiple factors will affect the final microstructure after sintering, such as amount of liquid present, particle size and the temperature program especially in terms of cooling.[34] Some examples are shown in Figure 2.12.

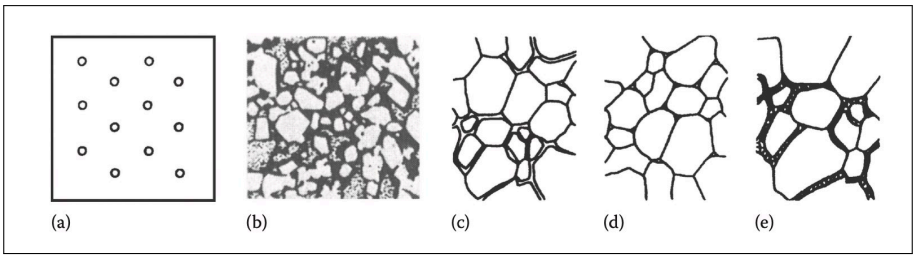

Figure 2.12: Illustration of different microstructures that liquid-phase sintering can result in. The microstructures shown here are sintered glass (a), a crystal-liquid structure (b), grain boundary glass (c), glass at triple junctions (d), and lastly crystallized grain boundaries (e).[34]

The second microstructure is often the results when a large amount of liquid is cooled quickly enough that the liquid is able to solidify as glass. This is the case for viscous composite sintered porcelains. This type of sintering requires that more than 20% of the total material is liquid phase at high temperatures.[34]

The liquid-phase sintering rate is controlled by particle size, viscosity and surface tension. The latter two are strongly affected by temperature and composition. An increase in temperature can result in increased amount of liquid phase, thus aiding densification. The sintering rate will also be increased if the liquid phase is able to wet the solid particles.[34]

2.6 Metal Substrate Material - a Ti-6Al-4V Alloy

As stated previously, metals have been used for implants for a while now. Pure titanium and its alloys have since they were introduced in the 1960s become among the most used metallic biomaterials. They are commonly used for medical and dental implants. This includes medical implants such as hip prostheses, artificial knee joints, bone plates and cardiac valve prostheses, as well as dental implants such as overdentures, crowns, bridges and components for dental implant prostheses. In 2008 the most used dental implant was screw shaped and made of either titanium or

the Ti-6Al-4V alloy.[3] [71] [72] This specific alloy was originally designed for aerospace applications and as a structural material, due to its high specific strength to weight ratio.[73] [74]

Ti-6Al-4V is a titanium alloy containing 5.5-6.5 wt% aluminium and 3.5-4.5 wt% vanadium. It is a grade 5 titanium alloy, also referred to as Ti6Al4V or Ti64. The alloying elements were added to increase the strength and hardness of the titanium. As a result, Ti-6Al-4V has higher values for elastic modulus and strength compared to lower grade titanium alloys. In this project the most relevant properties of the Ti-6Al-4V, i.e. the metal substrate, is the elastic modulus, coefficient of thermal expansion, ultimate tensile strength and yield strength.[71] [75] Values for these properties are given in Table 2.3 below.

Table 2.3: Some mechanical and physical properties of Ti-6Al-4V.[71] [76]

Property	**Value**	**Unit**
Yield strength	795	MPa
Ultimate tensile strength	860	MPa
Elastic modulus, E	114	GPa
CTE	$9.2 \cdot 10^{-6}$	K^{-1}

In addition to having the necessary mechanical properties a biomaterial needs to be biocompatible. This entails that the material is not toxic while in the body, and that it will not be destroyed while in use.[43] The human body is a highly corrosive environment, which could lead to detoriation of the implant over time. Because of this, corrosion resistance is an important property in terms of biocompatibility. If the material corrodes while implanted it could lead to release of ions, which could be toxic.[6] Biocompatibility is also dependent on other material properties, such as low ion formation tendency in aqueous environments, low level of electronic conductivity, and whether the material is in its thermodynamic equilibrium at physiological pH values. Even though Ti-6Al-4V is commonly used as a biomaterial, it might have a toxic effect caused by aluminium and vanadium being released. This is especially relevant for permanent implant applications.[71]

The mechanical properties of Ti-6Al-4V will be negatively affected above a certain temperature due to oxidation of the material. The oxidation happens above 480 °C, thus the alloy has a maximum service temperature of 350 °C.[77] Higher temperatures can also affect the distribution of alloying elements in Ti-6Al-4V, especially aluminium. Segregation and diffusion of aluminium towards the surface of the material has been observed at high temperatures by Lutz et al.[78] and Rodriguez et al.[79]. This segregation was observed at 400 °C, with an observed increase at 750 °C. The diffusion of Al was found to increase with the temperature during heat treatment of the alloy.

2.7 ISO 9693:2019 - the De-bonding/Crack Initiation Test

The ISO standard ISO 9693:2019 concerns the compatibility in metal-ceramic and ceramic-ceramic material systems used in dentistry. This standard exists to ensure that the veneering ceramic and the substructure material function are compatible for the mechanical and thermal conditions in an oral environment. Chapter 4.2.3 (*De-bonding/crack-initiation test*) and 6.4 (*De-bonding/crack-initiation test*) provide requirements for the debonding/crack-initiation strength of the material system and the requirements for testing this strength, respectively.[80]

For metallic substructures and at least one dental veneering ceramic, the debonding strength has to be greater than 25 MPa. This strength is to be measured in a flexural-strength testing machine with a three-point bending set-up. At least six samples have to be tested, and they have to fracture by a de-bonding crack at one end of the ceramic layer. There are requirements to the size and shape of both the substructure and the ceramic layer. The substructure has to be (25 ± 1) mm x (3 ± 0.1) mm x (0.5 ± 0.05) mm. In the middle of the substructure, an (8 ± 0.1) mm x (3 ± 0.1) mm x (1.1 ± 0.1) mm is to be placed. The dimensions for the ceramic layer is for the fired ceramic.[80] A sketch of the sample with these dimensions is given in Figure 2.13.

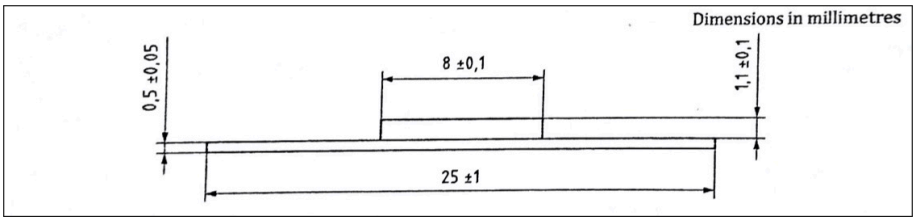

Figure 2.13: Sketch of the sample with the required dimensions according to ISO 9693:2019.[80]

The de-bonding test is done in the three-point bending set-up with the applied load on the underside of the sample, i.e. with the ceramic facing the opposite side of the load. This load is applied at a constant speed of (1.5 ± 0.5) mm/min until fracture. The criteria for fracture is a sharp decline in force of at least 5%. There are two fracture types, of which only one is an approved fracture. The approved fracture is an "end of ceramic" fracture, meaning that the fracture occurs at one end of the ceramic. The other fracture type is a "top of ceramic", where the ceramic layer cracks in the middle rather than at the end. Samples fracturing in the unapproved way have to be replaced until six samples have an "end of ceramic" fracture.[80] Sketches of htese fracture types are given in Figure 2.14 below.

During the debonding testing, the force and deflection are measured. The force at fracture F_{fail} is also recorded. Based on this it is possible to calculate the de-bonding strength τ_b numerically. The full calculation is described in ISO 9693:2019, and an example is given in Appendix B. The calculation of the de-bonding strength is based on Young's modulus of the substructure, the thickness of the substructure and F_{fail}.[80]

Metal-ceramic systems will have different bond strengths depending on the chosen

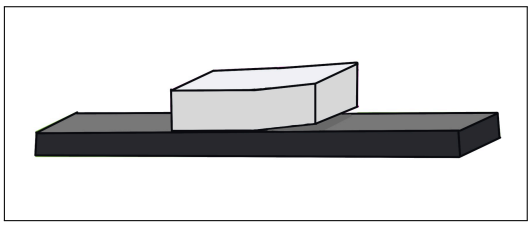

(a) An "end of ceramic" fracture.

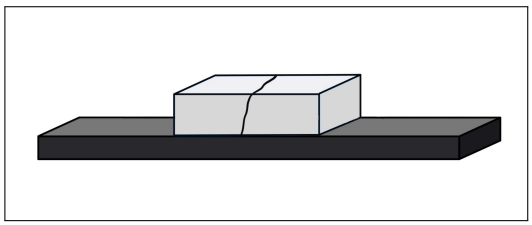

(b) A "top of ceramic" fracture.

Figure 2.14: These sketches show the two possible fracture types, (a) "end of ceramic" and (b) "top of ceramic".

substructure and the porcelain, as well as the processing of the system. One study found that a Ti-6Al-4V alloy combined with dental porcelain had a bond strength of 28.24 MPa, and that this could be improved by adding either a SiO_2 or a SiO_2-TiO_2 sol-gel coating between the metal and the dental porcelain.[81] Another study investigated the behaviour of different porcelain types on commercially pure titanium. The resulting bond strengths varied between 21 ± 3 MPa and 45 ± 5 MPa. For the initial Ti porcelain used in the study a bond strength of 31 ± 5 MPa was reported.[82] Aslan et al.[83] found that grade 5 titanium alloy substrates treated with airborne-particle abrasion prior to coating with dental porcelain had bond strengths of 27.12 ± 7.16 MPa and 29.55 ± 5.54 MPa, for two porcelain types. Based on these studies, porcelains on titanium alloys are not guaranteed to have bond strengths over the 25 MPa criteria in ISO 9693:2019.

2.8 Fracture Mechanics of Ceramics

Ceramic materials have a brittle behaviour, Prior to fracture there is no plastic deformation, but some elastic deformation. Ceramics fail when they are under a stress that is greater than their nominal strength.[34] [84]

Processing of ceramics will almost always result in some defects, either from powder composition and compaction, from handling of the ceramic or from the sintering process. Some examples of potential defects are pores, differently sized agglomerates, cracks, scratches, and inhomogeneity. Defects like pores, inclusions, and grains are found in the ceramic body while other defects, like cracks, can be found on the surface. Defects can weaken ceramic materials as stress more easily concentrates around them. Thus, defects result in ceramics fracturing at lower loads than the ideal ceramic could withstand.[34] [84]

The reduction in strength due to defects is affected by different factors. Different elastic modulus between the ceramic body and any inclusions, as well as differences in coefficient of thermal expansion of the two, can increase the strength reduction. The size and shape of inclusions and pores, and the distance between pores and between pores and the surface, will also affect the strength of the ceramic. The placement of pores relative to grain boundaries and cracks is another factor. Cracks close to pores can give a reduction in strength as pores are considered inclusion with zero strength. These pores therefore provide a path for crack propagation with less resistance. On the other hand, inclusions with greater strength than the ceramic

body can deflect crack propagation. Pores will also result in rougher surfaces after polishing.[26] [34]

2.9 Overlapping Signals in Energy Dispersive Spectroscopy

Energy dispersive spectroscopy (EDS) is a characterisation method where a chemical analysis is performed. It is a mostly qualitative method, but semi-quantitative results can be obtained from it. This analysis is often done using SEM instrumentation as these typically have an EDS system as well. The measurement is based on three different signals: secondary and backscattered electrons, and X-rays. Of these it is the X-rays that are used for the identification of elements.[85]

It is therefore possible to do an elemental analysis since each element will send out a X-ray signal unique to itself. However, there are limitations to this method. The energy resolution can be as low as 150 eV. If the X-rays the elements emit have very similar wavelengths, their signals can overlap. This makes it difficult to separate some elements.[86] The characteristic energies of the relevant elements in this project are given in Table 2.4.

EDS can measure both major and minor elements. The major elements are present in concentrations above 10 wt%, while the minor elements are present in concentrations between 1 and 10 wt%. EDS is therefore not able to identify trace elements.[85]

Table 2.4: The characteristic X-ray energy of relevant elements.[87]

Element	keV	Series
Al	1.486	K_α
Ba	4.465	L_α
C	0.277	K_α
Ca	3.690	K_α
F	0.677	K_α
K	3.312	K_α
La	4.650	L_α
Mg	1.253	K_α
N	0.392	K_α
Na	1.041	K_α
O	0.525	K_α
Si	1.739	K_α
Sr	1.806	L_α
Ti	4.508	K_α
V	4.949	K_α
Zr	2.042	L_α

3 Experimental

3.1 Materials and Apparatus

An overview of the materials and apparatus used in this project are given in Table 3.1 and Table 3.2, respectively. The materials have been used for solid state synthesis of a $(Ba_{0.85}Ca_{0.15})(Zr_{0.1}Ti_{0.9})O_3$ (BCZT) powder as well as preparation of the metal substrates and the coatings. In addition to the listed apparatus, some software have been used. *EVA* has been used for XRD measurements, *testXpert III* software was used for measurements during the Schwickerath adhesion test, and the *aixPlorer* software was used during piezoelectrical evaluation.

Table 3.1: List of chemicals and materials used in this project. Manufacturer, LOT number, purity and purpose are given for each material where relevant.

Materials	**Manufacturer**	**LOT nr.**	**Purity** [%]	**Purpose**
$BaCO_3$	Sigma Aldrich	22734	99.98	Precursor
$CaCO_3$	Sigma Aldrich	SLBC8690V	>99	Precursor
ZrO_2	Alfa Aesar	25231B	99.98	Precursor
TiO_2	Sigma Aldrich	MKCD6078	99.80	Precursor
Initial Ti Bonder	GC	2101121	N.A	Coating
Initial Ti-bonder liquid	GC	2009011	N.A	Coating
Initial D-A3 Ti Dentin	GC	2103051	N.A	Coating
Initial Ti-modelling liquid	GC	2009291	N.A	Coating
Korox 110 µm	Bego	-	-	Sandblasting
DP-Spray P 3 µm	Struers	-	-	Lubricant, polishing
DP-Spray P 1 µm	Struers	-	-	Lubricant, polishing
Auromal 50L Silberleitlack	Ami Doduco	-	-	Silver electrodes

Table 3.2: List of the apparatus used in this project including the model, manufacturer and purpose.

Apparatus	Model	Manufacturer	Purpose
Termaks oven	-	Termaks	Drying precursors
Planetary ball mill	PM 100	RETSCH	Milling powder
Rotary evaporator	R-210	BUCHI	Drying mixture
Uniaxial press	K2500/S3-S40 HV	mäder pressen	Pressing pellets
Digital sensor	8451-6020	Burster	Monitor force
Diamond wire saw	Well 3500	Well	Cut samples
LaboPol 21		Struers	Polishing
Sintering furnace	Super Kanthal	Entech	Calcination, sintering
FEG-SEM	Ultra 55	Zeiss	Characterisation
PSD analyzer	Partica LA-960	Horiba	Characterisation
X-ray Diffractometer	D8 A25 DaVinci	Bruker	Characterisation
Furnace	Commodore 100 VPF	Jelenko	Firing coatings
Dental laboratory handpiece	Perfecta 600	W&H	Grinding coatings
Steam cleaner	Steamer X3	Amann Girrbach	Cleaning substrates
Sandblasting unit	Basic quattro IS	Renfert	Sandblasting substrates
Materials testing machine	ZwickiLine Z5.0	ZwickRoell	Adhesion test
BET analyser	3Flex 3500	Micromeritics	BET analysis
Degas unit	Degas Smartprep for 3Flex	Micromeritics	Degas powder
Piezoelectrical tester	AIX PES	AIXACCT Systems	Piezoelectrical evaluation
Berlincourtmeter	YE2730A d_{33} meter	Sinocera	Piezoelectrical evaluation

3.2 Methods

3.2.1 Solid-State Synthesis of BCZT

In this project a calcium-zirconium doped barium-titanate (BCZT) powder was made with the following composition, $(Ba_{0.85}Ca_{0.15})(Zr_{0.1}Ti_{0.9})O_3$, through solid-state synthesis. One portion of the BCZT powder was only calcined and then used to make BCZT/Porcelain coatings while the other portion of the powder was

sintered as pellets. Four precursors ($BaCO_3$, $CaCO_3$, ZrO_2, TiO_2) were used for the synthesis. Three batches of BCZT powder was made, with different particle sizes. The calculations of precursor amounts are given in Appendix B. The general procedure for the synthesis is described. The exact procedure for each powder is illustrated in the flowchart in Figure 3.1.

First, precursors were weighed out into separate crucibles for each precursor. The mass of precursors used for each powder are given in Table 3.3. Precursors for batch α and β were weighed out together. The crucibles were placed in a Termaks oven at 110 °C to dry the precursors overnight. Stoichiometric amounts of the dried precursors were then weighed out and milled using a planetary ball mill for 1 hour at 150 rpm. A 250 mL milling jar was used, filled with 90 mL of 3 mm diameter YSZ balls. Pure ethanol was added until all the milling media and the precursors were covered. After milling, the powder suspension was transferred into a rotary evaporator flask. A sieve was used to separate the milling media from the suspension. The suspension was dried with a rotary evaporator at 175 mbar with a 60 °C water bath. The dried powder was lightly ground with a mortar and pestle to break any soft agglomerates before it was sieved through a 250 µm sieve.

Table 3.3: The amount used of each precursor for each batch. The precursors for batches α and β were weighed out together.

Precursor	$\mathbf{m}_\alpha$ [g]	$\mathbf{m}_\beta$ [g]	$\mathbf{m}_\gamma$ [g]
$BaCO_3$	7.4697	7.4697	8.9572
$CaCO_3$	0.6755	0.6755	0.8150
ZrO_2	0.5492	0.5492	0.6643
TiO_2	3.2069	3.2069	3.8769

The powder was uniaxially pressed into pellets with a diameter of 25 mm with a force of approximately 5kN, which equals to around 10 MPa. The conversion from MPa to kN is given in Appendix B. Each pellet weighed approximately 1 gram before calcination. The pellets were stacked in two platinum crucibles together with some sacrificial powder on the bottom of the crucible as well as covering the samples. The calcination was done in a Super Kanthal oven, the temperature program used for the calcination is given in Table 3.4. The pellets were weighed and the diameter measured before and after calcination. The calcined pellets were first crushed in a pellet crusher then milled in a planetary ball mill at 150 rpm. The milling time is specified for each powder in Figure 3.1. A 250 mL milling jar was used, filled with 60 mL of 3 mm diameter YSZ balls, which was then covered with 96% ethanol. After milling the powder was dried in a rotary evaporator as described for the precursors before it was sieved through a 250 µm sieve. The powder was then characterised with X-ray diffraction and Scanning Electron Microscope imaging, and the particle size distribution was measured using the Horiba PSD analyzer. For the β and γ batches, a BET analysis was also done.

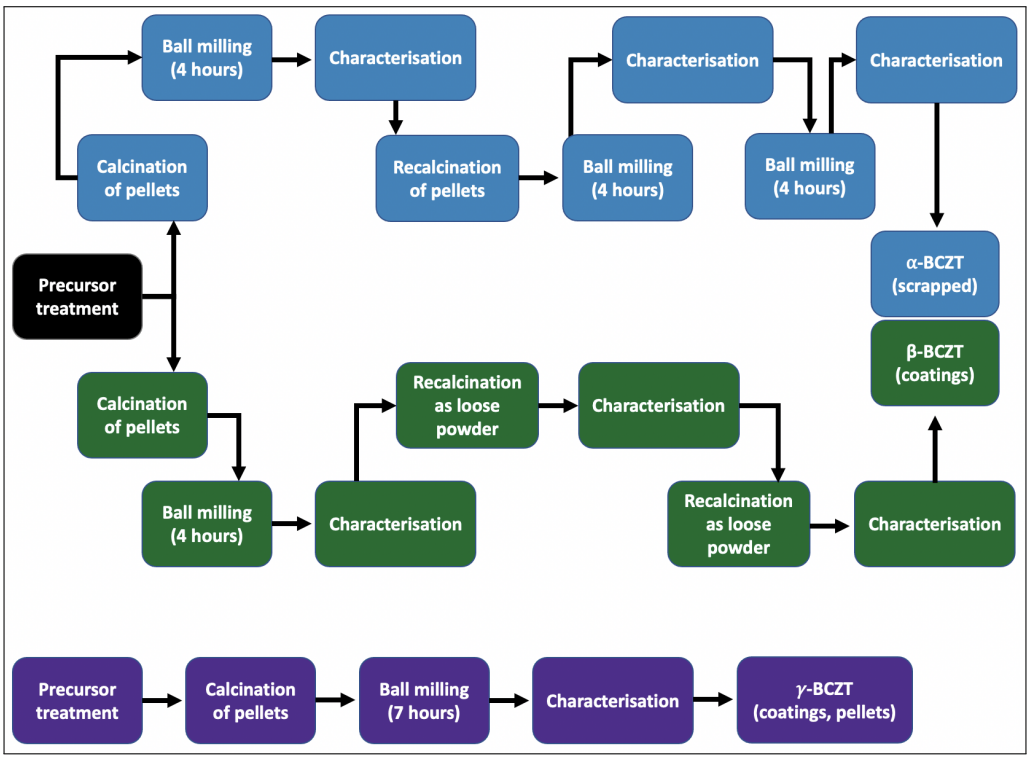

Figure 3.1: Flowchart of the solid-state synthesis of the three powder batches. The milling time is specified for each powder as well as the final use of the powder.

For the α-BCZT powder there were some peaks present in the XRD diffractogram that did not correspond to BCZT, thus there were some impurities in the powder. The average particle size was around 200 µm. Because of this the calcined powder was pressed into new pellets and a recalcination was done. All recalcinations followed the calcination temperature program. After recalcination and milling the particle size was around 100 µm. The powder was ball milled once again. Characterisation showed that there were still impurities and that the particle size was around 1 µm. There was some loss of powder after each milling and drying step. The total loss of powder in the α batch, combined with the impurities resulted in this batch being scrapped.

The XRD analysis of the β batch showed some impurities after the first calcination. The powder was recalcined as a loose powder. The subsequent characterisation still showed impurities and the powder was recalcined once more as loose powder. The weight of the powder before and after each calcination is given in Table A.2. The powder was characterised again after the second recalcination.

After calcination of the γ batch, the pellets from one of the crucibles were visibly curved. This is shown in Figure 3.2.

Some of the BCZT-powder was pressed into pellets and sintered. First, three pellets of γ-BCZT were pressed using the uniaxial press and 0.8 kN force, which corresponds to around 10 MPa. Approximately 0.5 g powder was used to make the pellets, which had a diameter of 10 mm. The pellets were then pressed again using a cold isostatic press (CIP), at 2 kbar for 1 minute. An attempt was also made to press similar

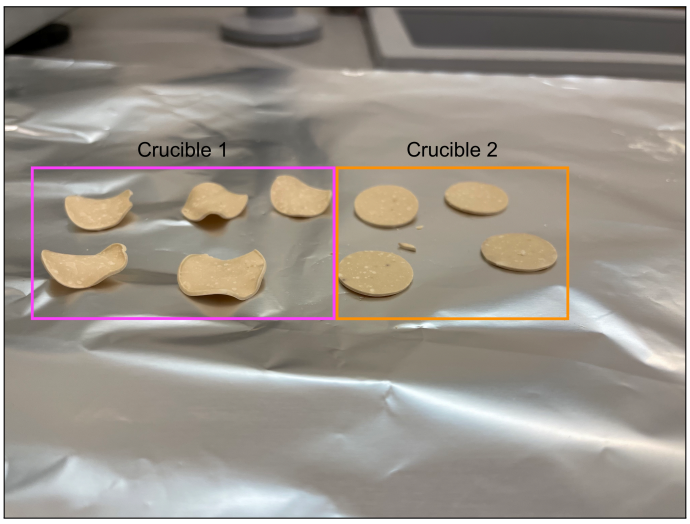

Figure 3.2: The calcined pellets made with γ-BCZT, where one half of the pellets are curved.

Table 3.4: Temperature programs for calcination and sintering of BCZT.

Procedure	**HR** [°C/**hour**]	$\mathbf{T_{max}}$ [°C]	$\mathbf{t_{hold}}$ [**Hours**]	**CR** [°C/**hour**]
Calcination	350	1300	2	400
Sintering	350	1450	3	400

pellets of the β-BCZT powder. However, even after increasing the force to 5.3 kN the pellets did not hold together. It was therefore decided to move forward with only the pellets made of γ-BCZT.

The pressed pellets were placed in a platinum crucible with sacrificial powder in the Super Kanthal oven for sintering. They were sintered at 1450 °C for 3 hours, with a heating rate of 350 °C and a cooling rate of 400 °C. The temperature program is given in Table 3.4. The weight and dimension of the pellets were measured before and after sintering. These measurements are given in Table A.3.

3.2.2 Characterisation of Powder and Pellets

Four methods were used to characterise the BCZT powders; X-ray diffraction (XRD), Scanning electron microscope (SEM) imaging, particle size distribution (PSD) measurements and BET analysis.

XRD Analysis

All XRD analyses were performed using the DaVinci1 instrument with Cu K_α radiation at wavelength 1.54 Å. The analysis was a 0.2 degree FS-XRD done over 2 hours for the 2Θ range 10 - 80°. A XRD analysis was also done on one of the pellets, using the same scan program as for the powders.

SEM Imaging

The SEM imaging was done on the Zeiss Ultra 55 FEG-SEM to confirm particle sizes and morphology of the powder. The images were taken using secondary electrons (SE), a 30 µm aperture, 5.0 kV voltage, and a working distance of approximately 10 mm. Images were taken at a range of different magnifications. For imaging of powder, the powder was first suspended in ethanol as described for particle size distribution (PSD) measurements below. A droplet of this suspension was then added to carbon tape placed on a stub, using a pipette. The stub was placed in the SEM once any liquid had evaporated. The pellets were imaged with SEM to look at the morphology, using secondary electrons (SE), a 30 µm aperture, 5.0 kV voltage, and a working distance of approximately 10 mm.

PSD Measurements

The particle size distribution (PSD) was measured with the Partica LA-960. The measurements were done in ethanol, and the PSD distribution was measured multiple times to ensure reproducible results. For this measurement, approximately half a small plastic spoon of dried, sieved powder was added to a small beaker together with 30 mL 96% ethanol. The beaker was then placed in an ultrasound bath for 30 minutes. Shortly before adding the suspension to the ethanol in the chamber in the instrument, the beaker was moved in a circular motion for 30 seconds. This was done to stir up any particles that had fallen to the bottom of the beaker. A plastic pipette was used to add droplets of the suspension to the chamber until the transmittance was within the acceptable area for the measurement. The liquid in the chamber was continuously stirred during the measurements. First 5 measurements were taken, then the instruments ultrasonic-feature was used for 3 minutes. After the suspension had stabilized again 5 new measurements were taken.

BET Analysis

The BET analysis was done to measure the surface area of the powders. The clean, dry test tubes were first weighed empty. The BCZT powders were then added to one test tube each, the tubes with the powders were then weighed. The tubes were placed in the degas unit, placing the needle approximately 5 cm down into the tube. A rubber cap was used to close the tube and a metallic heat jacket was placed around each tube. The samples were degassed using nitrogen. The conditions for degassing were set using the *TriFlex* software and the degassing program given in Table 3.5. The samples were degassed overnight.

Table 3.5: Degassing program for BET analysis.

T [°C]	**Ramp rate [°C/ min]**	**t_{hold} [min]**
30	10	60
90	10	60
250	10	860
25	10	60

After degassing the tubes were weighed once more. The tubes were then mounted to one port each on the 3Flex 3500 for the BET analysis. An isothermal jacket was

placed around each tube to reduce any temperature gradients in the tubes. A *5 pkt BET* analysis was then run.

Density Measurements of Pellets

The geometrical density of the pellets was determined based on mass and dimensions measured with a caliper. The bulk density, apparent porosity and true porosity were determined using Archimedes' principle. First the dry weight, m_1, of each pellet was measured. The pellets were then placed in a evaporation dish inside a vacuum desiccator. The pressure was dropped to under 25 mbar and held for 20 minutes, using a vacuum pump. The pump was then sealed off from the desiccator and isopropanol was carefully introduced to the evaporation dish through an inlet tube until he pellets were covered by approximately 20 mm of isopropanol. The inlet tube was closed and the vacuum pump was turned on for the desiccator, lowering the pressure again. After 30 minutes the vacuum pump was turned off and air was carefully introduced into the desiccator. The desiccator then sat at ambient pressure for 30 minutes. Each pellet was weighed while immersed in isopropanol (m_2) and after a quick drying with a damp tissue (m_3). The temperature of the isopropanol was recorded for each pellet in order to calculate the correct density of the isopropanol. The measurements of mass and dimensions are given in Table A.3 and Table A.4.

3.2.3 Preparation of BCZT/Porcelain Coatings

Based on previous experience gained during the authors project work it was decided to use a two-layer build-up of the coating to ensure adhesion between the metal substrate and the porcelain coating. Two dental porcelains were used for the coatings, a bonder porcelain and a dentin porcelain. The substrates were made of Ti-6Al-4V, cut according to the dimensions stated in ISO 9693:2019 *Dentistry - Compatibility testing for metal-ceramic and ceramic-ceramic systems*. The required dimensions are (25 ± 1) mm x (3 ± 0.1) mm x (0.5 ± 0.05) mm. The equipment used for substrate preparation and shaping the porcelain green bodies are shown in Figure 3.3. This includes: (A) a Dremel with a rotary burr to grind the surface of the metal substrate, (B) a pink grinding stone used to polish the coatings, (C) a small paint brush, (D) a porcelain brush, (E) a vibrating brush and (F) a small cutting tool.

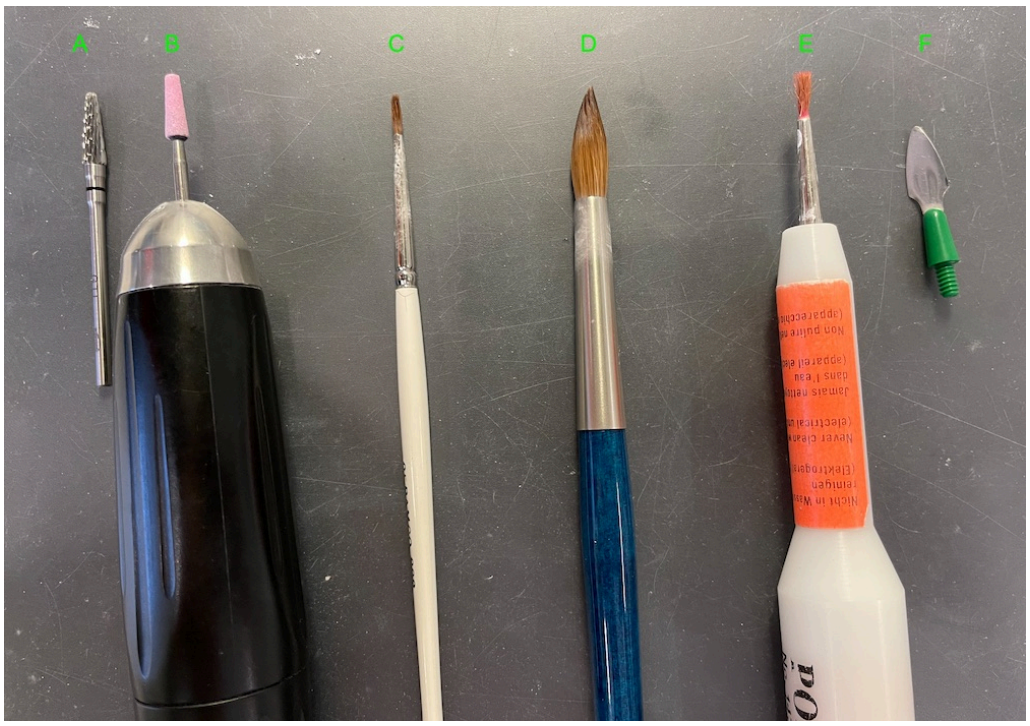

Figure 3.3: The equipment used in the coating process. (A) Rotary burr used with Dremel to grind the substrate surface, (B) Dremel and pink grinding stone used to polish coatings, (C) small paint brush, (D) porcelain brush, (E) vibrating brush, and (F) cutting tool.

First the substrate must be prepared, to remove the existing oxide layer. The metal substrate was lightly ground using a Dremel handpiece, the grinding was done in one direction. Then the ground surface was sandblasted, using Korox 110 µm at 2 bar, until the surface became matted due to the change in roughness. This was followed by immediately steam cleaning the substrates. The procedure for substrate preparation followed the procedure outlined by the supplier of the dental porcelains for optimal adhesion. Once the substrates were steam cleaned a maximum of 15 to 20 minutes passed before the initial layer of porcelain was applied.

The six images in Figure 3.4 show the process from the application of the first porcelain layer, to the firing of this layer, the green body before and after cutting of excess, and lastly to the fired coating before and after polishing.

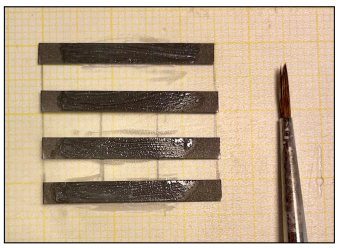

(a) 4 samples where the bonder layer has been applied. Before firing the edges are cleaned up.

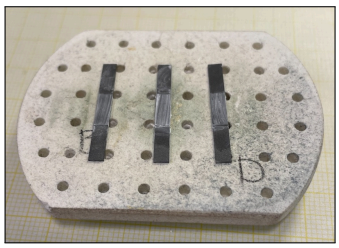

(b) 3 samples where the bonder layer has been fired.

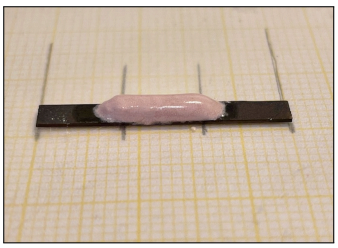

(c) The second layer has been added to the sample.

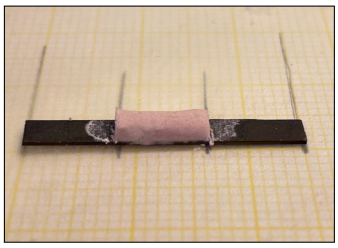

(d) Some excess liquid has been removed from the sample and the edges have been cleaned up.

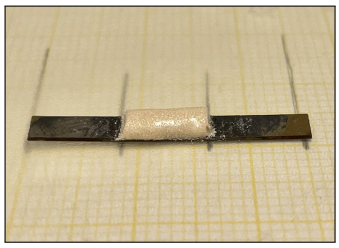

(e) Image of the fired coating sample.

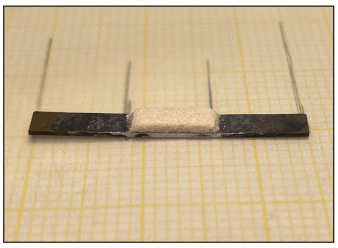

(f) The coating sample after both the sides and the top surface has been polished.

Figure 3.4: Images taken during the coating process.

The initial layer of porcelain was a bonder porcelain. The bonder powder was mixed with its corresponding modelling liquid until the mix was a thin wash. This was then applied onto the substrate with a small paintbrush. For a smooth surface and a sufficiently thin layer of porcelain it was dragged beyond the dimensions stated in ISO 9693:2019. Any excess porcelain was carefully removed using a wet porcelain brush. The substrates were fired in the Jelenko oven according to the bonder firing temperature program given in Table 3.6. The temperature program was given by the supplier of the bonder porcelain. Porcelain firing is often done under vacuum as it can reduce the porosity left in the porcelain after firing.

Table 3.6: Temperature programs for firing of bonder and dentin porcelain.

Porcelain	$\mathbf{T_{Preheat}}$ [°C]	$\mathbf{t_{drying}}$ **[min]**	**HR** [°C/**min**]	**Vacuum**	$\mathbf{T_{Final}}$ [°C]	$\mathbf{t_{hold}}$ **[min]**
Bonder	450	4 min	55	Yes	810	1
Dentin	400	6 min	45	Yes	780	6

The samples were allowed to cool after firing before the second porcelain layer was applied on top of the bonder. 0.14 g of powder was estimated per sample for the second porcelain layer. Seven sets of samples were made in total; one baseline set with no BCZT, two sets with 30 wt% BCZT, two with 40 wt% and two with 50 wt%. These sets are also specified in Table 3.7. For the baseline samples only dentin porcelain powder was used.

For the samples with BCZT, first the BCZT powder and the dentin powder had to

be mixed until a homogeneous mixture formed. The two powders were weighed out before they were mixed with a pestle and mortar. The powder amounts used for each composition are given in Table 3.7. For some of the sets samples were made over multiple days. In those cases the powders have been weighed and mixed each day, thus there are multiple powder weights. The powder mixing was done very lightly for a short amount of time to prevent big changes in particle size while still ensuring a homogeneous mixture. The pink colour of the dentin porcelain powder made it possible to see when the two powders had combined properly. After mixing the powder was transferred to a ceramic palette. For samples with only the dentin porcelain powder, no mixing was necessary and the powder was added directly onto the palette. The modelling liquid corresponding to the dentin porcelain was added to the powder until a thick paste formed. Using a wet porcelain brush, the paste was applied to the sample, on top of the bonder layer. The green body was built up and formed with the porcelain brush. To help the porcelain flow better on top of the bonder layer, and to remove some excess liquid, a vibrating brush was gently placed on the ends of the substrate. The excess liquid was then removed by blotting the sample with tissue paper. Finally the edges of the green body was cleaned up to get the desired shape. This was done using the porcelain brush and a small cutting tool.

Table 3.7: The 7 sets of samples are here listed with the number of samples made, the weight percentage of BCZT, the mass of BCZT and dentin, and the total mass of powder used. There are multiple rows of samples within one set whenever the samples were made over multiple days.

Set	**# of samples**	**wt% BCZT [%]**	$\mathbf{m_{BCZT}}$ **[g]**	$\mathbf{m_{dentin}}$ **[g]**	$\mathbf{m_{total}}$ **[g]**
D-00	10	0	-	1.4	1.4
	8	0	-	1.12	1.12
Dγ-30	10	30	0.42	0.98	1.4
	6	30	0.252	0.588	0.84
Dγ-40	10	40	0.56	0.84	1.4
	3	40	0.168	0.252	0.42
Dγ-50	10	50	0.70	0.70	1.4
Dβ-30	10	30	0.42	0.98	1.4
	3	30	0.126	0.294	0.42
	4	30	0.168	0.392	0.56
Dβ-40	12	40	0.672	1.008	1.68
Dβ-50	12	50	0.84	0.84	1.68

Finally, the samples were fired in the Jelenko oven in accordance with the dentin firing program listed in Table 3.6. All temperatures etc. are taken from the temperature program given by the dentin porcelain supplier except for the holding time at

T_{max} which was 1 minute originally. Some test samples were made with a holding time of 1 minute however, from observations in the SEM it did not look like the dentin had been able to melt properly during the firing. The samples with only dentin and those with dentin and BCZT had significantly different structures after 1 minute. Therefore, a test was done with a holding time of 6 minutes total. After 6 minutes it looked like the dentin had been able to melt and flow, thus it was decided to continue with a 6 minute holding time.

After firing the samples were polished on both the edges and on the surface. Because the porcelain contracts during firing the green body was made to be slightly wider than the substrate. The porcelain was built higher than required in ISO 9693:2019. This was done to ensure that all samples would go through the same treatments prior to testing, as all excess porcelain was removed using a pink stone with the Dremel hand piece. After this polishing step the samples had the shape and dimensions given in Figure 3.5a. The different layers in the final sample are named in Figure 3.5b.

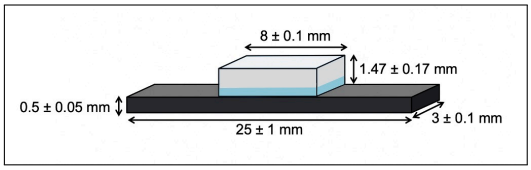

(a) Sketch of the final sample showing the dimensions of the metal substrate and the coating. [30]

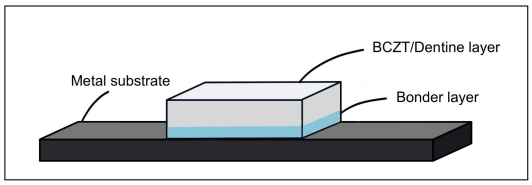

(b) Sketch of the final sample showing the placement of the different layers in the sample and their corresponding names.

Figure 3.5: Two sketches of the final sample showing the dimensions and the different layers.

3.2.4 Characterisation of BCZT/Porcelain Coatings

Debonding Tests According to ISO 9693:2019 - De-bonding/crack-initiation test

Debonding tests of some samples were done at NIOM in accordance with ISO 9693:2019 *Dentistry - Compatibility testing for metal-ceramic and ceramic-ceramic systems* . The testing was done using the Zwick, a figure of the equipment is given in Figure 3.6. The sample was placed in a 3-point bending setup with the coating facing down. A force was applied perpendicularly to the back of the sample with a test speed of 1.5 mm/min and a pre-load of 2 N. This force was increased until the *testXpert III* software measured a 5% decline in force, which is the fracture requirement in ISO 9693:2019. The software measured the force in Newton as a function of the deflection in mm. The fracture mode of each sample was checked afterwards, and confirmed as a "End of ceramic" fracture.

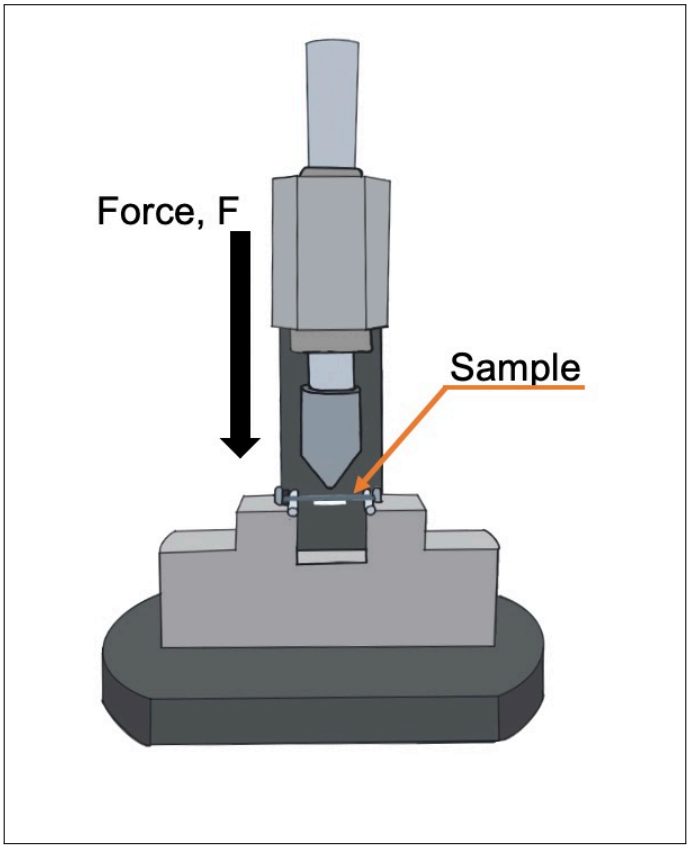

Figure 3.6: Sketch of the equipment used for the adhesion test. The sample was placed in a three-point bend and subjected to a downwards force.[30]

SEM Imaging

SEM images were taken of the cross sections of the coated samples, as well as of the surface and side of a selection of the fractured samples. This was done to see whether the material system behaved differently as the amount of BCZT increased and to confirm the type of fracture from the Schwickerath adhesion test. By imaging the cross sections it was also possible to investigate the metal-ceramic interface to a certain degree. The SEM images were taken with the Zeiss Ultra 55 FEG-SEM, using 30 µm aperture, 5kV, and a SE-source.

Prior to imaging the samples had to be cut in two and the cross section polished. They were cut using the Wells diamond saw. After cutting they were cleaned in ethanol in an ultrasonic bath for 15 minutes. One part of the cut sample was then polished using the LaboPol-21 and by hand, with the grinding surfaces and lubricants listed in Table 3.8. The samples were cleaned in ethanol in an ultrasonic bath for 5 minutes between each polishing step.

XRD Analysis

XRD measurements were performed on one sample from each set of coatings to investigate the chemical composition of the coatings. The measurements were done using the DaVinci1 instrument with Cu K_α radiation at wavelength 1.54 Å. The analysis was a 0.2 degree FS-XRD done over 2 hours for the 2Θ range 10 - 80°.

Table 3.8: Grinding surface, lubricant with particle size, time and instrument are given for each step in the polishing procedure.

Grinding surface	Lubricant	Particle size [µm]	Time [s]	Instrument
SiC paper #1200	Water	-	30	LaboPol-21
SiC paper #4000	Water	-	30	LaboPol-21
MD Nap 3 µm	Diamond particle suspension	3	60	By hand
MD Nap 1 µm	Diamond particle suspension	1	60	By hand

EDS Analysis of the Cross Section

An EDS analysis was done on sample D-00-8, Dγ-30-11 and Dβ-30-7 to look at the chemical composition of the coatings. The analysis was done in the Zeiss Ultra-55 FEG-SEM with a 60 µm aperture, 15 kV voltage and a 10 mm working distance. The cross section of each sample was analysed. The analyses were done both in multiple points on each cross section and as a mapping scan of a section of the cross section.

3.2.5 Characterisation of Piezoelectric Properties

The piezoelectric and ferroelectric properties of the pellets and the coatings were measured in AIX PES and with a Berlincourt-meter. First, a thin silver electrode was painted on each side of the sample and air-dried. The sample was then submerged in a silicone oil bath within the AIX PES set up, at room temperature. The polarisation and strain was measured in a single loop measurement using a triangular waveform and a frequency of 1 Hz. Each sample was tested at multiple voltage amplitudes, with a final amplitude of 1000 V. During these measurements the samples became poled. The piezoelectric coefficient d_{33} and the relative permittivity of the coatings was measured in the AIX PES using a small signal amplitude of 5 V, small signal frequency of 1kHz, and medium integration time. The final d_{33} value for each coating was calculated by averaging the measurements. A total of 100 measurements were taken. The relative permittivity of each coating was calculated based on the measured capacitance, the electrode area and thickness of the sample. The piezoelectric coefficient was also measured using a Berlincourt-meter. This method was used for both the coatings and the pellets. The dried sample was placed between the two contact probes and fastened. The instrument then applied an oscillating force to the sample, which resulted in a piezoelectric response. A sketch of the Berlincourtmeter is shown in Figure 3.7.

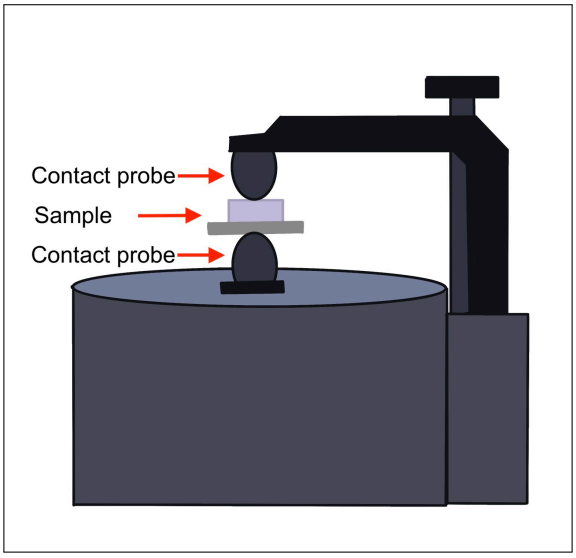

Figure 3.7: Sketch of the Berlincourt-meter with a coating sample fastened between the two contact probes.

3.3 Sample Overview

As previously mentioned, two different dental porcelains have been used together with two different BCZT powders. A bonder porcelain was first applied to the metal substrate. A dentin porcelain was mixed with BCZT powder, then applied on top of the bonder porcelain. The two BCZT powders are named β and γ. They have particle sizes around 150 µm and 1 µm, respectively. The coated samples have been given sample IDs based on the BCZT powder and the amount of BCZT. **One sample ID is Dβ-30-1, where Dβ refers to dentin and β-BCZT, 30 refers to the 30 wt% BCZT in the sample, and 1 is the sample number.**

The set of samples that make up the baseline have no BCZT powder, therefore the sample IDs are D-00-1, D-00-2, etc. An overview of all the samples used in this project is given in Table 3.9 as well as in Figure 3.8. In the table the sample ID, description, preparations done, and measurements done for each sample are listed. Some samples broke in various stages of the process. For these samples "broken" is written in the "Measurements" column. In the flowchart in Figure 3.8 the sample numbers are listed as "(1;18)" etc.

Table 3.9: Overview of all samples used in the project, their composition as well as any preparations and measurements done on the samples.

ID	Description	Preparations	Measurements
D-00-1	0/100 wt% BCZT/dentin	-	Debonding test, SEM
D-00-2	0/100 wt% BCZT/dentin	-	Debonding test
D-00-3	0/100 wt% BCZT/dentin	-	Debonding test
D-00-4	0/100 wt% BCZT/dentin	-	Debonding test
D-00-5	0/100 wt% BCZT/dentin	-	Debonding test
D-00-6	0/100 wt% BCZT/dentin	-	Debonding test

Continued on next page

Table 3.9 *continued from previous page*

ID	Description	Preparations	Measurements
D-00-7	0/100 wt% BCZT/dentin	-	Broken
D-00-8	0/100 wt% BCZT/dentin	Cut, polish	SEM, EDS, XRD
D-00-9	0/100 wt% BCZT/dentin	-	Piezo-test
D-00-10	0/100 wt% BCZT/dentin	-	Broken
D-00-11	0/100 wt% BCZT/dentin	-	Piezo-test
D-00-12	0/100 wt% BCZT/dentin	-	Broken
D-00-13	0/100 wt% BCZT/dentin	-	Piezo-test
D-00-14	0/100 wt% BCZT/dentin	-	Broken
D-00-15	0/100 wt% BCZT/dentin	-	Debonding test
D-00-16	0/100 wt% BCZT/dentin	-	Debonding test
D-00-17	0/100 wt% BCZT/dentin	-	Broken
D-00-18	0/100 wt% BCZT/dentin	-	Debonding test
Dγ-30-1	30/70 wt% γ-BCZT/dentin	-	Debonding test, SEM
Dγ-30-2	30/70 wt% γ-BCZT/dentin	-	Debonding test
Dγ-30-3	30/70 wt% γ-BCZT/dentin	-	Debonding test
Dγ-30-4	30/70 wt% γ-BCZT/dentin	-	Debonding test
Dγ-30-5	30/70 wt% γ-BCZT/dentin	-	Debonding test
Dγ-30-6	30/70 wt% γ-BCZT/dentin	-	Debonding test
Dγ-30-7	30/70 wt% γ-BCZT/dentin	-	Broken
Dγ-30-8	30/70 wt% γ-BCZT/dentin	-	Broken
Dγ-30-9	30/70 wt% γ-BCZT/dentin	-	Debonding test
Dγ-30-10	30/70 wt% γ-BCZT/dentin	-	Broken
Dγ-30-11	30/70 wt% γ-BCZT/dentin	Cut, polish	SEM, XRD
Dγ-30-12	30/70 wt% γ-BCZT/dentin	-	Broken
Dγ-30-13	30/70 wt% γ-BCZT/dentin	-	Broken
Dγ-30-14	30/70 wt% γ-BCZT/dentin	-	Piezo-test
Dγ-30-15	30/70 wt% γ-BCZT/dentin	-	Piezo-test
Dγ-30-16	30/70 wt% γ-BCZT/dentin	-	Debonding test, SEM
Dγ-40-1	40/60 wt% γ-BCZT/dentin	-	Debonding test, SEM
Dγ-40-2	40/60 wt% γ-BCZT/dentin	-	Debonding test, SEM
Dγ-40-3	40/60 wt% γ-BCZT/dentin	-	Debonding test
Dγ-40-4	40/60 wt% γ-BCZT/dentin	-	Debonding test
Dγ-40-5	40/60 wt% γ-BCZT/dentin	-	Debonding test
Dγ-40-6	40/60 wt% γ-BCZT/dentin	-	Debonding test
Dγ-40-7	40/60 wt% γ-BCZT/dentin	Cut, polish	SEM, XRD
Dγ-40-8	40/60 wt% γ-BCZT/dentin	-	Piezo-test
Dγ-40-9	40/60 wt% γ-BCZT/dentin	-	Piezo-test
Dγ-40-10	40/60 wt% γ-BCZT/dentin	-	Piezo-test
Dγ-40-11	40/60 wt% γ-BCZT/dentin	-	Debonding test
Dγ-40-12	40/60 wt% γ-BCZT/dentin	-	Broken
Dγ-40-13	40/60 wt% γ-BCZT/dentin	-	Broken
Dγ-50-1	50/50 wt% γ-BCZT/dentin	-	Debonding test, SEM

Continued on next page

Table 3.9 *continued from previous page*

ID	Description	Preparations	Measurements
Dγ-50-2	50/50 wt% γ-BCZT/dentin	-	Debonding test
Dγ-50-3	50/50 wt% γ-BCZT/dentin	-	Debonding test
Dγ-50-4	50/50 wt% γ-BCZT/dentin	-	Debonding test
Dγ-50-5	50/50 wt% γ-BCZT/dentin	-	Debonding test
Dγ-50-6	50/50 wt% γ-BCZT/dentin	-	Piezo-test
Dγ-50-7	50/50 wt% γ-BCZT/dentin	-	Piezo-test
Dγ-50-8	50/50 wt% γ-BCZT/dentin	-	Piezo-test
Dγ-50-9	50/50 wt% γ-BCZT/dentin	-	Debonding test
Dγ-50-10	50/50 wt% γ-BCZT/dentin	Cut, polish	SEM, XRD
Dβ-30-1	30/70 wt% β-BCZT/dentin	-	Debonding test
Dβ-30-2	30/70 wt% β-BCZT/dentin	-	Debonding test
Dβ-30-3	30/70 wt% β-BCZT/dentin	-	Debonding test
Dβ-30-4	30/70 wt% β-BCZT/dentin	-	Debonding test, SEM
Dβ-30-5	30/70 wt% β-BCZT/dentin	-	Debonding test
Dβ-30-6	30/70 wt% β-BCZT/dentin	-	Debonding test
Dβ-30-7	30/70 wt% β-BCZT/dentin	Cut, polish	SEM, XRD
Dβ-30-8	30/70 wt% β-BCZT/dentin	-	Broken
Dβ-30-9	30/70 wt% β-BCZT/dentin	-	Broken
Dβ-30-10	30/70 wt% β-BCZT/dentin	-	Broken
Dβ-30-11	30/70 wt% β-BCZT/dentin	-	Piezo-test
Dβ-30-12	30/70 wt% β-BCZT/dentin	-	Broken
Dβ-30-13	30/70 wt% β-BCZT/dentin	-	Piezo-test
Dβ-30-14	30/70 wt% β-BCZT/dentin	-	Debonding test
Dβ-30-15	30/70 wt% β-BCZT/dentin	-	Broken
Dβ-30-16	30/70 wt% β-BCZT/dentin	-	Broken
Dβ-30-17	30/70 wt% β-BCZT/dentin	-	Debonding test
Dβ-40-1	40/60 wt% β-BCZT/dentin	-	Debonding test, SEM
Dβ-40-2	40/60 wt% β-BCZT/dentin	-	Debonding test, SEM
Dβ-40-3	40/60 wt% β-BCZT/dentin	-	Debonding test
Dβ-40-4	40/60 wt% β-BCZT/dentin	-	Debonding test
Dβ-40-5	40/60 wt% β-BCZT/dentin	-	Debonding test
Dβ-40-6	40/60 wt% β-BCZT/dentin	-	Debonding test
Dβ-40-7	40/60 wt% β-BCZT/dentin	Cut, polish	SEM, XRD
Dβ-40-8	40/60 wt% β-BCZT/dentin	-	Broken
Dβ-40-9	40/60 wt% β-BCZT/dentin	-	Piezo-test
Dβ-40-10	40/60 wt% β-BCZT/dentin	-	Piezo-test
Dβ-40-11	40/60 wt% β-BCZT/dentin	-	Piezo-test
Dβ-40-12	40/60 wt% β-BCZT/dentin	-	Debonding test
Dβ-50-1	50/50 wt% β-BCZT/dentin	-	Debonding test, SEM
Dβ-50-2	50/50 wt% β-BCZT/dentin	-	Debonding test
Dβ-50-3	50/50 wt% β-BCZT/dentin	-	Debonding test
Dβ-50-4	50/50 wt% β-BCZT/dentin	-	Debonding test

Continued on next page

Table 3.9 *continued from previous page*

ID	Description	Preparations	Measurements
Dβ-50-5	50/50 wt% β-BCZT/dentin	-	Debonding test
Dβ-50-6	50/50 wt% β-BCZT/dentin	-	Debonding test
Dβ-50-7	50/50 wt% β-BCZT/dentin	Cut, polish	SEM, XRD
Dβ-50-8	50/50 wt% β-BCZT/dentin	-	Broken
Dβ-50-9	50/50 wt% β-BCZT/dentin	-	Piezo-test
Dβ-50-10	50/50 wt% β-BCZT/dentin	-	Piezo-test
Dβ-50-11	50/50 wt% β-BCZT/dentin	-	Piezo-test
Dβ-50-12	50/50 wt% β-BCZT/dentin	-	-

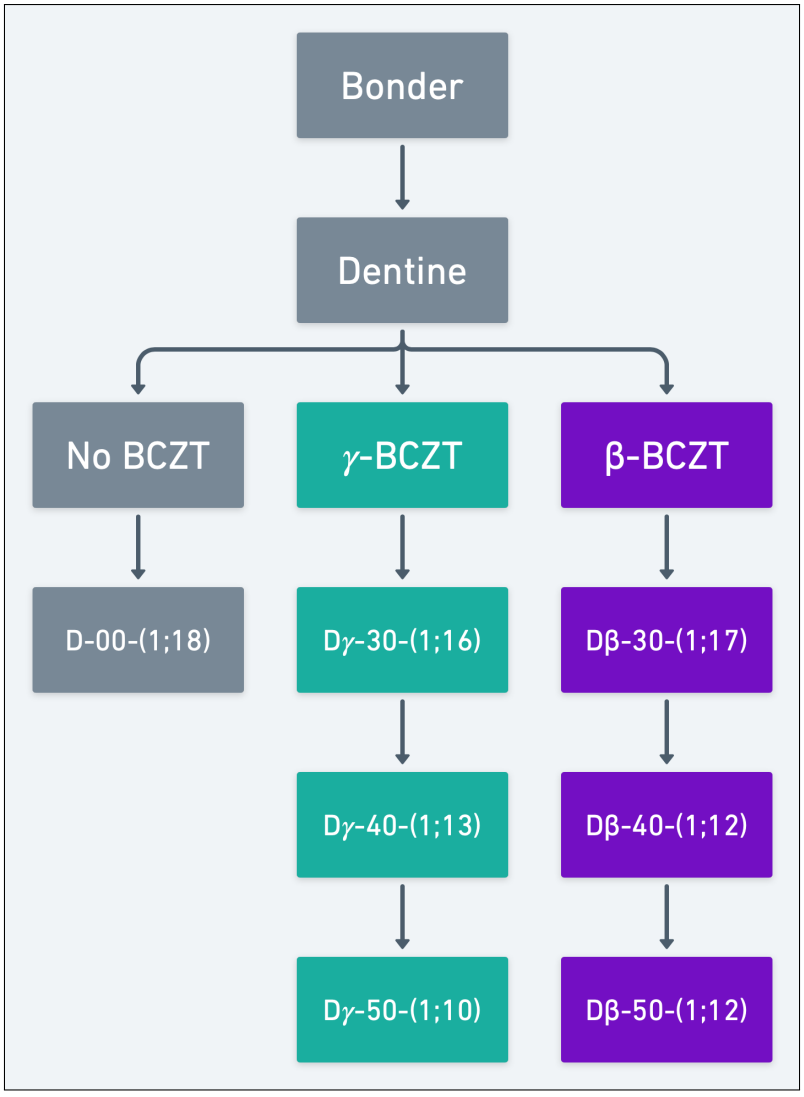

Figure 3.8: Flowchart of the different sets of samples made in this project.

4 Results

4.1 Solid-State Synthesis of BCZT

In total, three different batches of $(Ba_{0.85}Ca_{0.15})(Zr_{0.1}Ti_{0.9})O_3$ (BCZT) powder were made. The first batch, α-BCZT was characterised but not used further for coatings or pellets. All the characterisation results for this powder have therefore been placed in Appendix C (SEM images), E (PSD measurements), and G (XRD analysis). The second (β) and third batch (γ) were both processed with solid-state synthesis however, the β-BCZT powder has a longer total calcination time than the γ-BCZT powder. Some of the γ-BCZT powder has been used to press and sinter pellets.

4.1.1 X-Ray Diffraction Analysis of Powders

An XRD analysis of both β- and γ-BCZT was performed to confirm their compositions after calcination. The resulting diffractograms are given in Figure 4.1 and Figure 4.2, respectively. The *Diffrac.EVA* software was used to confirm whether the powders had the desired composition of $(Ba_{0.85}Ca_{0.15})(Zr_{0.1}Ti_{0.9})O_3$. In the diffractogram for β-BCZT a few peaks that do not match the PDF for $(Ba_{0.85}Ca_{0.15})(Zr_{0.1}Ti_{0.9})O_3$ can be observed. These peaks are present at approximately 30°, 34°, 44°, 47°, 54° and 59°. They were matched with $Ba_{0.8}Ca_{0.2}ZrO_3$ (PDF 04-010-6401) and $Ca_{0.975}Zr_{0.864}Ti_{21.45}O_7$ (PDF 01-074-0669). These compounds have been named BCZO and CZTO in Figure 4.1. Note that the intensity values for the PDFs have been normalized such that the intensities should not be compared across the different PDFs. There are no such peaks present in the diffractogram for γ-BCZT, suggesting that the powder has the desired composition. All the characteristic peaks for BCZT are present in both BCZT powders.

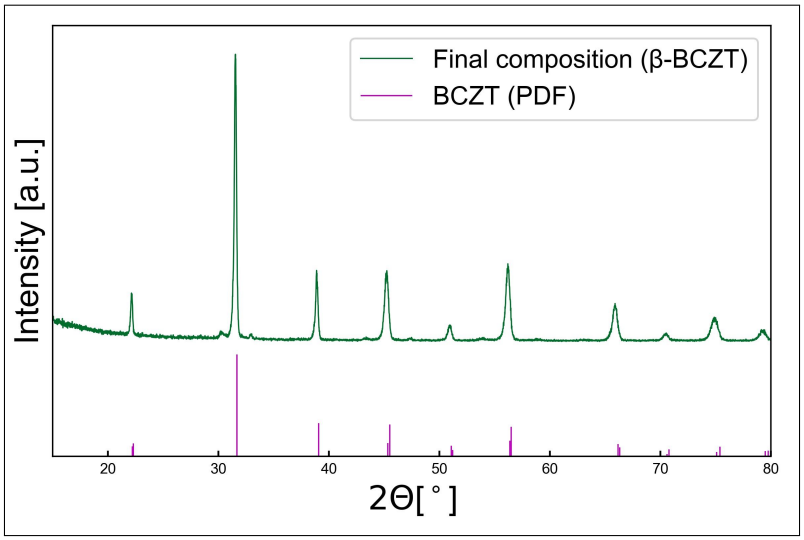

Figure 4.1: Diffractogram of β-BCZT powder, with the PDF for BCZT (PDF 01-086-8334), $Ba_{0.8}Ca_{0.2}ZrO_3$ (BCZO) (PDF 04-010-6401) and $Ca_{0.975}Zr_{0.864}Ti_{21.45}O_7$ (CZTO) (PDF 01-074-0669).

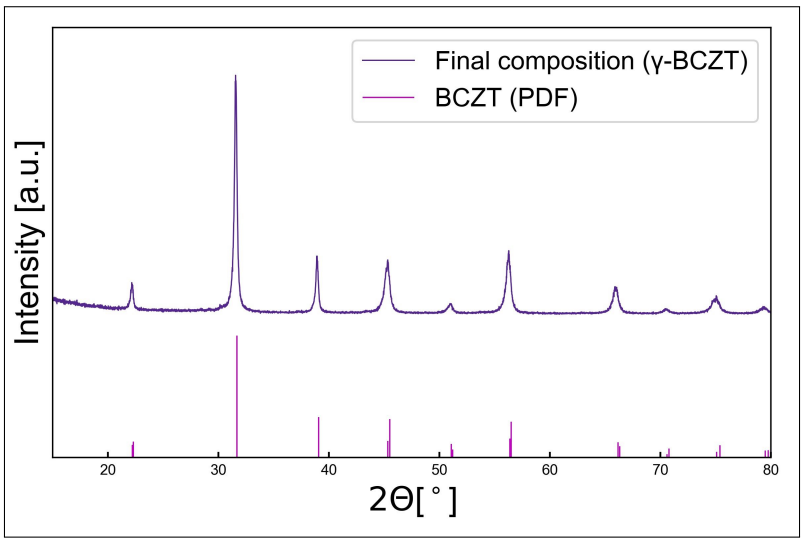

Figure 4.2: Diffractogram of γ-BCZT powder, together with the PDF for BCZT (PDF 01-086-8334)

4.1.2 Particle Size Distribution of Powders

The goal of the synthesis was two BCZT powders with different particle sizes. The particle size distribution was measured five times for each powder. All five measurements can be found in Figure E.2b and Figure E.3 for β- and γ-BCZT, respectively. One representative measurement of each powder is shown in Figure 4.3. The β-BCZT powder (Figure 4.3a) shows a broad particle size distribution, with particles between approximately 1 µm and 350 µm. The mean particle size is around 200 µm. From the curve in Figure 4.3b, it can be seen that the γ-BCZT powder has a more narrow distribution with the mean particle size around 1 µm. Some particles are up to 10 µm in diameter.

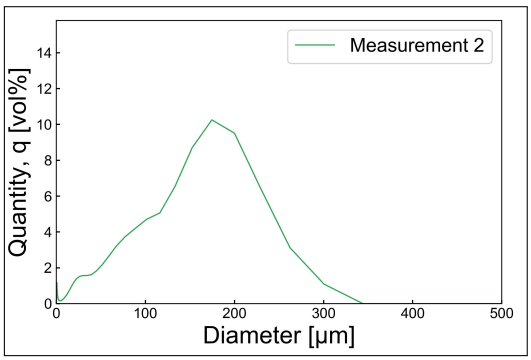

(a) Measurement nr. 2 of the particle size distribution of β-BCZT.

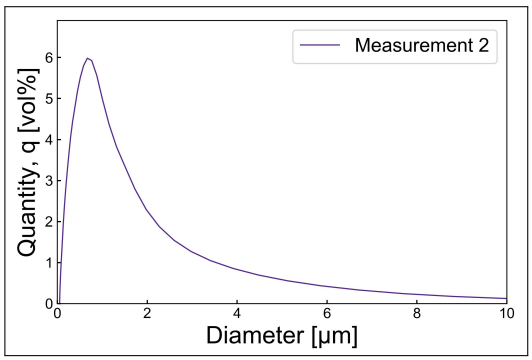

(b) Measurement nr. 2 of the particle size distribution of γ-BCZT.

Figure 4.3: Particle size distribution for both β-BCZT and γ-BCZT. Multiple measurements were done to ensure that they are reproducible, here one measurement is shown.

4.1.3 BET Analysis of Powders

The surface area of the two BCZT powders was measured in a BET analysis. The weight of the empty tubes, tubes with sample before and after degas, as well as the mass of the sample are given in Table 4.1 for both the γ- and the β-BCZT powders. The results are given in Table 4.2 below. From this it is clear that the β-BCZT powder has a significantly lower specific surface area than the γ-BCZT powder. This corresponds with the PSD measurements showing that the β-BCZT has a larger particle size than the γ-BCZT powder.

Table 4.1: Weight of both BCZT powders during BET analysis.

Powder	$\mathbf{m_{empty\ tube}}$ **[g]**	$\mathbf{m_{tube+sample}}$ **[g]**	$\mathbf{m_{degas}}$ **[g]**	$\mathbf{m_{sample}}$ **[g]**
γ-BCZT	35.9563	38.6389	38.6152	2.6589
β-BCZT	36.2869	39.7877	39.7815	3.4946

Table 4.2: The specific surface area of β- and γ-BCZT powder, measured in a BET analysis.

Powder	**Specific surface area** $\mathbf{[m^2/g]}$
β-BCZT	0.7939
γ-BCZT	8.8371

4.1.4 Scanning Electron Microscope Imaging of Powders

The morphology and size of the BCZT particles were characterised using a FEG-SEM. As stated previously, all images of the α-BCZT powder can be found in Appendix C, in Figure C.1. SEM images of β-BCZT and γ-BCZT are given in Figure 4.4 and Figure 4.5, respectively. The images are taken with 10 000X and 22 000X magnification. Both powders have small and larger particles present, with some of the larger particles looking more like chunks of a broken pellet rather than an actual powder particle. The particles in the γ-BCZT powder are more even in size compared to the β-BCZT powder, but still with some agglomerates and chunks.

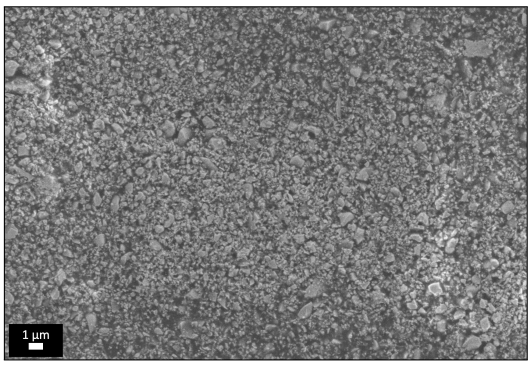

(a) SEM image of β-BCZT, taken at 10 000X magnification.

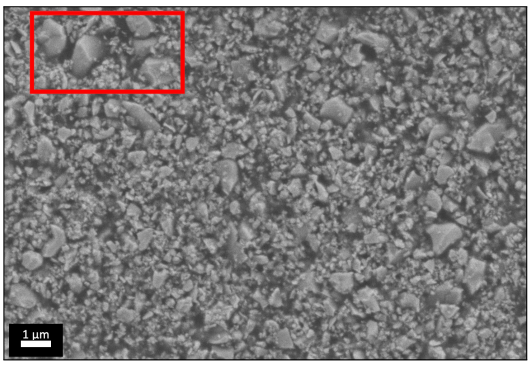

(b) SEM image of β-BCZT, taken at 22 000X magnification.

Figure 4.4: SEM images of β-BCZT powder, taken at 10 000X and 22 000X magnification.

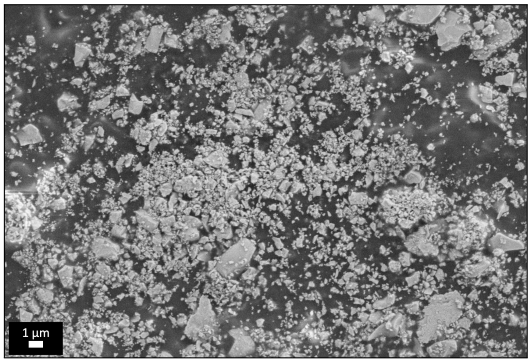

(a) SEM image of γ-BCZT, taken at 10 000X magnification.

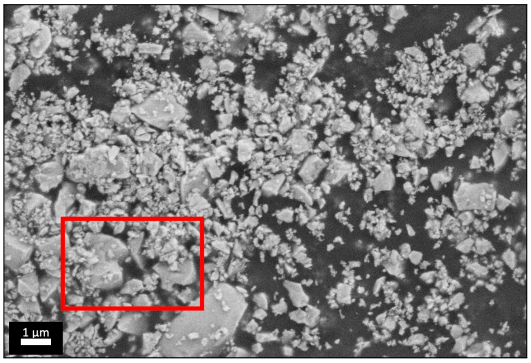

(b) SEM image of γ-BCZT, taken at 22 000X magnification.

Figure 4.5: SEM images of γ-BCZT powder, taken at 10 000X and 22 000X magnification.

4.1.5 X-Ray Diffraction Analysis of Pellets

One of the pellets, Pγ-3 was analysed with XRD, resulting in the diffractogram given in Figure 4.6. The diffractogram for the γ-BCZT powder is also given in the same figure, to compare the composition before and after sintering. Finally, the PDF of BCZT (PDF 01-086-8334) is also given in the figure. The characteristic peaks for BCZT are present in both the diffractograms. The peaks in the diffractogram for the pellet are narrower than for the powder. There are no peaks present that do not match with the PDF for BCZT.

4.1.6 Scanning Electron Microscope Imaging of Pellets

The as-sintered surface of the pellets have been imaged with SEM to get a better understanding of the morphology, especially in terms of porosity. The SEM images of Pγ-1, Pγ-2, Pγ-3 are given in Figure 4.7, 4.8, and 4.9, respectively. Additional images of Pγ-1 and Pγ-2 are given in Figure C.9.

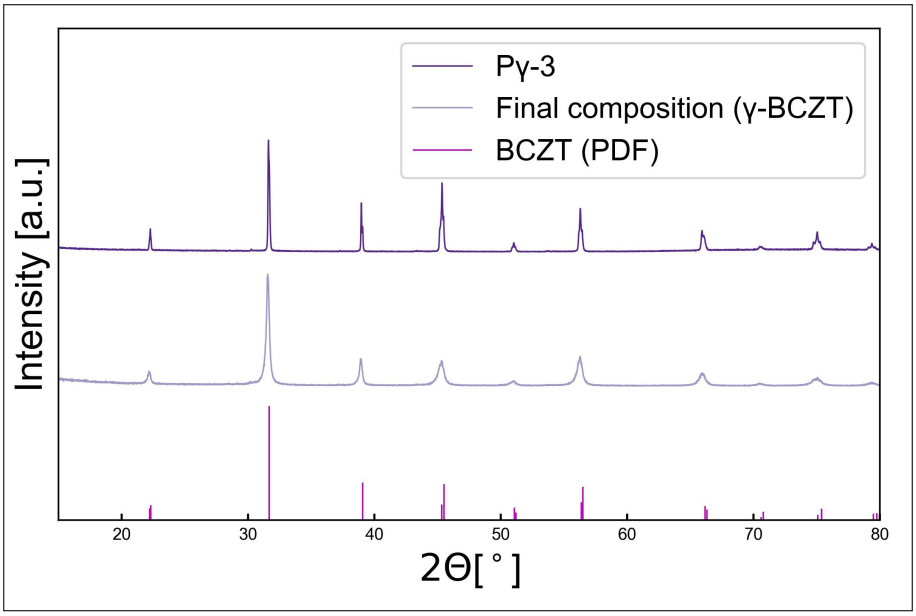

Figure 4.6: Diffractogram of pellet Pγ-3, as well as the γ-BCZT powder and the PDF of BCZT (PDF 01-086-8334)

In both Pγ-1 and Pγ-2 there are larger pores on the surface where you can see the grains below the pores. There seems to be some height differences in the surface topography, which is more visible in Pγ-2 than in Pγ-1. The two pellet have similar sized grains, with some grain size variation within each pellet. There is some porosity visible along the grain boundaries in both pellets.

It is more difficult to say something about Pγ-3 due to the quality of the images. From the images it looks like this pellet is less conductive than the other two pellets even though they underwent the same preparations prior to SEM imaging. This resulted in some very bright areas and some darker areas, as well as difficulty finding focus. However, it is still possible to see that there are some height differences on the surface as well as some pores. There is one large pore going across the bottom right corner of Figure 4.9a. The grains in Pγ-3 have similar shapes as the grains in the other two pellets.

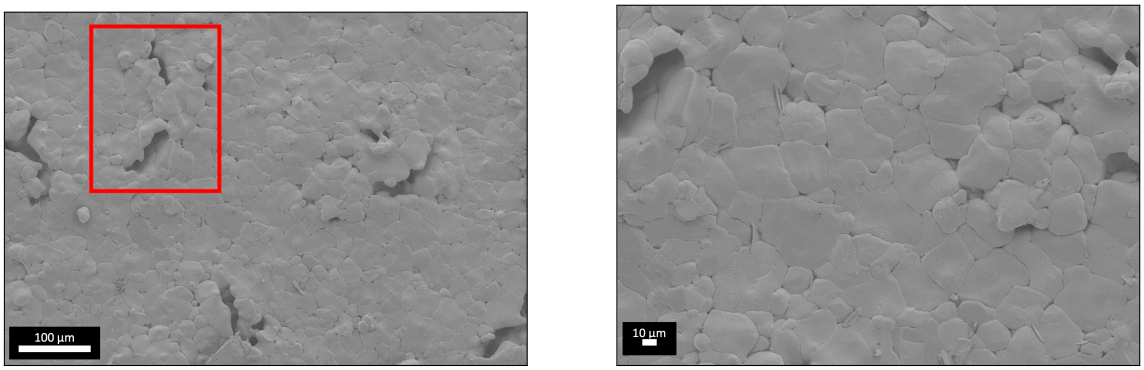

(a) Taken at 500X magnification.

(b) Taken at 1000X magnification.

Figure 4.7: SEM images of pellet Pγ-1.

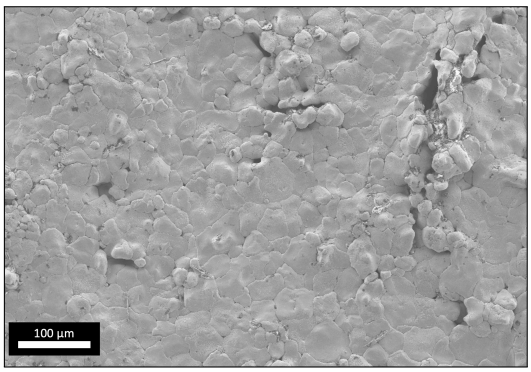

(a) Taken at 500X magnification.

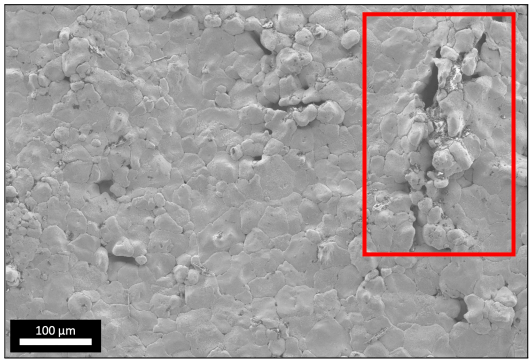

(b) Taken at 1000X magnification.

Figure 4.8: SEM images of pellet Pγ-2.

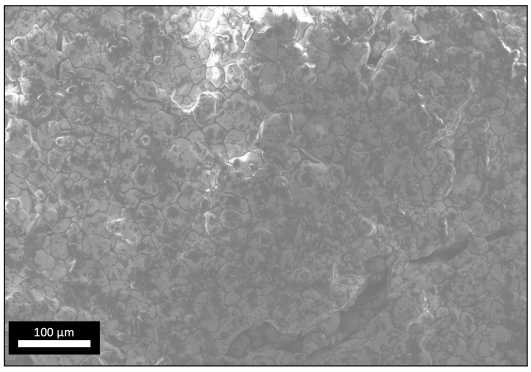

(a) Taken at 500X magnification.

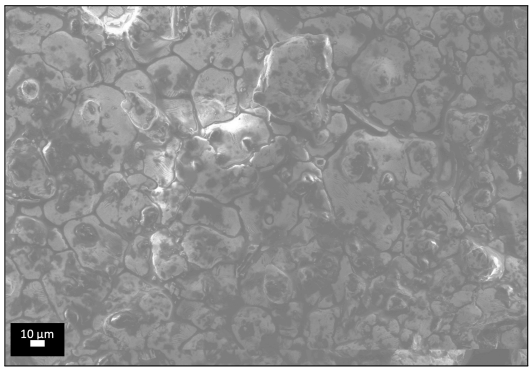

(b) Taken at 1000X magnification.

Figure 4.9: SEM images of pellet Pγ-3.

4.1.7 Density Measurements of Pellets

The density and porosity of the as-sintered BCZT pellets have been measured both using Archimedes' method and by using a caliper and weight. The dimensions and weight of the pellets are given in Table A.3 and Table A.4. In Table 4.3 the apparent (ρ_a), bulk (ρ_b) and relative density (ρ_{rel}) are given as well as the apparent (π_a), true (π_t) and closed porosity (π_c). The apparent porosity is often referred to as the open porosity while the true porosity is referred to as the total porosity. Pellet Pγ-2 and Pγ-3 have similar bulk densities while Pγ-1 has a slightly lower bulk density. The majority of the porosity in pellet Pγ-2 and Pγ-3 is open, with almost no closed porosity. Meanwhile, for Pγ-1 the closed porosity is more than half the porosity in the pellet.

Table 4.3: The theoretical and bulk density of the BCZT pellets, as well as their apparent, true and closed porosity.

ID	ρ_a [**g/cm**^{3}]	ρ_b [**g/cm**^{3}]	ρ_{rel} [**%**]	π_a [**vol%**]	π_t [**vol%**]	π_c [**vol%**]
Pγ-1	4.644	4.497	80.74	7.968	19.260	11.293
Pγ-2	4.541	5.009	89.92	10.69	10.69	0
Pγ-3	4.638	5.000	89.77	9.974	10.232	0.258

4.2 BCZT/Porcelain Coatings

Seven sets of BCZT/porcelain coatings have been made based on the β- and γ-BCZT powders. There is one baseline set with only bonder and dentin porcelain, then three sets with β-BCZT and three sets with γ-BCZT mixed with the dentin porcelain. For the sets with BCZT powder the dentin porcelain has been mixed with the BCZT powder into the following compositions; 30/70 wt% BCZT/dentin, 40/60 wt% BCZT/dentin, and 50/50 wt% BCZT/dentin.

4.2.1 Bond Strength

The bond strength of the coatings was measured in a De-bonding/crack initation test, done according to ISO 9693:2019. The *testXpert III* software measures the force as a function of the deflection. The resulting deflection curves are given in Appendix F. The sample ID, fracture force (F_{fail}) and bond strength (τ_b) of each tested sample are given in Table 4.4. In Figure 4.10, the bond strengths of each set of samples are shown as a boxplot. The weight percentage of BCZT is given along the x-axis while the bond strength is given along the y-axis. In the figure, the results for coatings made with β-BCZT are plotted to the left while they are plotted to the right for the coatings made with γ-BCZT. A horizontal line has been added at 25 MPa to mark the bond strength criteria in ISO 9693:2019 for metal-ceramic systems.

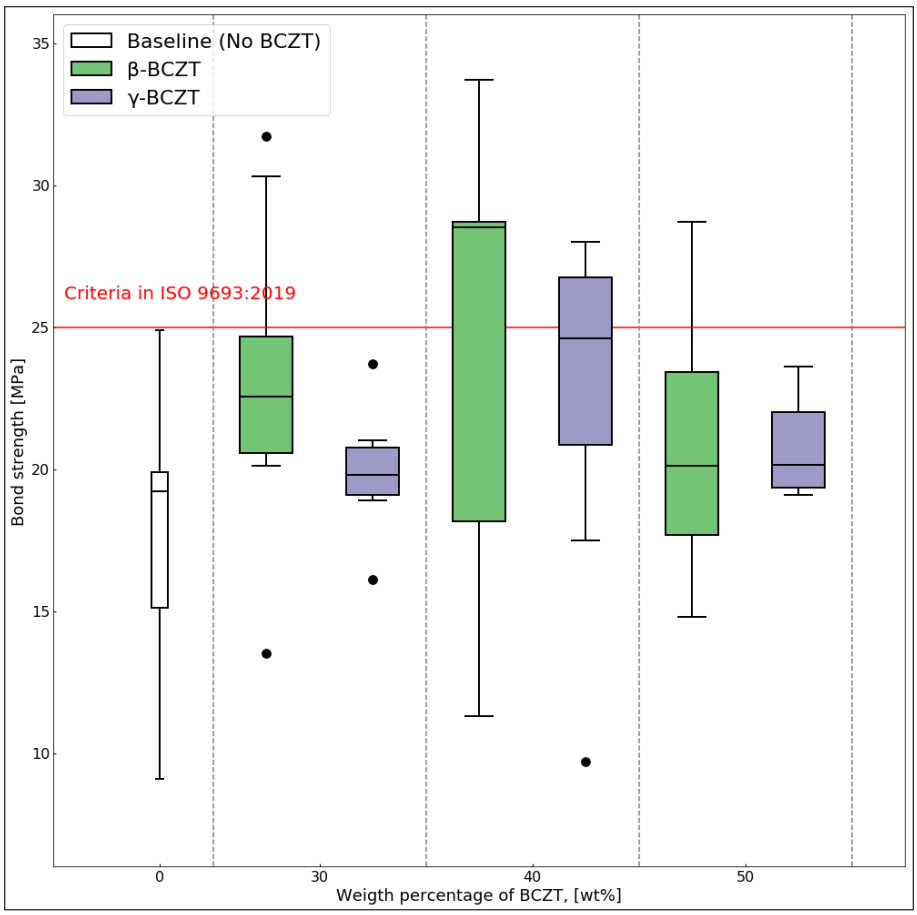

Figure 4.10: Boxplot showing the distribution of bond strength for each set of samples.

There are four elements in the boxplot; the median line, the "box" which is made up of the first and third quartile, the whiskers, and lastly the outliers. The median line is found within the "box", this represents the median value in the data set. The first and third quartile make up the limits of the "box". These are determined by the median value between the median value and the lowest or highest value of the data set, respectively. The whiskers have here been set to include all values between 5% and 95% of the data set. The outliers are present as dots either above or below the whiskers. These represent the values in the data set that falls outside the whiskers. The bond strength data has been plotted in a boxplot to better display the variation within each set of samples.

From Figure 4.10 and Table 4.4 one can see that the Dβ-40 set has the highest bond strength, but also the largest variation in measured values. The coatings made with β-BCZT have a higher median bond strength for both 30wt% and 40 wt% BCZT, while the median is nearly identical for the 50wt% BCZT compositions. However, the maximum values for the coatings made with β-BCZT powder are higher for all compositions compared to the same composition with γ-BCZT powder. The baseline coatings have a maximum bond strength just below 25 MPa. The median value for this set of samples is also lower than for all other sets.

Table 4.4: Fracture force and bond strength of each tested sample, together with any notes written down during the testing.

Sample ID	**F_{fail} [N]**	**τ_b [MPa]**	**Note**
D-00-1	5.16	25.6	
D-00-2	3.53	17.3	
D-00-3	4.16	19.9	
D-00-4	4.38	19.8	
D-00-5	1.91	9.18	
D-00-6	3.19	15.4	
D-00-15	5.05	24.2	
D-00-16	3.05	14.6	Fell off completely after test
D-00-18	3.8	19.4	
Dγ-30-1	5.11	24.0	
Dγ-30-2	3.89	19.5	
Dγ-30-4	3.41	16.3	
Dγ-30-5	4.45	21.2	
Dγ-30-6	4.26	20.0	
Dγ-30-9	4.27	20.0	
Dγ-30-16	-	-	Broke before force was measurable
Dγ-40-1	5.14	24.5	
Dγ-40-2	5.11	24.7	
Dγ-40-3	1.88	9.81	Unusual deflection curve
Dγ-40-4	5.54	26.1	
Dγ-40-5	5.83	28.1	
Dγ-40-6	5.64	27.4	
Dγ-40-11	3.80	17.7	Small cracking sounds immediately
Dγ-50-1	4.44	21.0	
Dγ-50-2	5.14	23.7	
Dγ-50-3	3.92	19.1	
Dγ-50-4	4.05	19.5	
Dγ-50-5	4.61	22.7	
Dγ-50-9	4.04	19.3	
Dβ-30-1	6.10	31.2	
Dβ-30-2	2.73	13.7	Broke almost immediately
Dβ-30-3	4.61	22.9	
Dβ-30-4	4.14	20.2	
Dβ-30-5	6.56	30.3	
Dβ-30-6	4.67	21.6	Fell off completely after test
Dβ-30-14	4.69	22.6	
Dβ-30-17	4.49	21.2	
Dβ-40-1	6.25	28.6	

Continued on next page

Table 4.4 *continued from previous page*

Sample ID	**F_{fail} [N]**	**τ_b [MPa]**	**Note**
Dβ-40-2	2.93	14.1	Cracking sounds immediately
Dβ-40-3	5.95	29.1	
Dβ-40-4	6.87	33.7	
Dβ-40-5	4.52	22.0	
Dβ-40-6	2.27	11.3	Broke immediately
Dβ-40-12	5.74	28.5	
Dβ-50-1	5.83	29.4	Small cracking sounds before fracture
Dβ-50-2	3.04	15.1	
Dβ-50-3	3.62	17.5	
Dβ-50-4	4.16	19.6	
Dβ-50-5	5.14	24.6	
Dβ-50-6	4.59	21.0	

4.2.2 Energy Dispersive Spectroscopy of BCZT/Porcelain Coatings

An EDS analysis was performed on the cross section of sample D-00-8, Dγ-30-11, and Dβ-30-7. The analyses were done on multiple points on each cross section as well as a mapping analysis of one section. The analysis was done to confirm the appearance of each phase of the coating, and to get a better understanding of the composition of the dental porcelains.

First multiple points in each cross section were analysed. The points were spread out throughout the different phases, i.e some points in what appeared to be the dentin-phase, some in the bonder-layer, some in what looked like BCZT particles, and some on the substrate. The elements found in each component of the coatings are listed in Table 4.5. An overview image of the scanned points in each sample, as well as tables with the amount of each element can be found in Appendix D.

Table 4.5: Elements found with EDS analysis of the different components of the coatings.

	Substrate			**Bonder**			**Dentin**			**BCZT**		
Element	D-00	Dγ	Dβ	D-00	Dγ	Dβ	D-00	dγ	Dβ	D-00	Dγ	Dβ
Al	x	x	x		x	x	x	x	x		x	
Ba	x						x	x	x		x	x
C		x	x									
Ca	x			x	x	x	x	x	x		x	x
F				x			x					
K	x			x			x	x	x		x	
La					x	x						
Mg	x			x			x					
N	x	x	x	x			x					
Na	x			x	x	x	x	x	x		x	
O				x	x	x	x	x	x		x	x
Si	x			x			x	x	x		x	
Sr					x	x						
Ti	x	x	x	x							x	x
V	x	x	x	x	x	x	x					
Zr							x				x	x

A selection of the elemental map scans for D-00-8, Dγ-30-11, and Dβ-30-7 are given in Figure 4.11, Figure 4.12 and Figure 4.13, respectively. These images show where the different elements can be found in each sample. For sample D-00-8 one can see that Si, K, Na and Ca are present in the same area and that this looks like the dentin-phase in the coating based on the SEM image in Figure 4.11a. Ti and Al are present in the substrate layer, and there seems to be areas where Al has gathered more densely. V can be seen in the substrate layer as well as in the bonder layer.

In sample Dγ-30-11 the elements Si, K, Na, and Ca can be seen in the same areas. However, Al is also present in the dentin-phase in this sample as well as in the substrate layer. The segregation of Al close to the surface of the substrate can be seen here also. Ba and Ti are present in both the substrate and in the BCZT particles. The same applies for V, but V is also present in the bonder layer. Zr is only found in one area, in what appears to be a larger BCZT-particle. The same observations generally hold for sample Dβ-30-7 as well. However, Zr is visible in more of the BCZT particles in this sample.

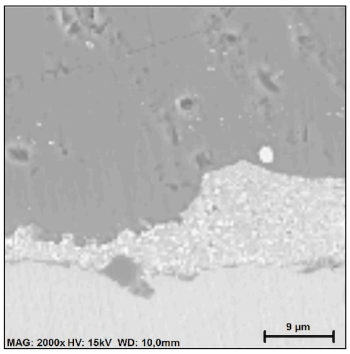

(a) Overview of area mapped with EDS in D-00-8.

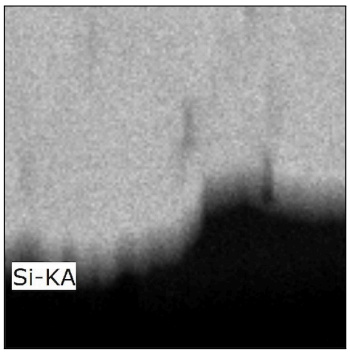

(b) Elemental map of D-00-8, showing Si.

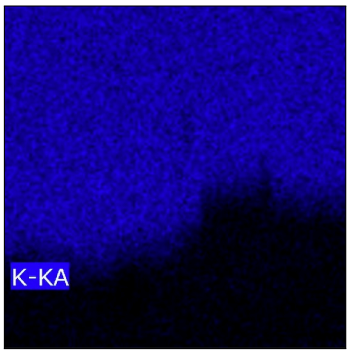

(c) Elemental map of D-00-8, showing K.

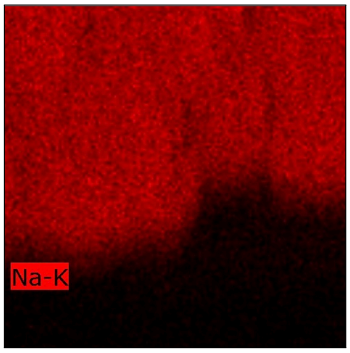

(d) Elemental map of D-00-8, showing Na.

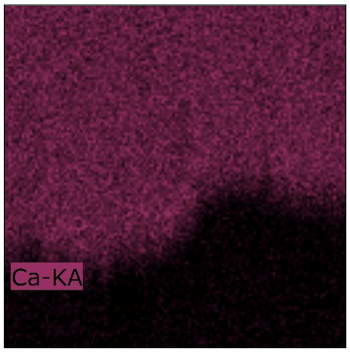

(e) Elemental map of D-00-8, showing Ca.

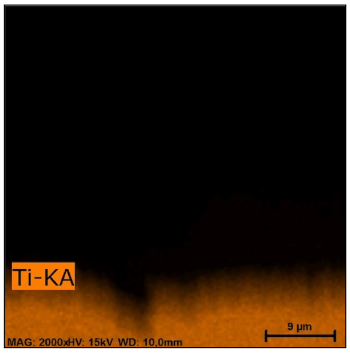

(f) Elemental map of D-00-8, showing Ti.

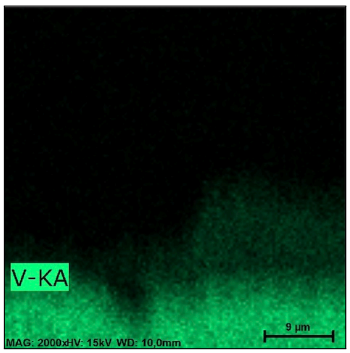

(g) Elemental map of D-00-8, showing V.

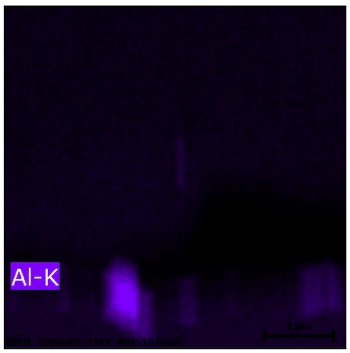

(h) Elemental map of D-00-8, showing Al.

Figure 4.11: Overview and elemental maps of D-00-8, from EDS analysis.

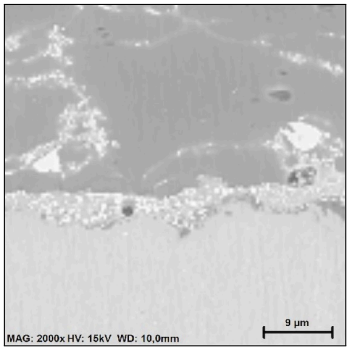

(a) Overview of area mapped with EDS in Dγ-30-11.

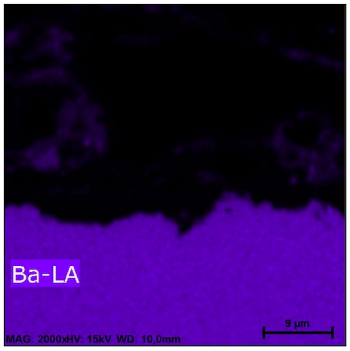

(b) Elemental map of Dγ-30-11, showing Ba.

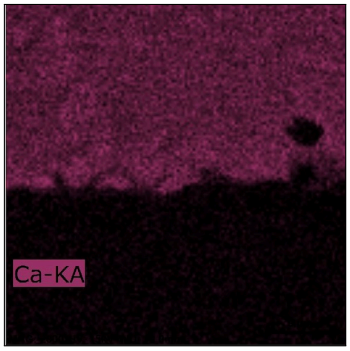

(c) Elemental map of Dγ-30-11, showing Ca.

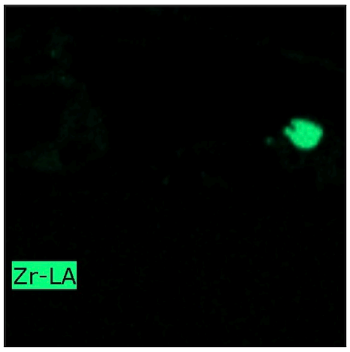

(d) Elemental map of Dγ-30-11, showing Zr.

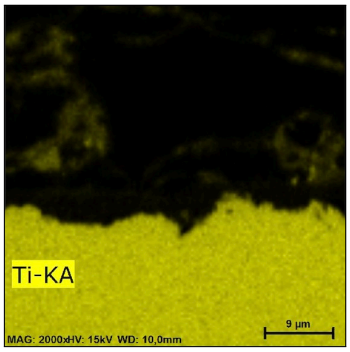

(e) Elemental map of Dγ-30-11, showing Ti.

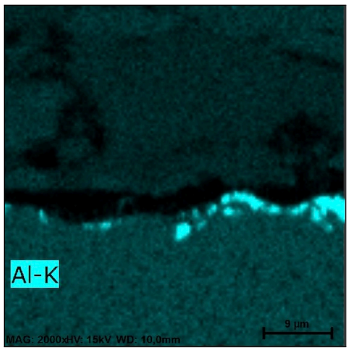

(f) Elemental map of Dγ-30-11, showing Al.

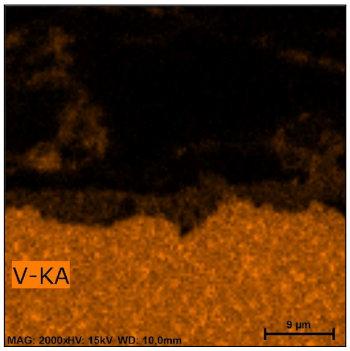

(g) Elemental map of Dγ-30-11, showing V.

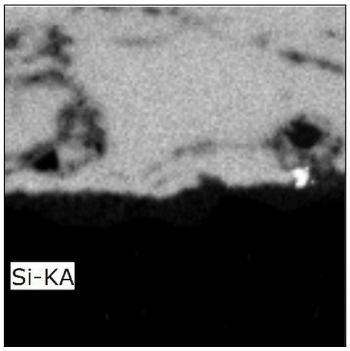

(h) Elemental map of Dγ-30-11, showing Si.

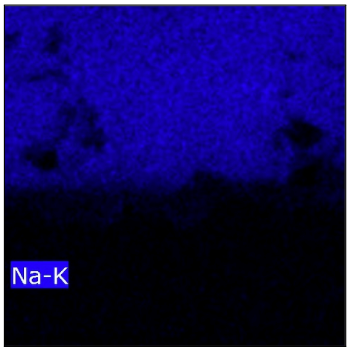

(i) Elemental map of Dγ-30-11, showing Na.

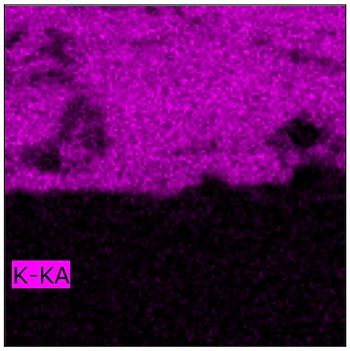

(j) Elemental map of Dγ-30-11, showing K.

Figure 4.12: Overview and elemental maps of Dγ-30-11, from EDS analysis.

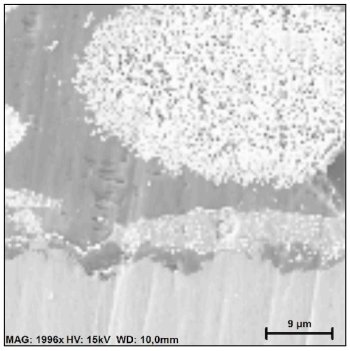

(a) Overview of area mapped with EDS in Dβ-30-7.

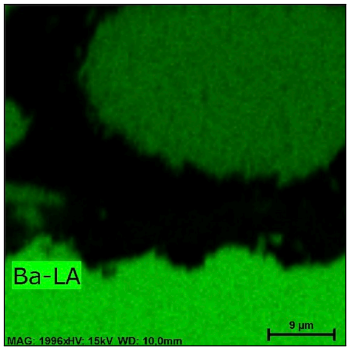

(b) Elemental map of Dβ-30-7, showing Ba.

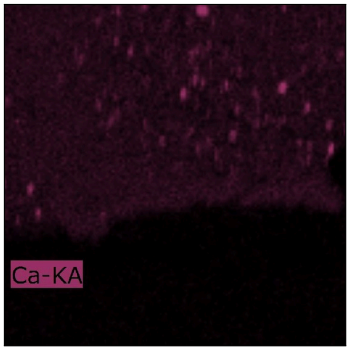

(c) Elemental map of Dβ-30-7, showing Ca.

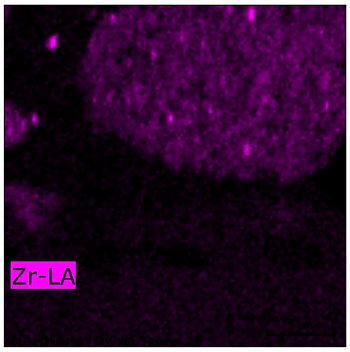

(d) Elemental map of Dβ-30-7, showing Zr.

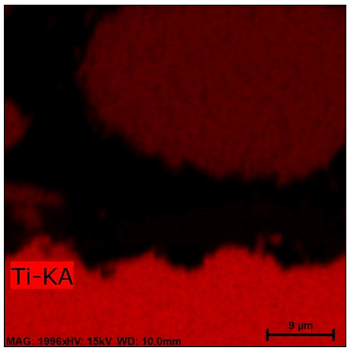

(e) Elemental map of Dβ-30-7, showing Ti.

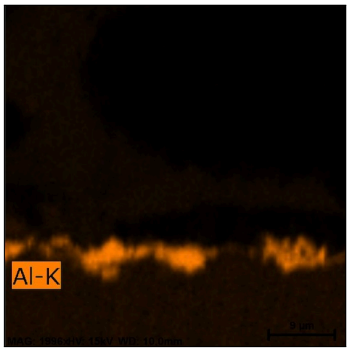

(f) Elemental map of Dβ-30-7, showing Al.

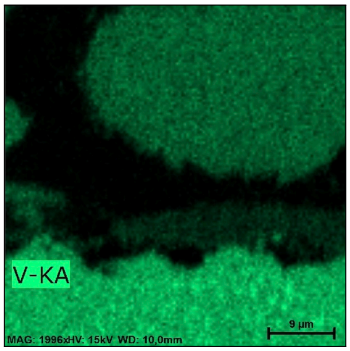

(g) Elemental map of Dβ-30-7, showing V.

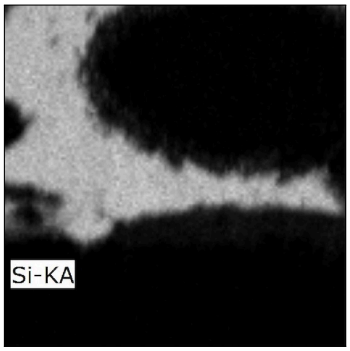

(h) Elemental map of Dβ-30-7, showing Si.

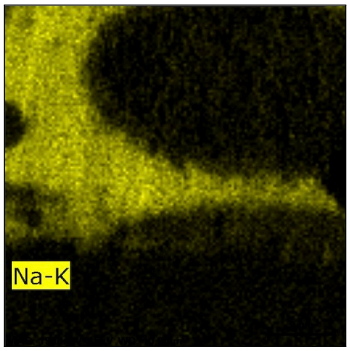

(i) Elemental map of Dβ-30-7, showing Na.

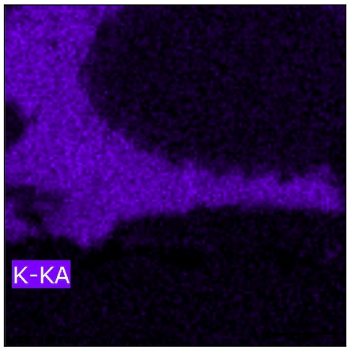

(j) Elemental map of Dβ-30-7, showing K.

Figure 4.13: Overview and elemental maps of Dβ-30-7, from EDS analysis.

4.2.3 X-Ray Diffraction Analysis

One coated sample of each composition was analysed using XRD, the resulting diffractograms are given in Figure 4.14. The PDF for BCZT (PDF 01-086-8334) and for Ti-6Al-4V (PDF 04-020-7055) are also given in the same plot. The diffractograms for the coatings with BCZT are very similar, both the Ti-6Al-4V and BCZT peaks can be seen. This is expected due to the thickness of the coating. The BCZT peaks are not present in the baseline sample. There is some noise and other peaks present in the diffractograms, this is most likely caused by the amorphous nature of the porcelain and by the different elements present in the porcelain.

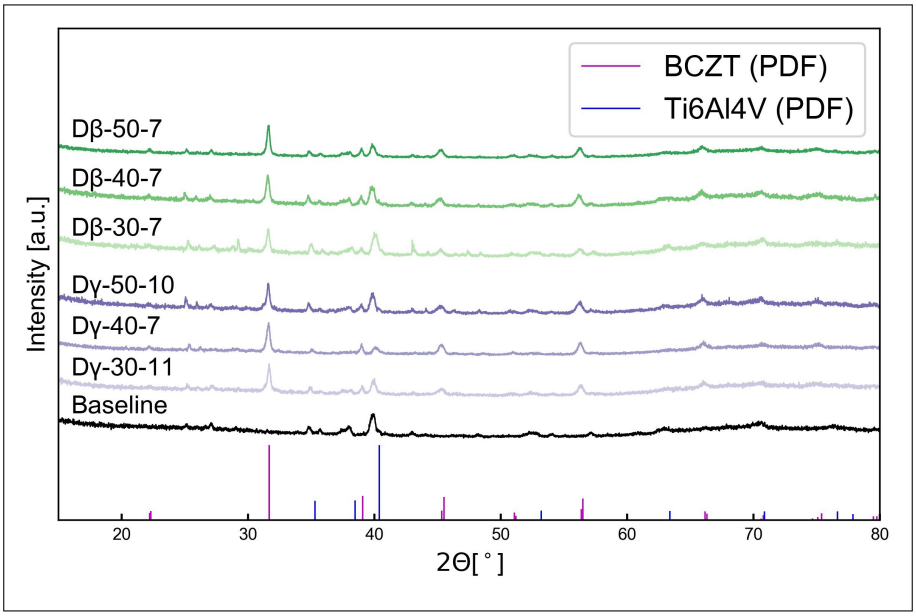

Figure 4.14: Diffractogram of each of the different coating compositions.

4.2.4 Scanning Electron Microscope Imaging of Surface and Cross Section

The surface and cross section of one sample from each set of coated samples were imaged with SEM. The images of D-00-8 and D-00-1 are given in Figure 4.15. The two porcelain layers are distinguishable in Figure 4.15b, and in Figure 4.15a some pores are visible within the smooth glass phase of the dentin porcelain. A few pores are visible on the surface in Figure 4.15c. There are some smaller particles distributed over the whole surface but the glass phase in the porcelain makes up the bulk of the surface. The glass phase looks like it has been able to flow into the crevices on the substrate surface. The particles in the bonder layer have stayed within the bonder-layer, and not spread into the BCZT/dentin layer. Any pores begin above the bonder layer, not within or underneath it.

SEM images of the cross section and surface of sample Dβ-30-7 and Dβ-30-4 are given in Figure 4.16. The BCZT particles are visible as lighter areas in the coating. The distribution of the larger BCZT particles in the porcelain are visible as well as the interface between the substrate, bonder and BCZT/Dentin layers. The particles

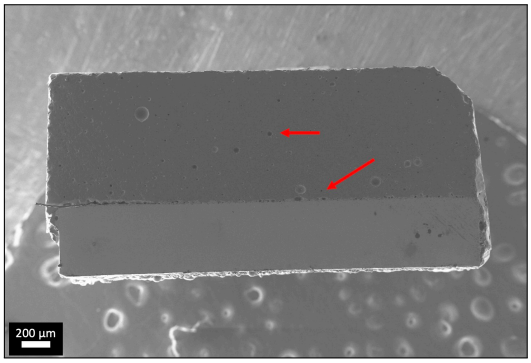

(a) SEM image of the cross section of D-00-8, taken at 100X magnification.

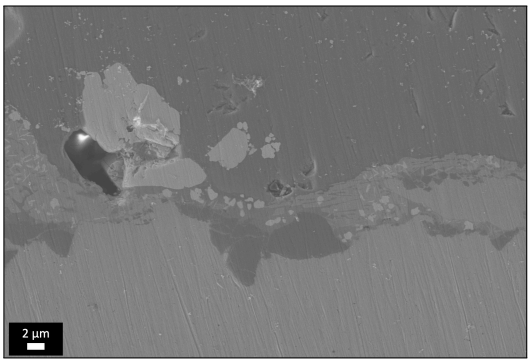

(b) SEM image of the cross section of D-00-8, taken at 6 500X magnification.

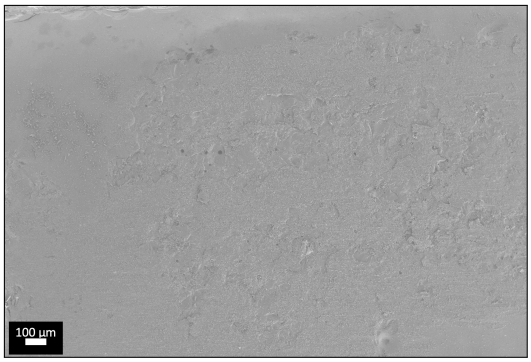

(c) SEM image of the surface of D-00-1, taken at 150X magnification.

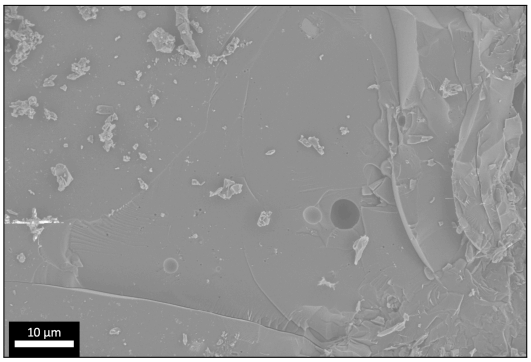

(d) SEM image of the surface of D-00-1, taken at 4 000X magnification.

Figure 4.15: SEM images of the cross section and surface of D-00-8 and D-00-1, respectively.

are not entirely homogeneously distributed throughout the coating. There are some pores visible in the cross-section and some on the surface of the coating. There also seem to be some marks from polishing visible on the surface. Looking closer at the interface between the layers, one can see that the glass phase in the porcelain has been able to flow and fill any crevices on the substrate and around the particles in the bonder-layer.

The SEM images of the cross section and surface of Dβ-40-7 and Dβ40-1 are given in Figure 4.17. These look similar to the images of Dβ-30-7 and Dβ-30-4. However, there is an increase in the amount of pores visible in the cross section. In this sample some pores are also present in the bonder-layer. Otherwise the interfaces between the layers are nice with no gaps. This suggest that the glass phase has been able to flow around any particles in this area during firing. There are some larger BCZT particles surrounded by pores in the bottom right corner of the coating. On the surface both the BCZT particles and the glass phase of the porcelain are visible.

The SEM images of Dβ-50-7 and Dβ-50-1 are given in Figure 4.18. The amount of pores visible in the cross section has increased from the previous samples, but the interface between the substrate, bonder and BCZT/dentin layer still looks the same. There are more visible pores close to the substrate, to the bottom left of the cross section. Additionally, it can seem like some of the larger BCZT particles have gathered in one area. Again, the BCZT particles and the glass phase are visible on

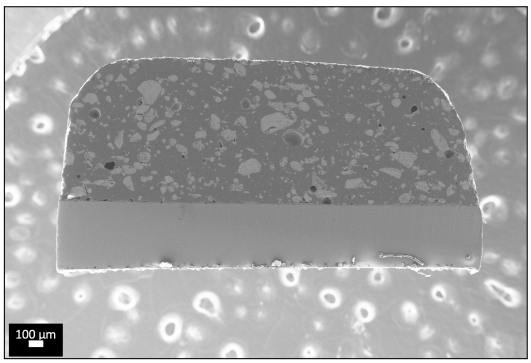

(a) SEM image of the cross section of Dβ-30-7, taken at 100X magnification.

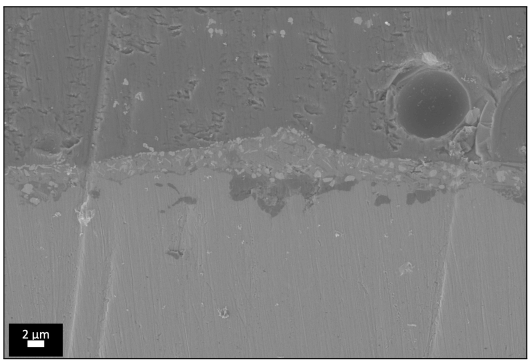

(b) SEM image of the cross section of Dβ-30-7, taken at 6 500X magnification.

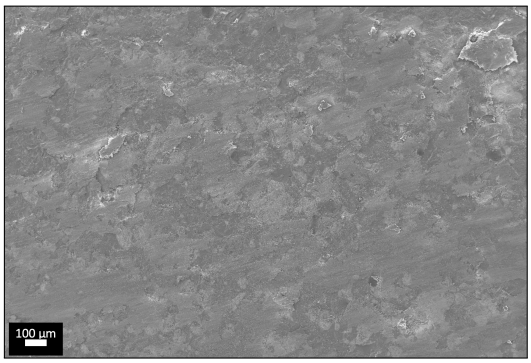

(c) SEM image of the surface of Dβ-30-4, taken at 150X magnification.

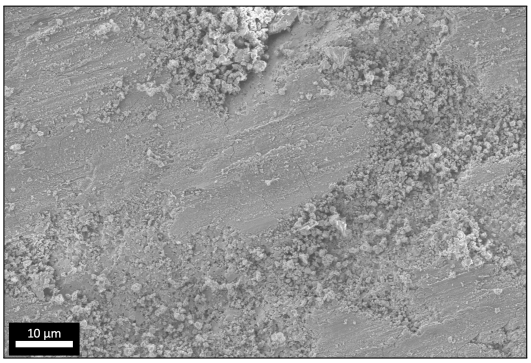

(d) SEM image of the surface of Dβ-30-4, taken at 4 000X magnification.

Figure 4.16: SEM images of the cross section and surface of Dβ-30-7 and Dβ-30-4, respectively.

the coating surface.

The SEM images of sample Dγ-30-11 and Dγ-30-1 are given in Figure 4.19. The BCZT particles are visible as lighter areas in the coating, some pores are also visible in the cross section. The SEM images of the surface show that there are pores there as well, and in Figure 4.19d what appears to be BCZT particles are visible in a pit on the surface. The particles are relatively evenly distributed, and some larger agglomerates are present. The interface and the bonder-layer looks the same as for the previous sample.

SEM images of Dγ-40-7 and Dγ-40-2 are given in Figure 4.20. These generally look similar to those in Figure 4.19, but with more pores and more BCZT. Images of Dγ-50-10 and Dγ-50-1 are given in Figure 4.21. In the cross section of Dγ-50-10 there are more pores than in previously mentioned samples, these are larger and more elongated. On the surface, larger areas of BCZT particles are visible. The interface between the layers looks the same even though the amount of BCZT powder has increased.

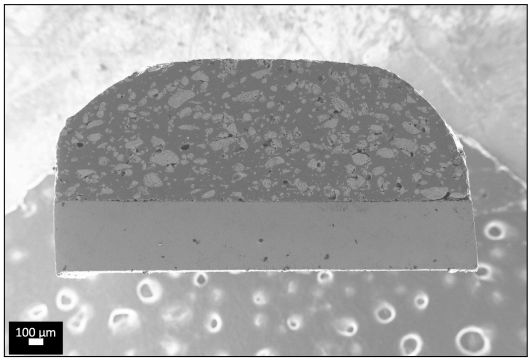

(a) SEM image of the cross section of Dβ-40-7, taken at 100X magnification.

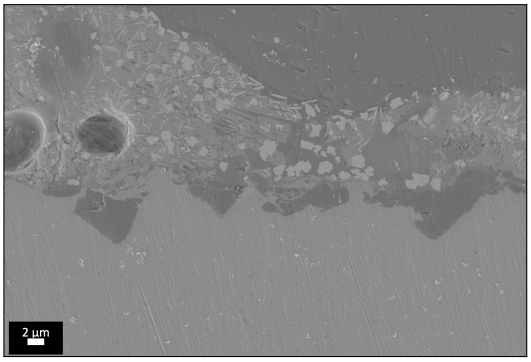

(b) SEM image of the cross section of Dβ-40-7, taken at 6 500X magnification.

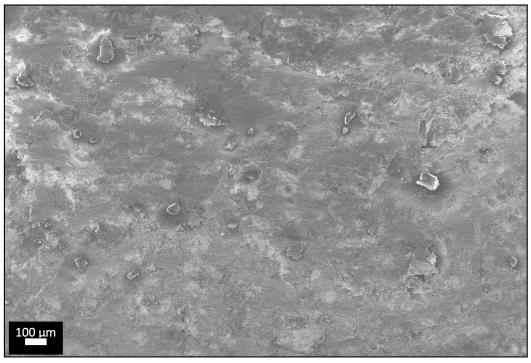

(c) SEM image of the surface of Dβ-40-1, taken at 150X magnification.

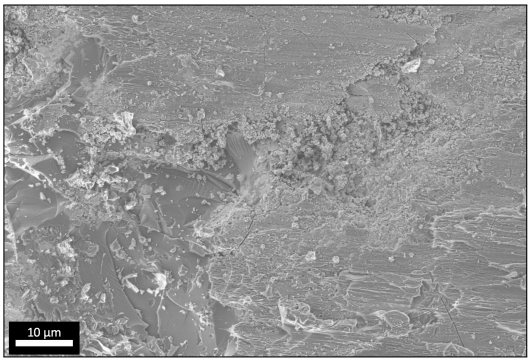

(d) SEM image of the surface of Dβ-40-1, taken at 4 000X magnification.

Figure 4.17: SEM images of the cross section and surface of Dβ-40-7 and Dβ-40-1, respectively.

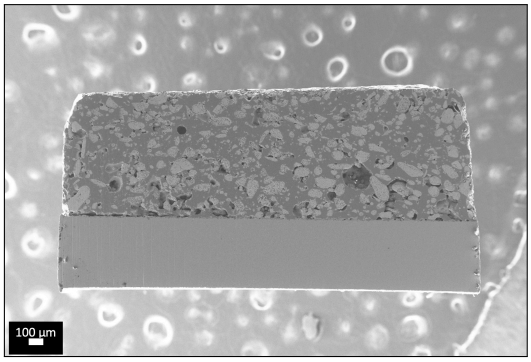

(a) SEM image of the cross section of Dβ-50-7, taken at 100X magnification.

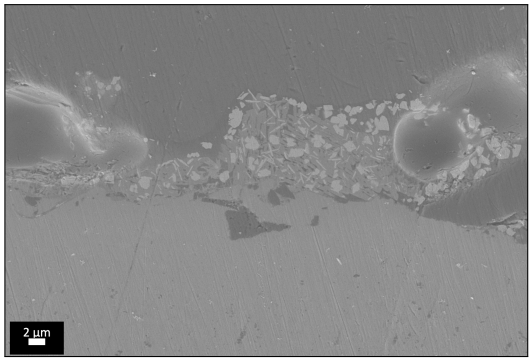

(b) SEM image of the cross section of Dβ-50-7, taken at 6 500X magnification.

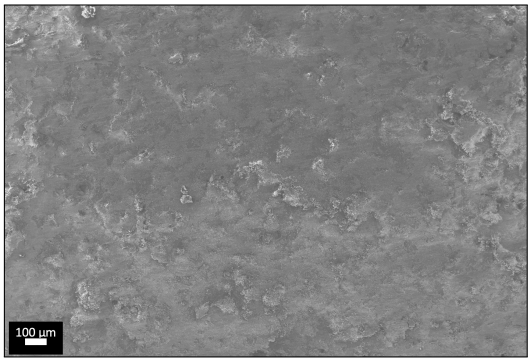

(c) SEM image of the surface of Dβ-50-1, taken at 150X magnification.

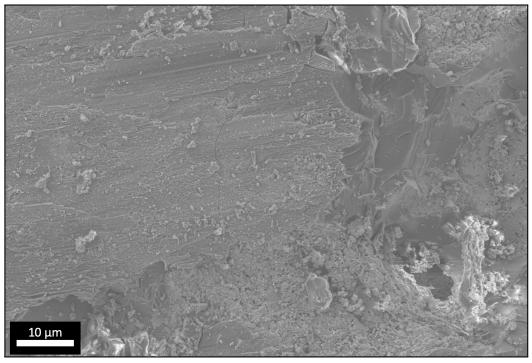

(d) SEM image of the surface of Dβ-50-1, taken at 4 000X magnification.

Figure 4.18: SEM images of the cross section and surface of Dβ-50-7 and Dβ-50-1, respectively.

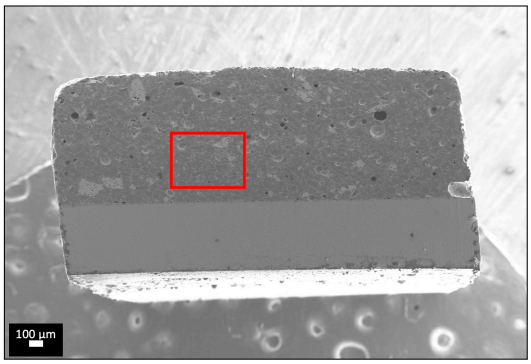

(a) SEM image of the cross section of Dγ-30-11, taken at 100X magnification.

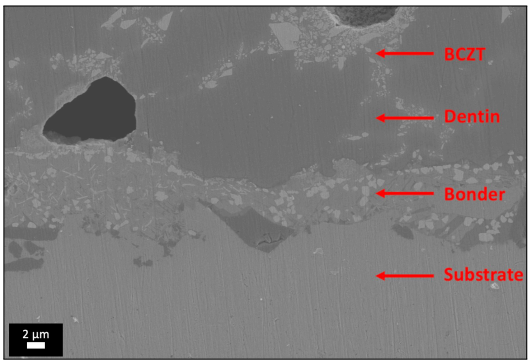

(b) SEM image of the cross section of Dγ-30-11, taken at 6 500X magnification.

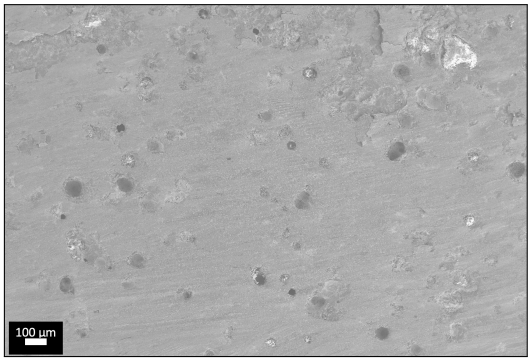

(c) SEM image of the surface of Dγ-30-1, taken at 150X magnification.

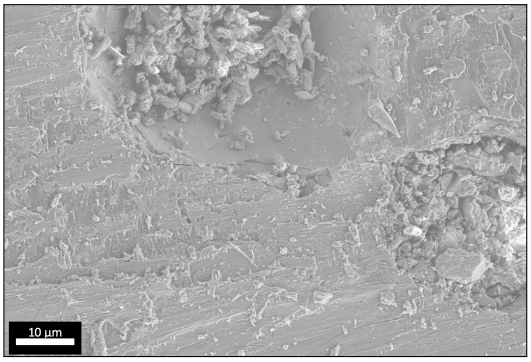

(d) SEM image of the surface of Dγ-30-1, taken at 4 000X magnification.

Figure 4.19: SEM images of the cross section and surface of Dγ-30-11 and Dγ-30-1, respectively.

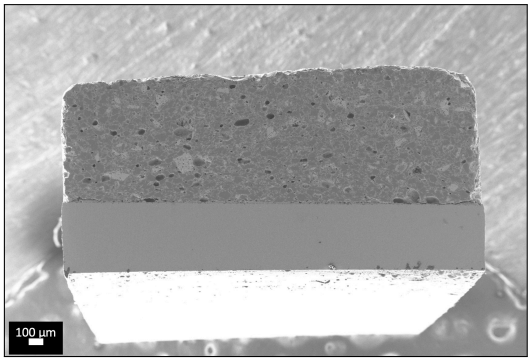

(a) SEM image of the cross section of Dγ-40-7, taken at 100X magnification.

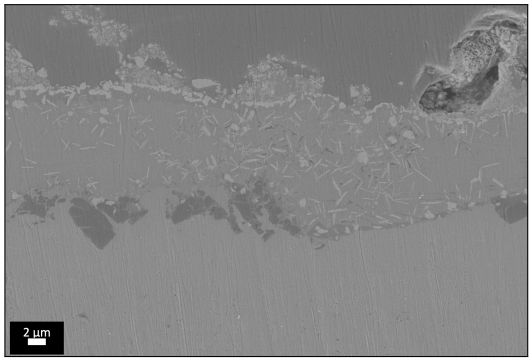

(b) SEM image of the cross section of Dγ-40-7, taken at 6 500X magnification.

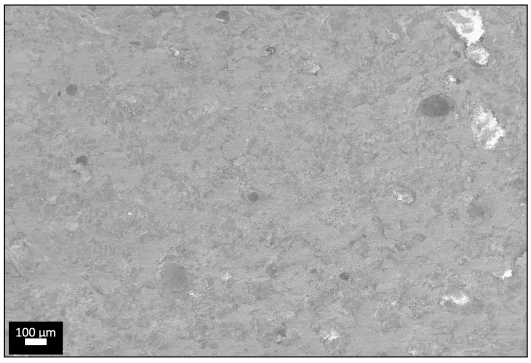

(c) SEM image of the surface of Dγ-40-2, taken at 150X magnification.

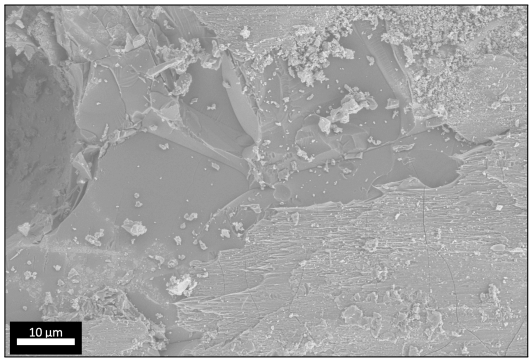

(d) SEM image of the surface of Dγ-40-2, taken at 4 000X magnification.

Figure 4.20: SEM images of the cross section and surface of Dγ-40-7 and Dγ-40-2, respectively.

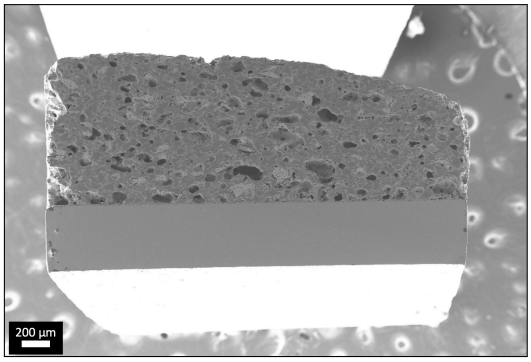

(a) SEM image of the cross section of Dγ-50-10, taken at 100X magnification.

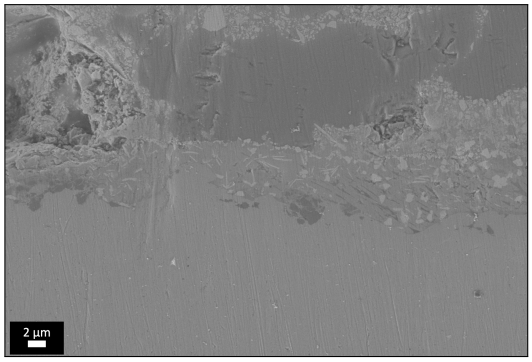

(b) SEM image of the cross section of Dγ-50-10, taken at 6 500X magnification.

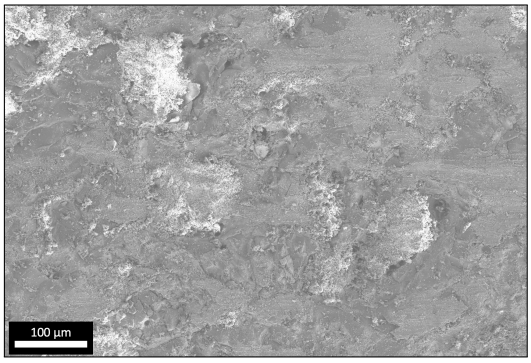

(c) SEM image of the surface of Dγ-50-1, taken at 150X magnification.

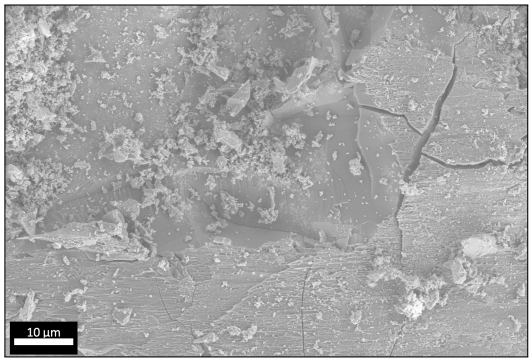

(d) SEM image of the surface of Dγ-50-1, taken at 4 000X magnification.

Figure 4.21: SEM images of the cross section and surface of Dγ-50-10 and Dγ-50-1, respectively.

4.2.5 Scanning Electron Microscope Imaging of Fractured Samples

One of the fractured samples in each set were imaged using SEM to get a better understanding of the fractures occurring in the Schwickerath adhesion test. Upon comparing the SEM images it was found that all the samples fractured very similarly. The fractures extends from one end of the coating to various lengths into the coatings. It also looks like the coatings have lifted from the substrate. Due to the similar fracture behaviour one set of images are shown in Figure 4.22, while more images can be found in Appendix C. The SEM images in Figure 4.22 show the side of sample Dβ-30-4.

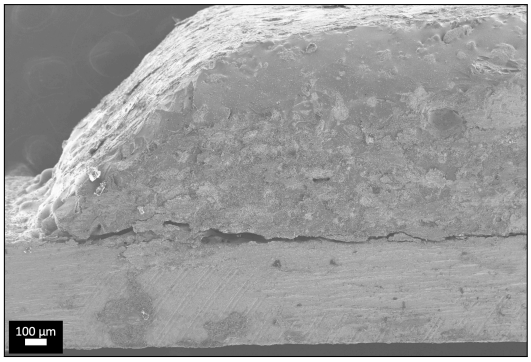

(a) SEM image of the side of Dβ-30-4 showing its fracture, taken at 150X magnification.

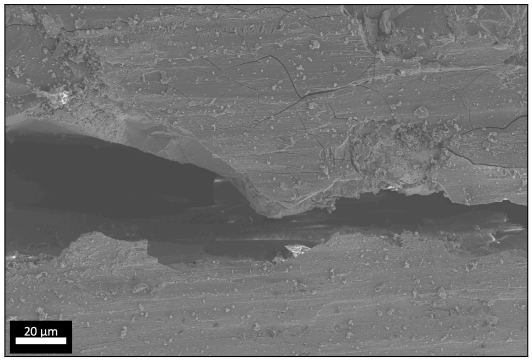

(b) SEM image of the side of Dβ-50-7 showing its fracture, taken at 1 750X magnification.

Figure 4.22: SEM images of the side profile of Dβ-30-4, showing the fracture resulting from the Schwickerath adhesion test.

In order to further understand the fracture behaviour of these coatings SEM images have been taken of the end of the metal substrate and where the coating has been fastened on the substrate, as well as of the underside of the coating. This has been done for sample Dγ-50-6, where the coating has broken completely off from the substrate. The images are given in Figure 4.23.

BCZT particles are visible on the underside of the coating in Figure 4.23a, which means that they made up part of the interface between the broken off coating and the substrate. Here some pores or gaps are also visible, suggesting that there either were pores prior to fracture or that parts of the coating is still adhered to the substrate. There is a difference between the images of the metal substrate and the substrate where the coating previously was. In Figure 4.23d the glass phase from the porcelain can be seen, this is not the case for the metal substrate in Figure 4.23f. These images show that while the coating delaminates in one end, parts of the coating is still left on the substrate.

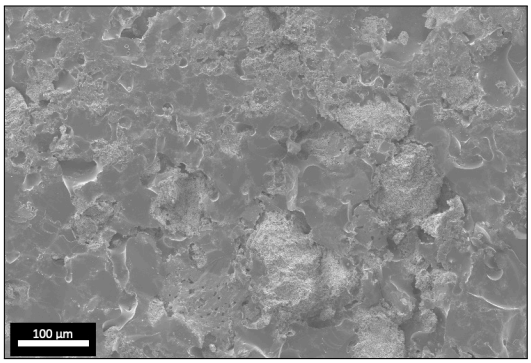

(a) SEM image of the underside of the coating on sample Dγ-50-6, taken at 500X magnification.

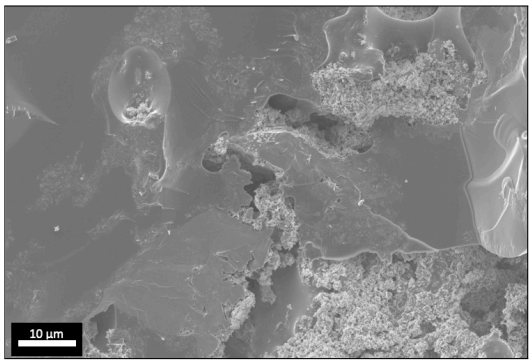

(b) SEM image of the underside of the coating on sample Dγ-50-6, taken at 4000X magnification.

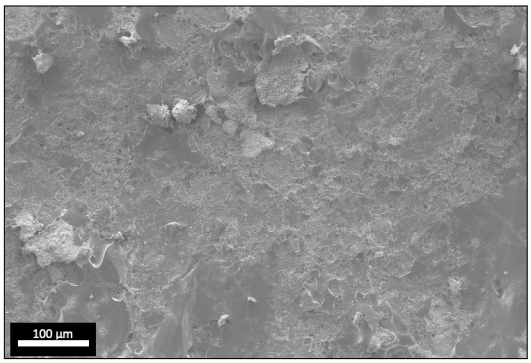

(c) SEM image of the substrate where the coating on sample Dγ-50-6 was, taken at 500X magnification.

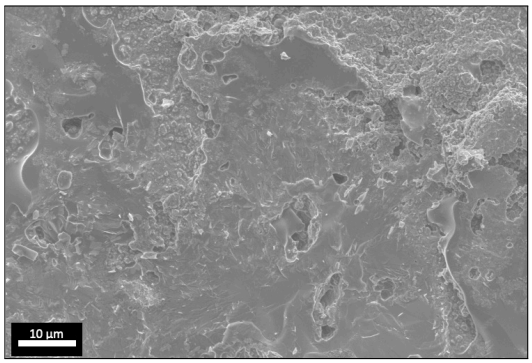

(d) SEM image of the substrate where the coating on sample Dγ-50-6 was, taken at 4000X magnification.

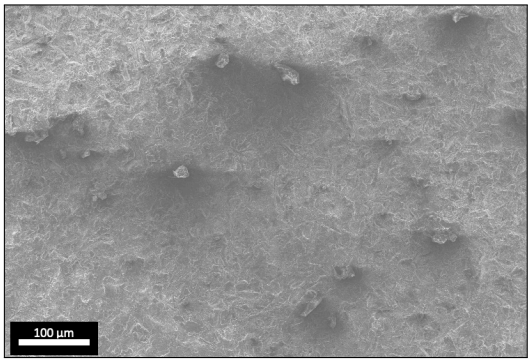

(e) SEM image of the substrate of sample Dγ-50-6, taken at 500X magnification.

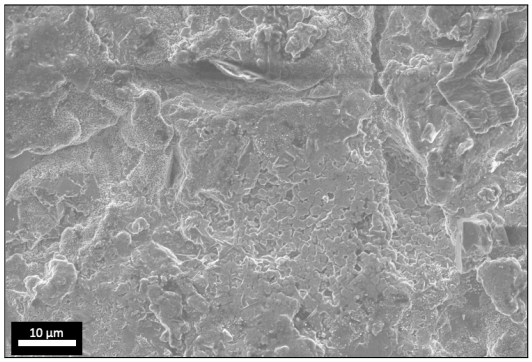

(f) SEM image of the substrate of sample Dγ-50-6, taken at 500X magnification.

Figure 4.23: SEM images of the underside of the coating, the substrate with coating residue, and the metal substrate of sample Dγ-50-6.

4.3 Piezoelectric Properties of BCZT Pellets and Coatings

The strain, polarisation, permittivity and piezoelectric coefficient (d_{33}) of the pellets and the coatings have been measured. The polarisation-electric field and strain-electric field hysteresis loops of the three pellets are given in Figure 4.24. Pellet Pγ-1 shows slightly different behaviour from the other two pellets, with a higher saturation polarisation and a higher remnant polarisation. This is accompanied by a higher degree of maximum strain. Pγ-2 and Pγ-3 show identical polarisation, but Pγ-3 shows a slightly higher strain.

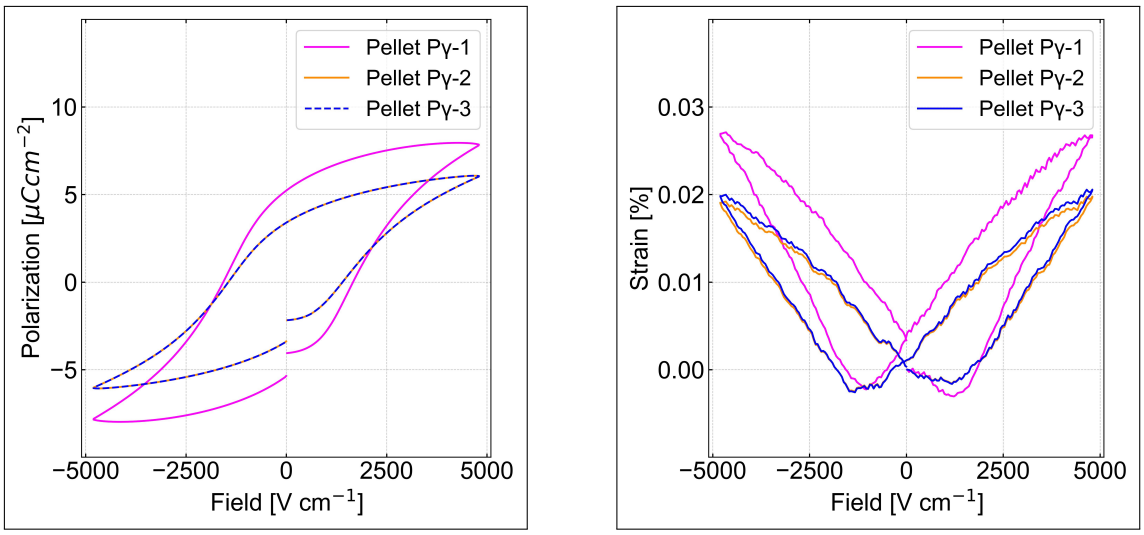

Figure 4.24: The (a) polarisation- and (b) strain-electric field loops for the three BCZT pellets.

The same plots are given for the coatings with γ-BCZT in Figure 4.26, and in Figure 4.27 for the coatings with β-BCZT. The polarisation- and strain-electric field loops for the baseline are given in Figure 4.25. The polarisation loops of the baseline coatings show no hysteresis character, they are instead thin and almost linear. The coatings with 30 wt% BCZT display very similar polarisation loops. The strain loops for these coatings and for the baseline coatings are more different.

As the amount of γ-BCZT powder is increased in the coatings, the polarisation loop adapts more of a hysteresis character. In the coatings with β-BCZT the polarisation loop is wider, however when the amount of BCZT is increased to 50 wt% the loops revert back to a more narrow shape. None of the strain loops for the coatings have the characteristic butterfly shape, which is present for the pellets.

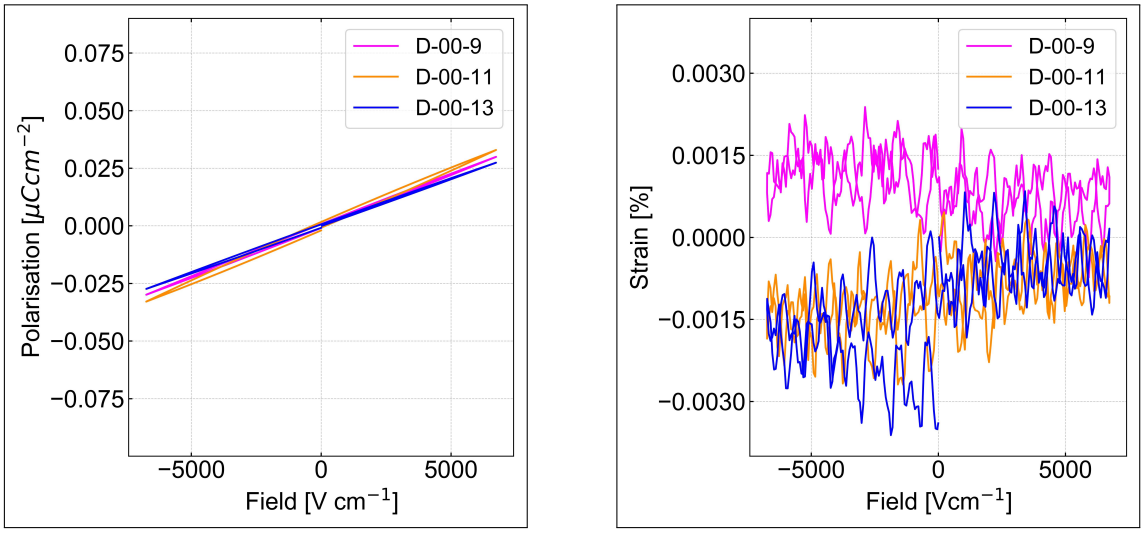

Figure 4.25: (a) Polarisation- and (b) strain-electric field loops for the baseline coatings, i.e. the coatings with no BCZT.

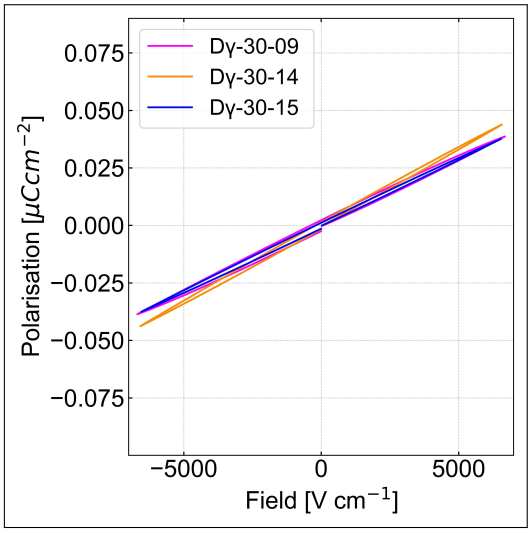

(a) Polarization-electric field hysteresis loop of coatings containing30 wt% γ-BCZT.

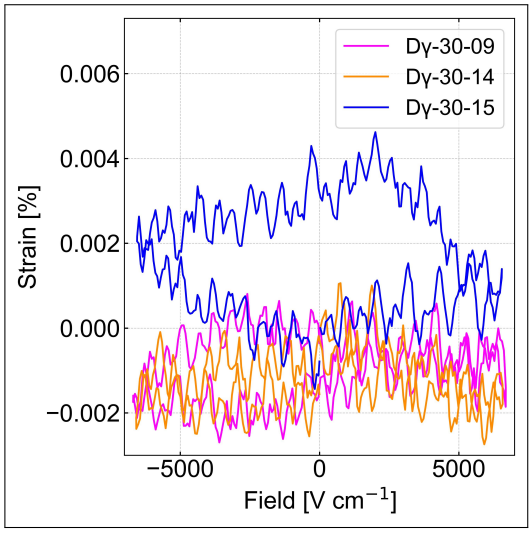

(b) Strain-electric field hysteresis loop of coatings containing30 wt% γ-BCZT.

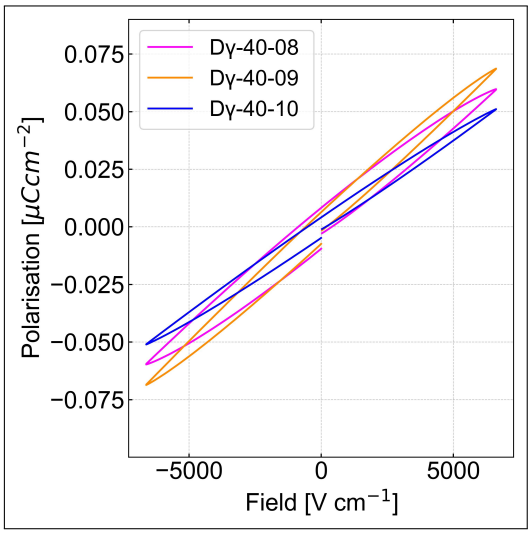

(c) Polarization-electric field hysteresis loop of coatings containing 40 wt% γ-BCZT.

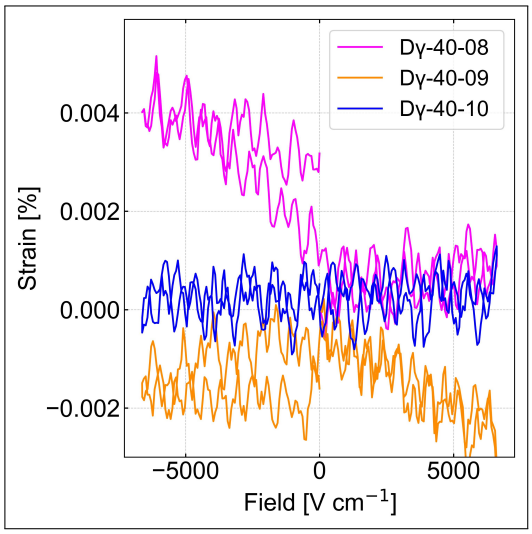

(d) Strain-electric field hysteresis loop of coatings containing 40 wt% γ-BCZT.

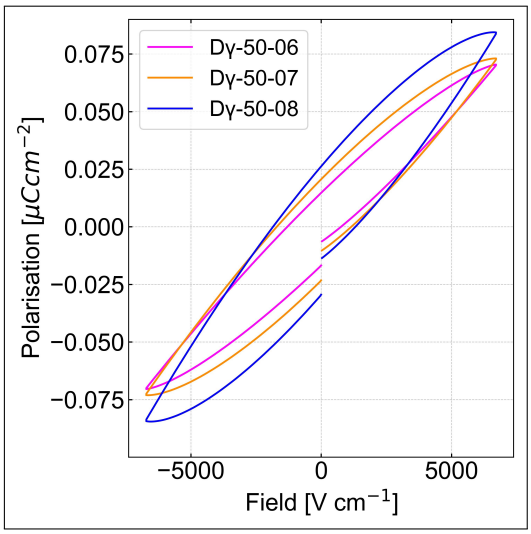

(e) Polarization-electric field hysteresis loop of coatings containing 50 wt% γ-BCZT.

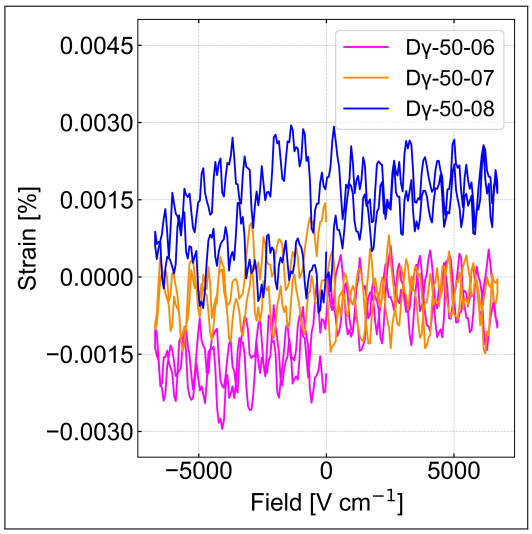

(f) Strain-electric field hysteresis loop of coatings containing 50 wt% γ-BCZT.

Figure 4.26: Polarization- and strain-electric field loops for coatings with γ-BCZT.

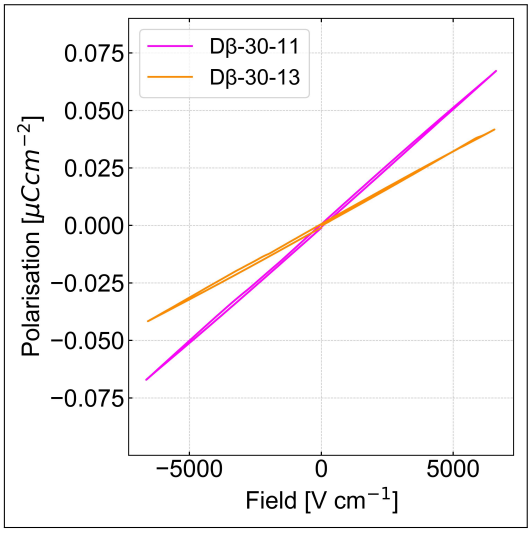

(a) Polarization-electric field hysteresis loop of coatings containing 30 wt% β-BCZT.

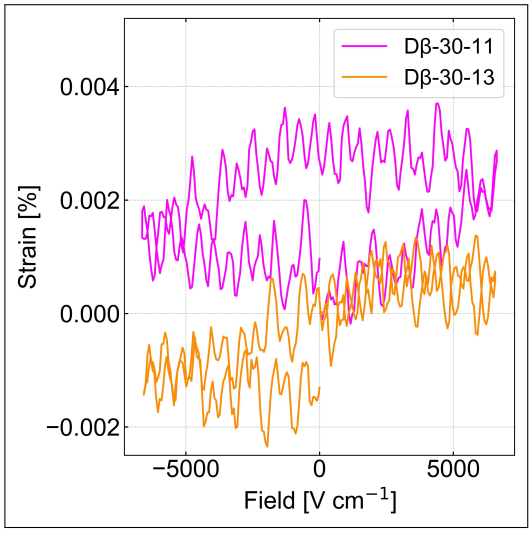

(b) Strain-electric field hysteresis loop of coatings containing 30 wt% β-BCZT.

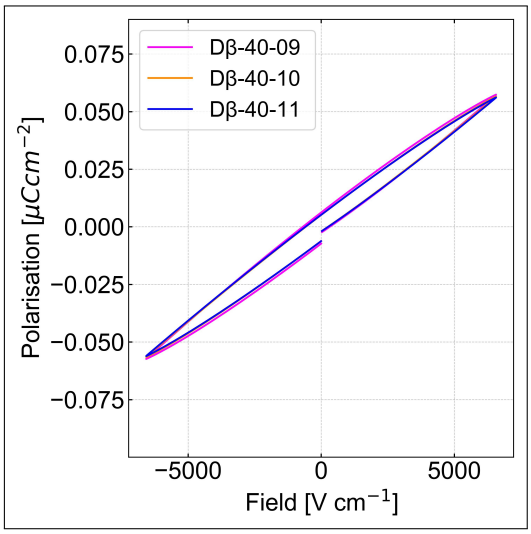

(c) Polarization-electric field hysteresis loop of coatings containing 40 wt% β-BCZT.

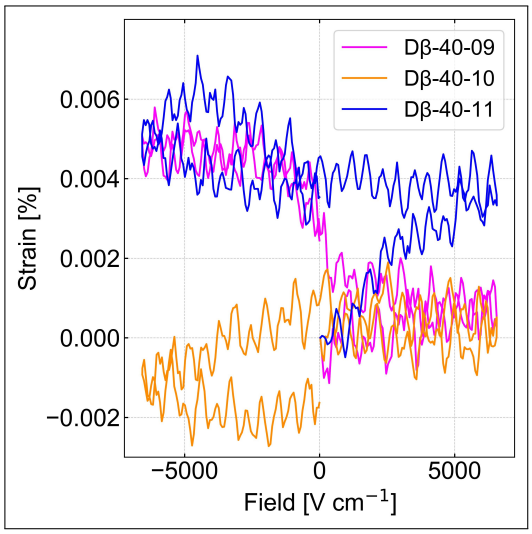

(d) Strain-electric field hysteresis loop of coatings containing 40 wt% β-BCZT.

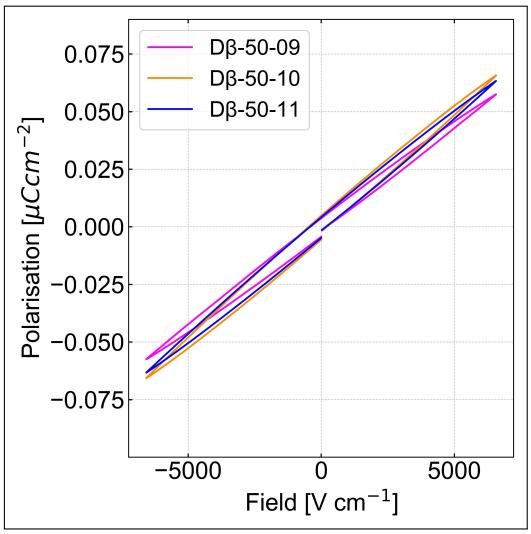

(e) Polarization-electric field hysteresis loop of coatings containing 50 wt% β-BCZT.

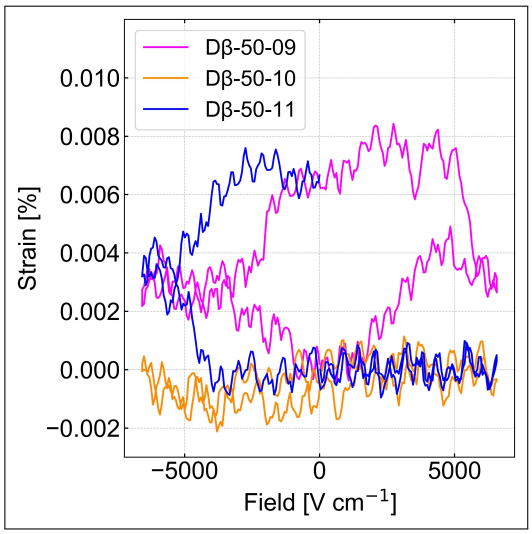

(f) Strain-electric field hysteresis loop of coatings containing 50 wt% β-BCZT.

Figure 4.27: Polarization- and strain-electric field loops for coatings with β-BCZT.

The piezoelectric coefficient d_{33} of the coatings was measured both for the direct and converse piezoelectric effect, but only for the direct piezoelectric effect for the pellets. The results of these measurements are given in Table 4.6. A plot of the converse d_{33} of the coatings is given in Figure 4.28. For the pellets, a piezoelectric coefficient between 90 and 142 pC/N was observed. Using the same measurement method on the coatings resulted in d_{33} values around 0.8 - 1 pC/N, with no significant differences between the different compositions. Measuring d_{33} via the converse piezoelectric effect resulted in more varied values, however there is also more variation within each composition and no clear trend between the compositions.

Table 4.6: d_{33} measured for the converse piezoelectric effect and for the direct effect.

Sample ID	$\mathbf{d_{33,converse}}$ **[nm/V]**	$\mathbf{d_{33,direct}}$ **[pC/N]**
Pγ-1	-	142.4
Pγ-2	-	106
Pγ-3	-	92.8
D-00-9	0.13	0.9
D-0011	-0.48	0.8
D-00-13	-0.26	0.84
Dγ-30-9	-0.03	0.92
Dγ-30-14	-0.39	0.9
Dγ-30-15	0.60	0.9
Dγ-40-8	0.18	0.92
Dγ-40-9	-0.26	0.9
Dγ-40-10	-0.30	0.84
Dγ-50-6	-0.25	0.9
Dγ-50-7	-0.32	0.96
Dγ-50-8	-0.07	0.86
Dβ-30-11	-0.13	0.96
Dβ-30-13	-0.19	0.88
Dβ-40-9	-0.20	0.86
Dβ-40-10	0.71	0.9
Dβ-40-11	0.05	0.94
Dβ-50-9	-0.11	0.94
Dβ-50-10	-0.10	0.88
Dβ-50-11	-0.27	0.88

The relative permittivity ϵ_r of the pellets and the coatings was measured in the AIX PES set-up. The permittivities when no electric field was applied are given in Table 4.7. The ϵ_r of the coatings have also been plotted in Figure 4.29 to give a visual representation of the variation within each set of coatings. The lowest and highest value for each set of coatings are represented by the boxes in the plot. The pellets have a ϵ_r around 2200 - 2300 while the baseline coatings have $\epsilon_r \approx 5$. The ϵ_r of the coatings with BCZT varies between 60 to 120. The coatings with 30 and 50 wt% β-BCZT have higher permittivities than the same coatings with γ-BCZT. The highest ϵ_r value of the Dγ-40 - coatings is higher than the ϵ_r value for the Dβ-40 - coatings.

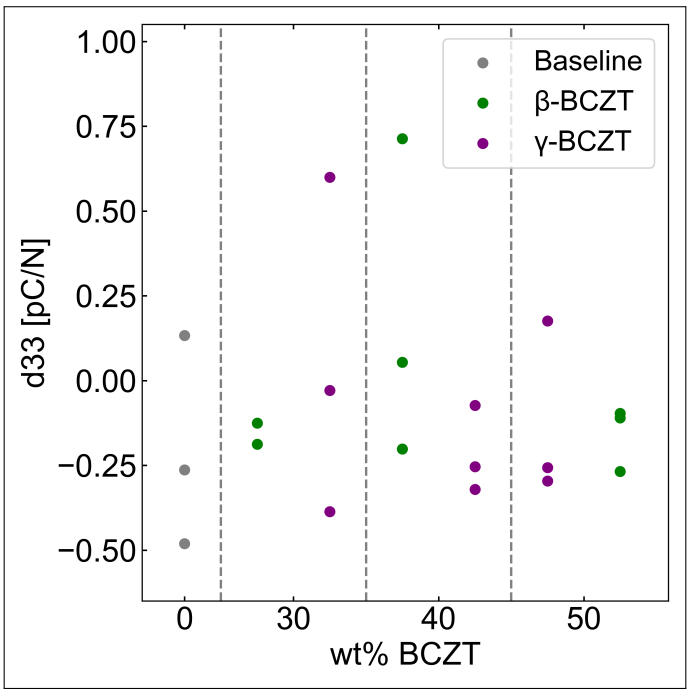

Figure 4.28: Plot of the average value for d_{33} for each coating sample. The coefficient was measured with the AIX PES, i.e. for the converse piezoelectric effect.

The change in ϵ_r and d_{33} for the pellets when an electric field is applied was also measured in the same set-up. The results are given in Figure 4.30. The d_{33}-electric field loop of pellet Pγ-2 is representative for all the pellets. It displays some of the same behaviour as the polarisation-electric field of the pellets. The ϵ_r-electric field loops of the three pellets shows that the permittivity is lower for the highest applied electric field. The ϵ_r of the pellets behaves similarly for all three pellets.

Table 4.7: Relative permittivity, ϵ_r for coatings and pellets when no electric field is applied.

Sample ID	ϵ_r [-]
D-00-9	5.21
D-00-11	5.85
D-00-13	4.95
Dβ-30-11	121.0
Dβ-30-13	70.41
Dβ-40-9	89.39
Dβ-40-10	90.18
Dβ-40-11	89.26
Dβ-50-9	95.75
Dβ-50-10	109.97
Dβ-50-11	106.69
Dγ-30-9	61.67
Dγ-30-14	76.45
Dγ-30-15	65.99
Dγ-40-8	71.79
Dγ-40-9	96.61
Dγ-40-10	75.93
Dγ-50-6	82.96
Dγ-50-7	83.23
Dγ-50-8	92.29
Pγ-1	2372.2
Pγ-2	2274.5
Pγ-3	2217.8

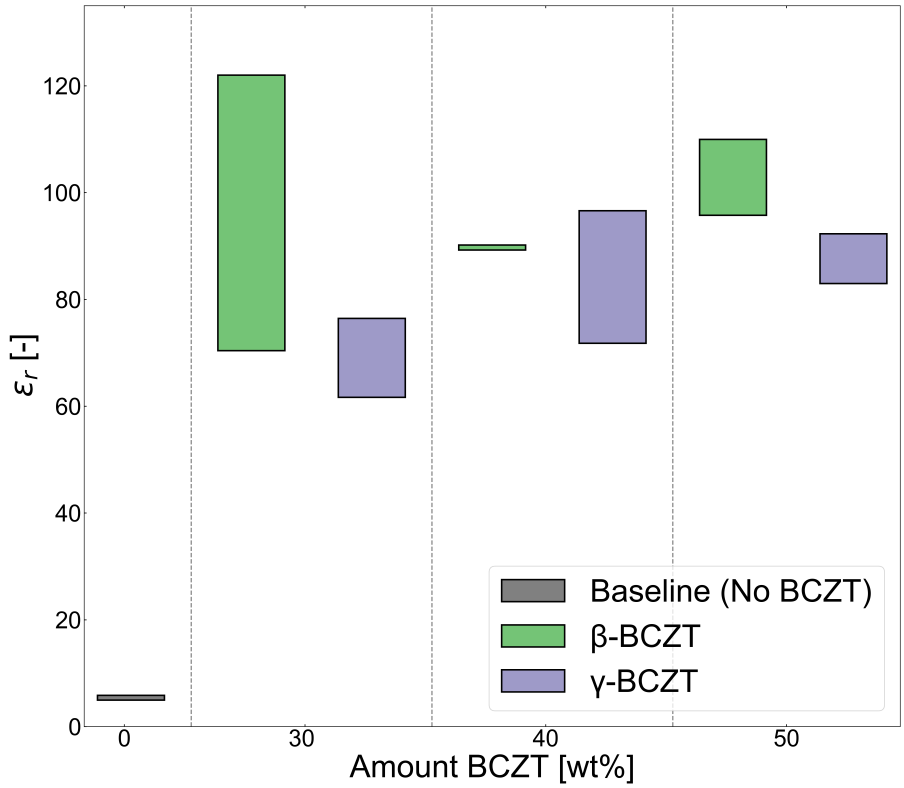

Figure 4.29: Relative permittivity, ϵ_r, of the coatings. The boxes stretch between the highest and lowest ϵ_r-value for each set of coatings.

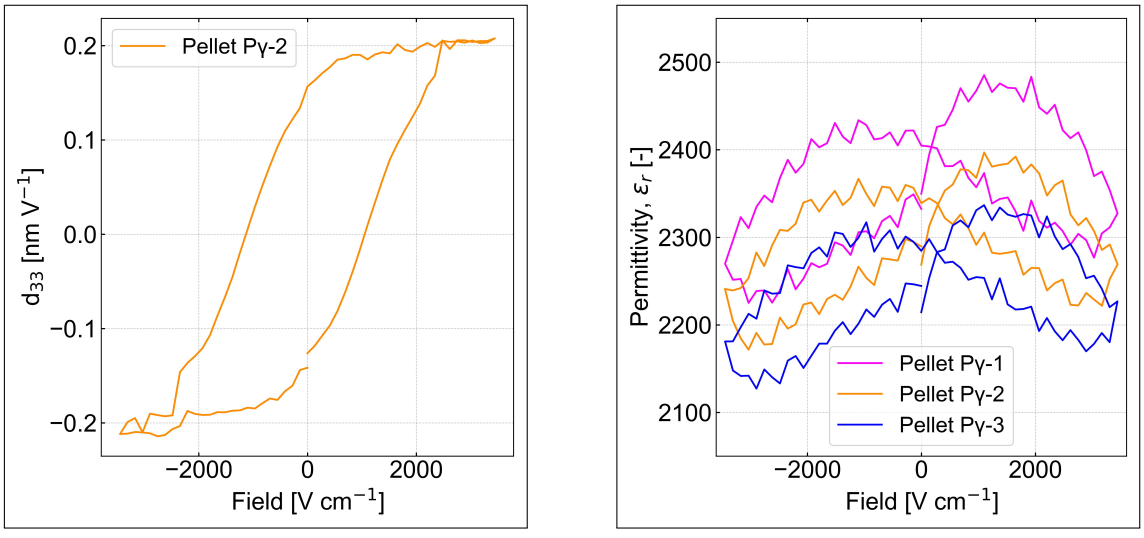

(a) **(b)**

Figure 4.30: (a) d_{33}-electric field and (b) ϵ_r-electric field of the BCZT pellets under an electric field.

5 Discussion

First the results regarding the BCZT/porcelain coatings are discussed, followed by a section on the synthesis of BCZT powders and pellets. Lastly, the piezoelectric properties of both the pellets and coatings are discussed together.

5.1 BCZT/Porcelain Coatings

5.1.1 Chemical Composition

The chemical composition of the BCZT/porcelain coatings has been analysed using both XRD-analysis and EDS-analysis. The resulting diffractograms from the XRD-analysis, given in Figure 4.14 are very similar, except for the diffractogram for the baseline sample. As expected there are no characteristic peaks of BCZT present there, since no BCZT powder was added to the baseline coatings. In all the diffractograms there are peaks matching the characteristic peaks of the Ti-6Al-4V substrate. The presence of peaks from the substrate show that the coatings are so thin that the XRD instrument is not able to measure only the coatings.

There are peaks in the diffractograms that do not match either BCZT or Ti-6Al-4V. These peaks are assumed to belong to the crystalline phases in the porcelains. These peaks are also visible in the diffractogram for the baseline coating, showing that they are not a result of adding BCZT to the coatings. The exact composition of these porcelains is not known so no attempt has been made to identify the peaks. The diffractograms curve upwards at higher 2θ angles. This is probably caused by the amorphous nature of the porcelain.

An EDS analysis was done on the cross section of three coating-samples to get a better understanding of their chemical composition. When discussing results from an EDS analysis it is important to note that some elements will have very close or overlapping characteristic energies, making them difficult to distinguish from each other. This includes Ba and Ti, as well as La and Ti. By doing an analysis of a specific point rather than a larger area there is also a larger uncertainty connected to the results. The point analysis is dependent on the operator finding a good point in the sample to measure. The placement of a point can mean measuring parts of a particle or the surrounding matrix instead. Measuring multiple point in the same area reduces the uncertainty somewhat.

The multipoint analysis in general found more elements in sample D-00-8 than in Dβ-30-7 and Dγ-30-11, as seen in Table 2.4. This was the case for the substrate, the bonder-layer and the dentin-phase, all of which should be the same for all samples. Ca, Ba, K, Na and Si was found in the substrate of D-00-8 but not in the other two samples. These elements are found in either the bonder or the dentin, suggesting that there might have been a cross-contamination. This could have happened during polishing of the cross section. If the sample was not cleaned enough between polishing and EDS analysis, these elements could remain in the sample. However, the same cleaning procedure was used for all samples.

Mg is however only found in D-00-8, and not in any of the components of the other samples. There is no known source for this contamination, especially since all samples underwent the same procedure and this is only found in one of them. The characteristic energy of Mg does not overlap with any of the other present elements. The presence of Ba in the substrate of D-00-8 should be taken with a grain of salt since Ba and Ti have overlapping energies, meaning that they cannot be distinguished. It is therefore not unexpected to identify Ba in a titanium alloy substrate.

The Ti-6Al-4V substrate has Al, C, N, Ti and V in all three samples. This is corroborated by the elemental maps in Figure 4.11, 4.13 and 4.12. The three alloying elements are expected, as well as the carbon due to carbon coating of the sample prior to analysis. Nitrogen can be added to Ti-6Al-4V alloys as a stabilizer.[88] This could be the source of the measured nitrogen.

The elemental maps of Al in all three samples show a concentration of Al close to the surface of the substrate. As mentioned in section 2.6, diffusion and segregation of Al has been observed in titanium alloys, for temperatures as low as 400 °C.[78] In this project the titanium alloy substrate has been heated to 780 °C and 810 °C for 6 and 1 minutes, respectively. These temperatures are well above the mentioned 400 °C, as well as higher than 750 °C which is where Lutz et al.[78] observed an increase in segregation. This behaviour should therefore be expected when heating these substrates.

Al, La and Sr are found in the bonder-layer of Dβ-30-7 and Dγ-30-11, but not in D-00-8. There is however, F, K, Mg, N, Si and Ti present in the bonder-layer of D-00-8 and not in the other two samples. There could be contamination from the other components of the sample explaining these differences, but it could also be that the placement of analysed points lead to different results. This is especially probable for the K and Si, as one would expect the presence of these in a porcelain. It is difficult to see, but the elemental maps of Dβ-30-7 and Dγ-30-11 in Figure 4.13 and 4.12 show that K is present in the bonder-layer. These maps also show that Si is not present in significant amounts in this layer. This supports the theory that point analysis is dependent on the placement of points versus the localization of elements. This variation in composition dependent on which parts of the sample is analysed suggests that the samples are not homogeneous.

Al, Ba, Ca, K, Na, O and Si were all found in the dentine-phase of the coatings. Al, K, Na, O and Si are expected since dental porcelains often contain both potash and sodium feldspar, quartz and alumina. Ca and Ba could be components of the porcelain, added by the supplier to adjust the properties, or they could originate from the BCZT powder. Based on the elemental maps Ca is a component of the porcelain as it can be seen in the whole dentine-phase, including in sample D-00-8. Ca is known to increase the coefficient of thermal expansion[25]. The presence of Ba in D-00-8 suggests that Ba is added to the porcelain as well.

The BCZT particles were confirmed as BCZT using EDS, but it seems like more of the dentin phase was measured alongside the BCZT particles in sample Dγ-30-11 compared to Dβ-30-7. Elements stemming from the dentin phase were measured in the BCZT particles of Dγ-30-11 but not in Dβ-30-7. The elemental maps of

these samples show Ba, Zr and Ti in what appeared to be BCZT particles in the corresponding SEM image. Ca is present in the whole dentin-phase, with no larger concentrations in the area of these particles.

The EDS analysis shows that the bonder- and dentin-porcelains have different chemical compositions. This is an expected result since the porcelains have different purposes and therefore need different properties. While the bonder is supposed to create good bonding between the layers, the dentin porcelain has to be able to be built as thicker layers. This is because dentin is generally used to build the shape of the dental restoration. The colour and translucency is more important in the dentin porcelain compared to the bonder, since dentin is the main constituent of the colour of the final restoration. Al could potentially be from the alumina, which is usually added to the dentin and not the bonder because viscosity and strength are more important in the main constituent of the porcelain body[25]. The difference in composition is also evident in SEM images of the coatings, where the two porcelains have different microstructures.

The chemical composition of each layer/component of the coatings is summed up in Table 5.1. All elements confirmed to be in each layer are listed under "Elements present", while the elements that most likely are contamination are listed under "Contamination elements".

Table 5.1: Summary of the chemical composition of the coatings. For each layer/component of the coatings, the present elements and contamination elements are listed.

Layer	Elements present	Contamination elements
Substrate	Al, N, Ti, V	C, Ca, K, Mg, Na, Si
Bonder	Al, Ca, K, Na, O, V	F, La, Mg, N, Si, Sr, Ti
Dentin	Al, Ba, Ca, K, Na, O, Si	F, Mg, N, V, Zr
BCZT	Ba, Ca, O, Ti, Zr	Al, K, Na, Si

5.1.2 Microstructure in Cross Sections and Surfaces

The microstructure of the coatings, visible in for example Figure 4.16a, resemble microstructure (b) "crystal-liquid structure" in Figure 2.12. This is the expected microstructure for viscous composite sintered porcelains where more than 20% of the total material is liquid phase at high temperatures[34]. The coatings made in this project contain at least 50 wt% porcelain, explaining why they have a similar microstructure to the "crystal-liquid structure". Both BCZT particles and a glassy phase are visible in the cross section of the coatings. The glassy phase is the darker, matrix material while the BCZT particles are lighter in colour in the SEM images. Only the glass phase is present in sample D-00-8 (Figure 4.15a) since no BCZT was added to the porcelain.

The SEM images of all the cross sections show two distinct porcelain layers, as shown in Figure 4.15b. While the dentine-phase is more of a continuous glass phase,

there are more particles present in the bonder layer. These could contribute to the adhesive properties of the porcelain. The presence of these layers show that the chosen approach of layering and firing multiple times is feasible to build structures without mixing the layers.

The same images show that there are pores present in all coating samples, and that the amount of pores increases with the amount of BCZT. There is some porosity in D-00-8, probably stemming from the fabrication of the coating. Air bubbles can be introduced to the porcelain slurry when the porcelain powder is mixed with its corresponding modelling liquid. Removing excess liquid prior to firing and firing under reduced pressure increases the removal rate of pores, but some pores can still be left after firing[26]. The pores in D-00-8 are distributed throughout the coating, but there are pores present along large sections of the bonder-dentin interface. This suggests that some air was trapped between the porcelain layers during the coating process. Pores are generally located in the BCZT/dentin-layer of the coatings, often with the first pores being right above the bonder-layer.

The addition of 30 wt% of β-BCZT increases the porosity and the size of the pores. This continues as the amount is increased to 40 wt% and 50 wt% β-BCZT powder. As the amount of BCZT is increased the pores become more irregularly shaped. The porosity is localised close to the BCZT particles. The same trend can be seen in the samples with γ-BCZT powder. However, there are more pores in these coatings compared to those with β-BCZT. This is especially visible when comparing Dβ-50-7 and Dγ-50-10 in Figure 4.18a and 4.19a, respectively. The pores are larger and more irregularly shaped in the coatings with γ-BCZT as well.

The densification of porcelain coatings depends on the amount of air present prior to firing, the porcelains ability to flow, and the porcelains ability to wet the particles. Based on sample D-00-8, some porosity is to be expected in all coatings, originating in the fabrication. However, the increase in porosity and the difference in porosity between the samples with BCZT indicates that both the presence of BCZT, the amount and the particle size affects the porosity.

There is an additional step in the fabrication procedure of the coatings when BCZT is added; mixing of the porcelain powder with BCZT powder. This step could result in more air in the porcelain body prior to firing. The powders have to be weighed out, mixed with a mortar and pestle, and finally moved to a porcelain slab before modelling liquid is added. The extra moving of the powders as well as the mixing method could introduce more air to the powder mixture, and subsequently to the final porcelain body. If this was the only source for the extra porosity, there would not be such large differences between the coatings. Therefore, more factors contribute.

The resulting BCZT/dentin powder mixes have different particle size distributions, as shown in Figure C.2e and C.2c. The β-BCZT powder is more similar in particle size to the dentin powder than the γ-BCZT powder is. The dentin powder does have both smaller and larger particles. The difference in particle size distribution between the powder mixes could have contributed to the difference in porosity. Different PSD could result in different packing of the powders.

The difference in porosity-evolution between the coatings with β- and γ-BCZT powder suggest that the smaller particles of BCZT are more detrimental to the density of the coatings than larger particles. The smaller γ-BCZT particles seem to be able to form (almost) connected networks throughout the coating, which means that there is percolation in these coatings. Thus, the particles in coatings with β-BCZT are further apart than in coatings with γ-BCZT. This could result in the γ-BCZT hindering the flow of the glassy phase to a larger degree, as there is smaller spaces to flow between and more particles acting as obstacles for the flow. The flow will then be hindered more as the amount of BCZT powder is increased for both powders since the amount of obstacles, i.e. particles, increases.

The densification rate is generally increased if the molten glass phase is able to wet the solid particles[34]. Surfaces with high energies are easier to wet[26], and surfaces with larger surface areas have higher surface energy. From the BET analysis it was found that the smaller γ-BCZT particles have a larger specific surface area than the larger β-BCZT particles. There are some limitations to this method, namely that it assumes spherical particles. However, due to the large differences in particle size it can be assumed that γ-BCZT has a larger surface area, even if the exact area is uncertain. Based on this, the molten glass phase should wet the γ-BCZT particles better than the β-BCZT particles. However, the observed percolation and agglomeration of γ-BCZT powder will reduce the effective surface area of the particles.

However, the SEM images show more porosity in the coatings with γ-BCZT powder. The wettability of the porcelain on the BCZT can therefore not be the most important factor for the densification of the coatings. The difference in surface area is at least not that important to the final wetting of the particles. Poor wetting combined with reduced and hindered flow could be an explanation of the change in porosity in the coatings.

The bonder-dentin interface and the substrate-porcelain interface are nice for all samples and generally look like the interfaces in sample Dγ-40-7, shown in Figure 4.20b. There are no gaps or pores between the layers. From these SEM images it seems like the glassy phase of the porcelains are able to flow and fill the crevices on the substrate and on the bonder-layer. This shows that the flow of porcelain was good at the firing temperatures. The firing temperatures were higher than the glass transition temperature for both the bonder- and the dentin-porcelain, which means that the glass phase should be able to flow[26].

During fabrication of these coatings it was however observed that a firing time of 1 minute, which is what the porcelain manufacturer recommends, was not sufficient for densification of the porcelains. Initial testing of coatings held at maximum temperature (T_{max}) for 1 minute showed that the porcelain had not been able to flow around the BCZT particles. Good flow of the molten glass phase was observed when the hold time at T_{max} was increased to 6 minutes. These observations suggest that the BCZT particles take up some of the energy applied through firing, making a longer holding time at T_{max} necessary. The heat capacity of the BCZT could therefore be another reason why the presence of BCZT hinders flow, and thus densification, of the coatings. One would expect that the increased firing time would

result in further densification.

As stated previously, little to no porosity is found within the bonder-layer of the coatings. There is no BCZT present in the bonder-layer, thus this porcelain will not be affected by BCZT. The handling of the bonder-porcelain is also different from that of the dentin-porcelain. The bonder is applied as a thin wash, while dentin is applied in a thicker layer. There is less space for air bubbles in the thin wash. Excess liquid will also evaporate quicker from the bonder since the layer is thinner and the total amount of liquid is smaller. These factors could have contributed to the lack of pores in this layer. Vibration was used on all samples prior to firing the BCZT/dentin layer. This was done to increase the consolidation of the porcelain green body. Increased consolidation should also be beneficial for reducing porosity.

The BCZT particles are relatively well distributed throughout the coating, but not completely homogeneously. This probably stems from the mixing of BCZT powder with dentin powder. The SEM images (Figure C.2) of the powder mixes corroborate this as the distribution is inhomogeneous there as well. The powder distribution was only checked with SEM once for 50/50 β-BCZT/dentin and for 30/70 γ-BCZT/dentin to evaluate whether mixing with a pestle and mortar was a possibility. The distribution was deemed good enough, so the method was implemented into the process but the distribution was not checked for subsequent powder mixes. The powder mixes used for the coatings were mixed until the powders looked like they had combined well. There is therefore an uncertainty in the homogeneity of the distributions of the powder mixes. However, based on the imaged powder mixes the distribution of BCZT and dentin in the fired coatings can be expected to vary between coatings, in terms of placement of the BCZT particles. An inhomogeneous powder mixture can also result in inhomogeneity within coatings made from the same powder mix. This contributes to variation within a set of samples.

The surfaces of the coatings show both glass phase and BCZT particles. There are also markings which appear to be from the sanding process. All samples underwent the same sanding procedure. The porosity present on the surfaces could be pores from air bubbles, but there could also be craters left from BCZT particles that have been removed from the surface during the sanding process.

5.1.3 Bond Strength

The coatings with 40 wt% β-BCZT had the highest values for bond strength, followed by the coatings with 40 wt% γ-BCZT. The coatings with β-BCZT powder in general performed better than those with γ-BCZT powder. The higher porosity in coatings with γ-BCZT could have contributed to this result. However, the substrate-porcelain interface is nearly identical in all imaged samples independent of particle size. The porcelain has therefore been able to flow properly and wet the substrate, which should provide good adhesion. It should be noted that only 12 of 49 samples measured bond strengths above the 25 MPa requirement in ISO 9693:2019. The highest measured bond strength was 33.7 MPa (sample Dβ-40-4).

There is some variation in measured bond strength within each set of samples.

Additionally, there were coatings that broke during the sanding process. These either broke in two or, in most cases, broke off from the substrate. This indicates that the fabrication process has been unable to produce uniform samples, and the actual bond strength variation is bigger than what was able to be measured.

As discussed previously, there are microstructural differences in the coatings such as distribution of BCZT particles and porosity. In addition to these, the fabrication process in itself can lead to inhomogeneity between the coatings within the same set of samples. The fabrication process up to firing is done completely by hand, thus there is a human factor contributing to variation. Establishing a good technique and procedure is therefore important.

The thickness of the oxidation layer on the substrate is important for the bond strength of the final coating.[25] The oxidation layer was not observed during SEM imaging of the cross sections of the coatings. The oxide layer thickness will be affected by the sandblasting of the substrate as well as the time from sandblasting to application of porcelain. Sandblasting is done at a 45° angle until the substrate is visibly matted in colour. The angle can vary between each substrate, as well as the time spent sandblasting. This will depend on the operator.

The time between sandblasting and application of porcelain is also the time in which the new oxidation layer is allowed to form. This should not exceed 15 to 20 minutes. In order to reduce the oxidation time, and to be as consistent as possible between samples, only 3 to 4 samples were made at a time. The bonder-layer was applied as a thin wash and minimal shaping of the porcelain was necessary after application. This meant that a short time was spent on each sample, further minimizing the allowed oxidation time and the variation between the samples. These two steps, and the previously discussed powder mixing, show that the coating process is dependent on the operator and their technique and experience.

The variation is biggest is the coatings with β-BCZT. There are fewer and smaller pores here, so the larger variation could indicate that the distribution of particles has a greater impact on the bond strength for larger particles. The SEM images of the underside of the fractured coatings (see Figure 4.23b) show that some BCZT particles have been present in the layer where the coating has fractured. The porcelain creates the adhesion between the layers. Thus, BCZT particles reduce the surface area where the layers are connected, potentially reducing the overall bond strength of the coating. The larger particles will result in larger, concentrated areas where there is no adhesion, compared to the smaller areas caused by the small γ-BCZT particles. This could explain why coatings with β-BCZT have larger variation in bond strength.

From the SEM images of the fractured samples (Figure C.3a) one can see that the coatings have fractured in an "End of ceramic"-type of fracture. This means that the coatings delaminate from the substrate rather than fracturing. However, the images of a completely broken off coating in Figure 4.23 indicate that the fracture has gone through the the bonder-dentin interface rather than between the substrate and the bonder layer. The same type of particles that are present in the bonder-layer in the cross sections are still left on the substrate where the coating was. The underside of the porcelain also shows BCZT particles, which means that the fracture has been

close to the dentin-layer. So, the coatings have actually delaminated in the porcelain rather than from the substrate. The presence of BCZT particles this close to the fracture could help explain why the fracture happened here. The BCZT particles reduce the available surface area for porcelain-adhesion, as discussed previously. This could weaken the bond between the porcelain layers. The presence of pores at or above the bonder-layer could also contribute to the placement of the fractures.

The coefficient of thermal expansion (CTE) of the different materials will affect the strength and compression of the system. The difference in CTE is less than 10^{-1} K^{-1} for the porcelain and Ti-6Al-4V, with Ti-6Al-4V having the higher CTE (see Table 2.1, 2.2 and 2.3). The thermal expansion of the porcelain and metal substrate should therefore affect the bond strength to a small degree. At the substrate-porcelain interface the porcelain is in compression, which is beneficial for the strength of the coatings. However, the CTE of the filler BCZT particles also has to be considered. BCZT has a lower CTE than the porcelains, meaning that BCZT is under compression while the porcelain is under tension close to the particles. This increases the stress and the chance of fracture in the porcelain around the particles. Still, there is only a small mismatch between BCZT and the porcelains of $\approx 0.6 \cdot 10^{-6}$ K^{-1}, suggesting that the effect of thermal expansion mismatch between these two materials is minimal.

The estimated coefficient of thermal expansion of BCZT is more than 10^{-1} K^{-1} lower than the CTE of Ti-6Al-4V. However, other compositions of BCZT have slightly higher coefficients, thus the actual difference might be lower. Still, the difference is largest for BCZT and Ti-6Al-4V. The thermal expansion mismatch between these two materials will therefore affect the overall coating the most close to the BCZT particles that are closer to the substrate.

5.2 Solid-State Synthesis of BCZT

5.2.1 Chemical Composition

The XRD analysis of the β-BCZT powder in Figure 4.1 show that the synthesis resulted in $(Ba_{0.85}Ca_{0.15})(Zr_{0.1}Ti_{0.9})O_3$ as well as some additional, unwanted compounds. The XRD analysis of γ-BCZT powder show that this powder had the desired $(Ba_{0.85}Ca_{0.15})(Zr_{0.1}Ti_{0.9})O_3$ composition. However, from Table B.3 it is clear that an excess of $CaCO_3$ precursor was added to both powders. The excess is greater in β-BCZT, which might be why the additional compounds were only measured in this powder. The calcium-excess can have affected the mechanical, thermal and piezoelectric properties of the BCZT powder used in this project. The XRD analysis of the pellets made with γ-BCZT powder showed no significant changes in composition from the analysis of the powder. This is as expected from the sintering process.

5.2.2 Morphology and Size of Powders

The particle size distributions (PSD) of β-BCZT and γ-BCZT powder in Figure 4.3 show that the synthesis resulted in two different particle sizes, which was the goal. The mean particle size of the β-BCZT powder did not change much from the first calcination to the recalcination, but the PSD became broader. The recalcination was done on loose powder, which was not milled afterwards. A certain coarsening from the recalcination is expected. Without milling afterwards the broader PSD is also expected. The SEM images of the powders support these results.

The PSD of the β-BCZT powder changed as it was measured. This change can be seen in Figure E.2. Some of the measurements done after the first calcination shift to the right while others shift to the left. There is an increase in the quantity of particles with a particle diameter of approximately 200 µm in all measurements after the first one. There is some unsteadiness present in the measurement of the recalcined powder as well. This could have been caused by agglomerates of the powder forming, thus resulting in the observed increased quantity of larger particles. The distribution after recalcination shifts along the x-axis as more measurements are performed, further suggesting that there is some agglomeration happening.

The first measurement of the PSD of γ-BCZT powder deviates from the next four measurements. The first measurement shows more particles above 3 µm, and fewer particles around 1 µm. The stability in the next measurements suggest that this might be an artefact, or that the first measurement was done before the solution was able to stabilize properly.

The powders have similar morphologies. The particles are more angular than spherical. There are more particles that look like broken chunks of a pellet in the γ-BCZT powder compared to the β-BCZT. Recalcination of β-BCZT as a loose powder, and the subsequent coarsening, could be the reason for why there appear to be fewer of these chunks. The particles were able to grow, while the γ-BCZT particles have only been milled and then imaged.

5.2.3 Microstructure of Pellets

Pellets for sintering were pressed using only γ-BCZT powder. It was not possible to press pellets from the β-BCZT powder, even after testing with a wide range of pressing forces. The large particle size of this powder could have made it difficult to press pellets that held together.

From the porosity measurements and the SEM images it seems like the sintering of the pellets did not move past the intermediate sintering stage. There is between 8 and 10 % open porosity in all pellets. From the as-sintered surfaces in Figure 4.7 and 4.8 one can see small pores at the grain boundaries, as well as larger, continuous pores going along multiple grains. The evolution in porosity during solid state sintering is illustrated in Figure 2.11, which also shows that the intermediate stage of sintering continues until the pores no longer are connected[34].

Pellet Pγ-1 is the most porous pellet, but it is also the pellet with the most closed porosity. All the porosity in Pγ-2 is open, while only 0.26 vol% of the porosity in Pγ-3 is closed. This suggests that the pellets reached different stages of the sintering even though they were sintered together, in one crucible. The same temperature program has previously been used to make bulk samples of the same composition, which resulted in a relative density of 99 %[13]. The particle size distribution is relatively narrow, but there are particles ranging from sub-micron diameter to approximately 10 µm. This should improve packing of the powder, and contribute to a higher density. Still, the density of the pellets is lower than expected for this composition.

However, there is a calcium-excess in the powder that was not present in the previously mentioned bulk samples of 99 % relative density. This excess could influence the sintering process and thus the final density of the pellets. During sintering the pellets changed from a white-ish colour to a dark grey, as shown in Figure 5.1. This colour change was unexpected and could also potentially be attributed to the calcium-excess in the powder.

Figure 5.1: Pellets after sintering.

5.3 Piezoelectric Properties

The piezoelectric properties of the pellets and coatings were tested to better understand the effect of adding BCZT particles to a porcelain matrix. The pellets all displayed the expected behaviour in terms of polarisation and strain when an electric field was applied. The polarisation loop of the pellets, in Figure 4.24, display hysteresis behaviour associated with piezoelectric materials. Pellet Pγ-1 shows higher saturation polarisation, P_s, and remnant polarisation, P_r, compared to Pγ-2 and Pγ-3. Pγ-2 and Pγ-3 show identical polarisation-behaviour. From the porosity values in Table 4.3 one would expect Pγ-1 to show lower P_s and P_r, as higher porosity generally is associated with lower piezoelectric properties[51] [55]. Irregular pores affects the P_s and P_r more than spherical pores, which could explain why Pγ-1 shows higher P_s and P_r.

Pγ-1 also shows higher degree of strain compared to Pγ-2 and Pγ-3. This corresponds to the higher P_s and P_r values. The strain-electric field hysteresis loop has a

butterfly-shape for all three pellets. This is expected for bulk piezoelectric materials. The d_{33} values measured with the Berlincourt-meter, given in Table 4.6, show that the poling process of the pellets has been successful. The highest value of 142 pC/N is however significantly lower than the 527 pC/N and 620 pC/N that have been reported previously [61] [62]. The porosity and composition of the pellets probably contribute to the lower piezoelectric coefficient. The excess of calcium could also have an effect on this. Figure 4.30a shows that the piezoelectric coefficient of the pellets also has a hysteresis-loop when an electric field is applied. The shape of this loop follows that of the polarisation-electric field loop.

The polarisation- and strain-electric field loops of the baseline coatings in Figure 4.25 show that the porcelain is a dielectric material, while the strain is so small that it is mostly noise. The polarisation-loops are very similar for all three coatings. The microstructure can have an effect on these loops, the similar shape indicates that the microstructure of these coatings is similar as well. The dielectric behaviour is expected as these coatings contain no BCZT.

The coatings with 30 wt% β-BCZT display the same thin polarisation loops indicating dielectric behaviour. The addition of 40 wt% β-BCZT results in a wider polarisation-loop, with a higher remnant polarisation. This shows that adding BCZT increases the piezoelectric behaviour of the coating. However, the addition of 50 wt% β-BCZT reduces the remnant polarisation, indicating a decline in piezoelectric behaviour. The coatings with the smaller γ-BCZT particles see the same increase in piezoelectric behaviour, and it continues to increase with the addition of 50 wt% γ-BCZT.

Porosity will reduce the piezoelectric behaviour, partially because of the reduced amount of piezoelectric material. In these coatings the mass of piezoelectric material is controlled and the same within each set of samples. The porosity is found in the dentin-phase of the coatings and not within the BCZT particles. This means that the pores only to a small degree replaces BCZT. Thus, the effect of reduced piezoelectric material is not the main contributor to the reduced polarisation behaviour in the coatings with 50 wt% β-BCZT.

The lower permittivity of pores can result in inhomogeneous distribution of the electric field during the poling process [51] [55]. The increased porosity in Dβ-50 - coatings will give a more inhomogeneous electric field distribution, with a concentration of the field around the pores. This means that the BCZT particles will feel a lower electric field, which could result in fewer particles being successfully poled even though the applied electric field is higher than the coercive field.

The permittivity measurements showed that the baseline coatings have a significantly lower permittivity than the BCZT pellets. This means that the glass phase in the BCZT/porcelain coatings will have a similar effect as the pores on the overall electric field distribution. The electric field will concentrate in the glassy phase-matrix as well, resulting in the BCZT particles feeling even less of the electric field. This concentration of electric field around the interfaces of phases with different permittivity has been observed in composites of hydroxyapatite and barium titanate which, while they are not the same material system as the coatings, have a similar structure [56] [59]. These composites can therefore give an insight into the expected

behaviour of the BCZT/porcelain coatings.

The reduction in permittivity in composites compared to bulk samples seen for hydroxyapatite/barium titanate composites, is observed in these BCZT/porcelain coatings as well. The relative permittivity of each coating was measured, as shown in Figure 4.29. The BCZT pellets had permittivities around 2200 - 2300, which is quite a bit higher than the relative permittivity of 5 for the baseline coatings. The BCZT/porcelain coatings have permittivities between 60 and 120, which is a significant reduction from the permittivity of the pellets. The permittivity of the Dβ-30 and Dβ-50 - coatings are higher than their γ-BCZT counterparts.

If the porosity was solely responsible for the reduction in polarisation behaviour of the coatings one would expect the Dγ-50 - coatings to display the poorest behaviour as these have more pores, and the pores are less spherical compared to the Dβ-50 - coatings.[53] [54] The Dγ-50 - coatings actually have the highest values for P_s and P_r. This could be due to percolation of the BCZT particles. If the particles are able to form a network the poling process could be improved since the connected particles will affect each other. The placement and size of the BCZT particles will therefore influence the degree of percolation. Percolation combined with more piezoelectric material in the Dγ-50 - coatings could be why these coatings show the best polarisation-electric field loops.

The placement and size of BCZT particles will in general affect the hysteresis-curves of a coating. The polarisation-electric field loops of Dβ-30-13 and Dβ-30-13 in Figure 4.27a have different slopes. This could be caused by differences in microstructure. The microstructure can, as previously discussed, vary within a set of coatings since the BCZT/dentin powder mixes are not completely homogeneous. The polarisation loop of Dγ-50-8 deviates from the polarisation loop of Dγ-50-6 and Dγ-50-7. This deviation could also be caused by microstructural differences between the coatings.

The amount of BCZT particles and their placement, as well as the overall porosity, electric field distribution and degree of percolation will all affect the final poling of the coatings. The polarisation-electric field loops of the BCZT/porcelain coatings show that these factors are important, and that they vary between the samples.

The measured strain is very low for all coatings. The measurements of displacement were done using a 0.63 µm calibration factor in the *aixPlorer* software, while the output from the software was displacement values on the nanometer-scale. The calibration factor combined with the very low strain-values suggest that the plotted strain-loops are mostly noise. Still, this means that the overall strain of the coatings was small. The small strain could be explained by two theories. One theory is that the inhomogeneous electric field distribution caused by low permittivity in the porcelain-matrix and pores, results in incomplete poling of the coatings. Another is that the poling process has been successful, but that the porcelain-matrix compensates for or conceals the strain in the BCZT particles. If this happens, the instrument will not measure strain in the whole coating.

When measuring the piezoelectric coefficient in the AIX PES instrument, it is the indirect piezoelectric coefficient that is measured with the unit nm/V. This measure-

ment depends on the instrument being able to measure strain in the sample. Thus, if the strain is so low in the whole coating that it is not measured, low values of the indirect piezoelectric coefficient will be measured. This can be seen in Table 4.6, where the values for indirect piezoelectric coefficient are close to 0 for all coatings.

The direct piezoelectric coefficient was measured for the coatings as well, this was done using a Berlincourt-meter. These measurements resulted in average d_{33} values for all coatings between 0.8 - 1 pC/N. This might indicate that the poling of the coatings has been unsuccessful. The piezoelectric coefficient of these coatings cannot be determined from these results. Adding more BCZT particles could be necessary to be able to measure the piezoelectric coefficient. Pisitpipathsin et al.[70] were unable to measure the d_{33} of composites of BCZT and 45S5 bioglass for compositions with less than 80 % BCZT. This is a different material system than the BCZT/porcelain coatings, but an increased amount of BCZT particles might be necessary for these coatings as well.

Reducing the porosity and improving the homogeneity of the coatings would also improve the piezoelectric properties and reduce the variation in results between the samples.

6 Conclusion

The present study has investigated the effect of adding BCZT to dental porcelain on the piezoelectric properties and bond strength of these coatings. $(Ba_{0.85}Ca_{0.15})(Zr_{0.1}Ti_{0.9})O_3$ (BCZT)/porcelain coatings on Ti-6Al-4V substrates were successfully prepared using a coating procedure based on procedures for porcelain dental restorations. The piezoelectric composite coatings were created by layering a bonder porcelain with a BCZT/dentin porcelain mixture.

X-ray diffractograms and calculations based on precursor amounts of the two BCZT powders β-BCZT and γ-BCZT showed that there were other compounds present in addition to the the $(Ba_{0.85}Ca_{0.15})(Zr_{0.1}Ti_{0.9})O_3$ composition. The sintered γ-BCZT pellets all had lower relative densities than expected, ranging from $\approx$ 80 - 90 %. The remaining porosity in these coatings was largely open porosity. This was also observed on the as-sintered surface of the pellets. The additional compounds and reduced density were attributed to the Ca-excess in the powder, which could negatively affect the density and piezoelectric properties of the coatings and BCZT pellets.

The porosity of the coatings increased with the amount of BCZT powder. The smaller particles of γ-BCZT, relative to β-BCZT, resulted in higher porosity with more irregularly shaped pores. The microstructure of the coatings demonstrated some inhomogeneous features. The bonder-dentin interface and the substrate-porcelain interface do however look almost identical in all samples. This shows that the use of an initial bonder-layer for improved adhesion resulted in consistent interfaces across the coatings.

The coatings with 40 wt% BCZT had the highest bond strength, with the larger β-BCZT particles performing better than the smaller γ-BCZT particles. The baseline coatings showed the lowest bond strength, indicating a positive effect of adding BCZT. Only 12 of the samples exhibited a bond strength above the requirements of ISO 9693:2019, where the highest bond strength of 33.7 MPa was observed for Dβ-40-4. All the fractures were of the "End of ceramic"-type, which means that the bond strength results are valid.

The BCZT pellets displayed the expected piezoelectric response to an electric field. The highest measured d_{33} value was 142 pC/N, which is lower than previously reported values of 620 pC/N. This could be caused by the porosity of the pellets as well as the Ca-excess in the BCZT powder.

The baseline coatings displayed dielectric behaviour. This was also observed for the coatings with 30 wt% BCZT, indicating that 30 wt% was not sufficient to elicit a piezoelectric response. The saturation polarisation and remnant polarisation of the coatings increased for coatings with 40 wt% BCZT. The best piezoelectric properties were observed in the coatings with 50 wt% γ-BCZT, while a reduction was observed for 50 wt% β-BCZT. This was probably due to percolation of the γ-BCZT particles.

The piezoelectric properties of the coatings were affected by porosity and distribution of particles within the coating. This, and the permittivity of the materials af-

fected the distribution of the electric field. The permittivity of the BCZT/porcelain coatings was significantly lower than for the BCZT pellets, in line with observations done on hydroxyapatite/barium titanate composites[56] [57] [58]. This reduced the piezoelectric properties of the BCZT/porcelain coatings.

The strain of the coatings was very low. This is most likely either caused by unsuccessful poling of all the BCZT particles in the coatings, or due to the porcelain concealing and/or compensating for the strain in the BCZT particles. The same applies to the piezoelectric coefficient of the coatings.

The results of this study could be improved by working with pure $(Ba_{0.85}Ca_{0.15})(Zr_{0.1}Ti_{0.9})O_3$ powder, sintering denser BCZT pellets, and achieving less porous coatings. It could be interesting to test the wettability of the porcelain on the BCZT particles to better understand the wetting mechanisms in the coatings, and as a way of improving the coatings. Further testing is required before these coatings can be used for biomedical applications, but this study shows promising results for mixing BCZT with dental porcelains.

7 Further Work

The porosity of these coatings seem to have a detrimental effect on their bond strength and piezoelectric properties. The coating procedure should therefore be optimised to reduce the porosity as well as increase the homogeneity across different samples. A more homogeneous powder mixture of BCZT and dentin porcelain could for example improve the homogeneity of the coatings. A more narrow particle size distribution of this powder mixture could potentially also help, as this could be thought to improve the distribution of BCZT particles in the coatings. Both the homogeneity and particle size distribution could be improved by using a different method for mixing the powders, for example ball milling. Studying the wettability of porcelain on the particles could further increase our understanding of this system. The results indicate that the coatings are very sensitive to the procedure and the technique of the operator. Automation of parts of or the whole process should therefore be looked into. This could potentially reduce the variation between coatings.

The bond strength of the coatings can be improved in other ways in addition to improving the overall microstructure. Dental porcelains have different compositions based on their function, as well as differences between the manufacturers. It could therefore be beneficial to evaluate coatings with different dental porcelains to see whether they are more compatible with the BCZT powder. Other materials for the initial, adhesive layer could also be investigated. It can be difficult to obtain good adhesion between dental porcelains and titanium substrates. Because of this difficulty it is also possible to consider other metal substrate materials, and study how the adhesion of the coatings changes with the substrate material. Alternative metals include stainless steels and CoCr-alloys.

The piezoelectric properties of these coatings can be further improved. To get a better understanding of the effect the BCZT powder has on the porcelain in terms of piezoelectric properties, a study should be done using a phase pure $(Ba_{0.85}Ca_{0.15})(Zr_{0.1}Ti_{0.9})O_3$ powder. Based on this study, increased amounts of BCZT could be of interest to test. This is however dependent on a better procedure that is able to prepare less porous coatings. In addition to this, it would be interesting to look into the effect of poling at higher electric fields. An alternative to increasing the amount of BCZT in the coatings would be to utilise other piezoelectric ceramics with an intrinsically higher piezoelectric coefficient.

If the piezoelectric properties are found to be acceptable, further testing of the coatings is necessary before they can be used for their intended biomedical applications. The mechanical properties of the coatings have to be further evaluated. It would for example be interesting to see how the coatings behave when they are exposed to repeated loads. The intended purpose in biomedical applications means that the coatings will be exposed to the environment in the human body. Thus, tests should therefore be done where the coatings are exposed to similar environments. A natural starting point for this would be soaking studies in for example simulated body fluid (SBF).

Lastly, this study has looked at the bond strength and piezoelectric properties when

the coatings are applied to a rectangular, flat substrate. The coatings should be applied on substrates with the same geometry as the intended purpose of the coatings, to understand how the change in geometry affects the coatings and whether the coating procedure has to be adapted for curved surfaces.

Bibliography

[1] M. N. Rahaman, A. Yao, B. S. Bal, J. P. Garino, and M. D. Ries, "Ceramics for Prosthetic Hip and Knee Joint Replacement," *Journal of the American Ceramic Society*, vol. 90, no. 7, pp. 1965–1988, 2007. _eprint: https://onlinelibrary.wiley.com/doi/pdf/10.1111/j.1551-2916.2007.01725.x.

[2] S. Todros, M. Todesco, and A. Bagno, "Biomaterials and their biomedical applications: From replacement to regeneration," *Processes*, vol. 9, no. 11, p. 1949, 2021.

[3] M. Z. Ibrahim, A. A. D. Sarhan, F. Yusuf, and M. Hamdi, "Biomedical materials and techniques to improve the tribological, mechanical and biomedical properties of orthopedic implants – A review article," *Journal of Alloys and Compounds*, vol. 714, pp. 636–667, Aug. 2017.

[4] W. R. Wagner, S. E. Sakiyama-Elbert, G. Zhang, and M. J. Yaszemski, *Biomaterials Science: An Introduction to Materials in Medicine*. Academic Press, May 2020.

[5] L. M. Bjursten, L. Rasmusson, S. Oh, G. C. Smith, K. S. Brammer, and S. Jin, "Titanium dioxide nanotubes enhance bone bonding in vivo," *Journal of Biomedical Materials Research Part A*, vol. 92A, no. 3, pp. 1218–1224, 2010.

[6] M. Navarro, A. Michiardi, O. Castaño, and J. Planell, "Biomaterials in orthopaedics," *Journal of The Royal Society Interface*, vol. 5, no. 27, pp. 1137–1158, 2008. Publisher: Royal Society.

[7] J. Henkel, M. A. Woodruff, D. R. Epari, R. Steck, V. Glatt, I. C. Dickinson, P. F. M. Choong, M. A. Schuetz, and D. W. Hutmacher, "Bone Regeneration Based on Tissue Engineering Conceptions — A 21st Century Perspective," *Bone Research*, vol. 1, pp. 216–248, Dec. 2013. Number: 1 Publisher: Nature Publishing Group.

[8] M. Griffin and A. Bayat, "Electrical Stimulation in Bone Healing: Critical Analysis by Evaluating Levels of Evidence," *Eplasty*, vol. 11, p. e34, 2011.

[9] P. R. Kuzyk and E. H. Schemitsch, "The science of electrical stimulation therapy for fracture healing," *Indian Journal of Orthopaedics*, vol. 43, no. 2, pp. 127–131, 2009.

[10] E. Fukada and I. Yasuda, "On the Piezoelectric Effect of Bone," *Journal of the Physical Society of Japan*, vol. 12, no. 10, pp. 1158–1162, 1957.

[11] S. A. M. Tofail and J. Bauer, "Electrically Polarized Biomaterials," *Advanced Materials*, vol. 28, no. 27, pp. 5470–5484, 2016. _eprint: https://onlinelibrary.wiley.com/doi/pdf/10.1002/adma.201505403.

[12] V. Jarkov, S. J. Allan, C. Bowen, and H. Khanbareh, "Piezoelectric materials and systems for tissue engineering and implantable energy harvesting devices for biomedical applications," *International Materials Reviews*, pp. 1–51, 2021.

[13] K. K. Poon, *Development of Piezoelectric BCZT Ceramics as Electroactive Bone Implant Material*. NTNU, 2020. Accepted: 2020-05-06T12:10:12Z ISSN: 1503-8181.

[14] C. E. Misch, "Chapter 1 - Rationale for Dental Implants*," in *Dental Implant Prosthetics (Second Edition)* (C. E. Misch, ed.), pp. 1–25, St. Louis: Mosby, Jan. 2015.

[15] Y. A. Arteaga, "17 - Esthetics and Implant Prosthetics," in *Esthetic Dentistry (Third Edition)* (K. W. Aschheim, ed.), pp. 379–404, St. Louis: Mosby, Jan. 2015.

[16] Nissin Dental Products INC, "Prosthodontics (Pro) Patient Education Model [PE-PRO012]." Available at https://www.nissin-dental.net/products/PatientEducationModels/PROSTHODONTICS/PE-PRO020/index.html.

[17] J. Kelly, I. Nishimura, and S. D. Campbell, "Ceramics in dentistry: Historical roots and current perspectives," *The Journal of Prosthetic Dentistry*, vol. 75, no. 1, pp. 18–32, 1996.

[18] S. Bayne, J. Ferracane, G. Marshall, S. Marshall, and R. van Noort, "The Evolution of Dental Materials over the Past Century: Silver and Gold to Tooth Color and Beyond," *Journal of Dental Research*, vol. 98, pp. 257–265, Mar. 2019.

[19] G. W. Ho and J. P. Matinlinna, "Insights on Ceramics as Dental Materials. Part I: Ceramic Material Types in Dentistry," *Silicon*, vol. 3, pp. 109–115, July 2011.

[20] L. Culp, N. Y. Wong, and C. E. Misch, "Chapter 27 - Digital Technology in Implant Dentistry," in *Dental Implant Prosthetics (Second Edition)* (C. E. Misch, ed.), pp. 700–723, St. Louis: Mosby, Jan. 2015.

[21] M. Harsono and G. Kugel, "23 - Esthetics and computer-aided design and computer-aided manufacturing (CAD/CAM) systems," in *Esthetic Dentistry (Third Edition)* (K. W. Aschheim, ed.), pp. 479–485, St. Louis: Mosby, Jan. 2015.

[22] M. Javaid and A. Haleem, "Current status and applications of additive manufacturing in dentistry: A literature-based review," *Journal of Oral Biology and Craniofacial Research*, vol. 9, pp. 179–185, July 2019.

[23] A. Tahayeri, M. Morgan, A. P. Fugolin, D. Bompolaki, A. Athirasala, C. S. Pfeifer, J. L. Ferracane, and L. E. Bertassoni, "3D printed versus conventionally cured provisional crown and bridge dental materials," *Dental Materials*, vol. 34, pp. 192–200, Feb. 2018.

[24] E.-J. Bae, I.-D. Jeong, W.-C. Kim, and J.-H. Kim, "A comparative study of additive and subtractive manufacturing for dental restorations," *The Journal of Prosthetic Dentistry*, vol. 118, pp. 187–193, Aug. 2017.

[25] W. P. Naylor, *Introduction to Metal-Ceramic Technology: Third Edition*. Quintessence Publishing Co, 2019.

[26] B. W. Darvell, *Materials Science for Dentistry*. Elsevier Science, 2018.

[27] M. C. Wood, G. A. Thompson, and J. R. Agar, "A comparison of debonding strengths of four metal-ceramic systems with and without opaque porcelain," *The Journal of Prosthetic Dentistry*, vol. 97, pp. 141–149, Mar. 2007.

[28] GC Corporation, *Initial Ti - Technical manual*, 2020. Available at https://europe.gc.dental/sites/europe.gc.dental/files/products/downloads/initialti/manual/MAN_Initial_Ti_en.pdf.

[29] P. Haag and K. Nilner, "Bonding between titanium and dental porcelain: A systematic review," *Acta Odontologica Scandinavica*, vol. 68, pp. 154–164, May 2010.

[30] M. S. Gunstad, "Development of piezoelectric composite ceramic coatings on metal substrates for biomedical application - project work," 2022.

[31] S. C. Moldoveanu and V. David, "Chapter 7 - rp-hplc analytical columns," in *Selection of the HPLC Method in Chemical Analysis* (S. C. Moldoveanu and V. David, eds.), pp. 279–328, Elsevier, 2017.

[32] E. Bernardo and G. Scarinci, "Sintering behaviour and mechanical properties of Al2O3 platelet-reinforced glass matrix composites obtained by powder technology," *Ceramics International*, vol. 30, pp. 785–791, Jan. 2004.

[33] A. A. El-Kheshen and M. F. Zawrah, "Sinterability, microstructure and properties of glass/ceramic composites," *Ceramics International*, vol. 29, pp. 251–257, Jan. 2003.

[34] D. W. Richerson, "Modern ceramic engineering : properties, processing, and use in design," 2018.

[35] M. Antanasova and P. Jevnikar, "Bonding of Dental Ceramics to Titanium: Processing and Conditioning Aspects," *Current Oral Health Reports*, vol. 3, pp. 234–243, Sept. 2016.

[36] G. Miranda, F. Sousa, M. M. Costa, F. Bartolomeu, F. S. Silva, and O. Carvalho, "Surface design using laser technology for Ti6Al4V-hydroxyapatite implants," *Optics & Laser Technology*, vol. 109, pp. 488–495, Jan. 2019.

[37] I. Abrahamsson and G. Cardaropoli, "Peri-implant hard and soft tissue integration to dental implants made of titanium and gold," *Clinical Oral Implants Research*, vol. 18, no. 3, pp. 269–274, 2007.

[38] A. Insua, A. Monje, H.-L. Wang, and R. J. Miron, "Basis of bone metabolism around dental implants during osseointegration and peri-implant bone loss," *Journal of Biomedical Materials Research Part A*, vol. 105, no. 7, pp. 2075–2089, 2017.

[39] M. A. De Maeztu, J. I. Alava, and C. Gay-Escoda, "Ion implantation: surface treatment for improving the bone integration of titanium and Ti6Al4V dental implants," *Clinical Oral Implants Research*, vol. 14, no. 1, pp. 57–62, 2003.

[40] R. J. Tilley, "Understanding solids : the science of materials," 2013.

[41] M. Acosta, N. Novak, V. Rojas, S. Patel, R. Vaish, J. Koruza, G. A. Rossetti, and J. Rödel, "BaTiO $_3$ -based piezoelectrics: Fundamentals, current status, and perspectives," *Applied Physics Reviews*, vol. 4, no. 4, p. 041305, 2017.

[42] B. Jaffe, "Piezoelectric ceramics," 1971.

[43] D. W. Richerson, *The Magic of Ceramics*. The American Ceramic Society, 2000.

[44] W. D. Callister, "Materials science and engineering," 2015.

[45] P. Dineva, D. Gross, R. Müller, and T. Rangelov, "Piezoelectric Materials," in *Dynamic Fracture of Piezoelectric Materials: Solution of Time-Harmonic Problems via BIEM* (P. Dineva, D. Gross, R. Müller, and T. Rangelov, eds.), Solid Mechanics and Its Applications, pp. 7–32, Cham: Springer International Publishing, 2014.

[46] A. H. Rajabi, M. Jaffe, and T. L. Arinzeh, "Piezoelectric materials for tissue regeneration: A review," *Acta Biomaterialia*, vol. 24, pp. 12–23, 2015.

[47] A. L. Kholkin, N. A. Pertsev, and A. V. Goltsev, "Piezoelectricity and Crystal Symmetry," in *Piezoelectric and Acoustic Materials for Transducer Applications* (A. Safari and E. K. Akdoğan, eds.), pp. 17–38, Boston, MA: Springer US, 2008.

[48] X. Zhu, *Piezoelectric Ceramic Materials: Processing, Properties, Characterization, and Applications*. Nova Science Publishers, Incorporated, 2010.

[49] L. Jin, F. Li, and S. Zhang, "Decoding the Fingerprint of Ferroelectric Loops: Comprehension of the Material Properties and Structures," *Journal of the American Ceramic Society*, vol. 97, no. 1, pp. 1–27, 2014. _eprint: https://onlinelibrary.wiley.com/doi/pdf/10.1111/jace.12773.

[50] Y. Zhang, J. Glaum, C. Groh, M. C. Ehmke, J. E. Blendell, K. J. Bowman, and M. J. Hoffman, "Correlation Between Piezoelectric Properties and Phase Coexistence in (Ba,Ca)(Ti,Zr)O3 Ceramics," *Journal of the American Ceramic Society*, vol. 97, no. 9, pp. 2885–2891, 2014. _eprint: https://onlinelibrary.wiley.com/doi/pdf/10.1111/jace.13047.

[51] Y. Zhang, J. Roscow, R. Lewis, H. Khanbareh, V. Y. Topolov, M. Xie, and C. R. Bowen, "Understanding the effect of porosity on the polarisation-field response of ferroelectric materials," *Acta Materialia*, vol. 154, pp. 100–112, Aug. 2018.

[52] E. W. Yap, J. Glaum, J. Oddershede, and J. E. Daniels, "Effect of porosity on the ferroelectric and piezoelectric properties of (Ba0.85Ca0.15)(Zr0.1Ti0.9)O3 piezoelectric ceramics," *Scripta Materialia*, vol. 145, pp. 122–125, Mar. 2018.

[53] J. I. Roscow, Y. Zhang, M. J. Kraśny, R. W. C. Lewis, J. Taylor, and C. R. Bowen, "Freeze cast porous barium titanate for enhanced piezoelectric energy harvesting," *Journal of Physics D: Applied Physics*, vol. 51, p. 225301, May 2018. Publisher: IOP Publishing.

[54] J. I. Roscow, V. Y. Topolov, C. R. Bowen, J. Taylor, and A. E. Panich, "Understanding the peculiarities of the piezoelectric effect in macro-porous BaTiO $_3$," *Science and Technology of Advanced Materials*, vol. 17, pp. 769–776, Jan. 2016.

[55] C. Padurariu, L. Padurariu, L. Curecheriu, C. Ciomaga, N. Horchidan, C. Galassi, and L. Mitoseriu, "Role of the pore interconnectivity on the dielectric, switching and tunability properties of PZTN ceramics," *Ceramics International*, vol. 43, pp. 5767–5773, May 2017.

[56] M. Tavangar, F. Heidari, R. Hayati, F. Tabatabaei, D. Vashaee, and L. Tayebi, "Manufacturing and characterization of mechanical, biological and dielectric properties of hydroxyapatite-barium titanate nanocomposite scaffolds," *Ceramics International*, vol. 46, pp. 9086–9095, May 2020.

[57] A. F. L. Almeida, P. B. A. Fechine, J. M. Sasaki, A. P. Ayala, J. C. Góes, D. L. Pontes, W. Margulis, and A. S. B. Sombra, "Optical and electrical properties of barium titanate-hydroxyapatite composite screen-printed thick films," *Solid State Sciences*, vol. 6, no. 3, pp. 267–278, 2004.

[58] M. Prakasam, M. Albino, E. Lebraud, M. Maglione, C. Elissalde, and A. Largeteau, "Hydroxyapatite-barium titanate piezocomposites with enhanced electrical properties," *Journal of the American Ceramic Society*, vol. 100, no. 6, pp. 2621–2631, 2017.

[59] Y. Wang, J. Cui, L. Wang, Q. Yuan, Y. Niu, J. Chen, Q. Wang, and H. Wang, "Compositional tailoring effect on electric field distribution for significantly enhanced breakdown strength and restrained conductive loss in sandwich-structured ceramic/polymer nanocomposites," *Journal of Materials Chemistry A*, vol. 5, pp. 4710–4718, Feb. 2017. Publisher: The Royal Society of Chemistry.

[60] L. Bolzoni, "Structural electroactive cermets: dielectric and structural properties of conductive metallic reinforced piezoelectric ceramics," *Critical Reviews in Solid State and Materials Sciences*, vol. 46, pp. 38–81, Jan. 2021. Publisher: Taylor & Francis.

[61] I. Coondoo, N. Panwar, D. Alikin, I. Bdikin, S. S. Islam, A. Turygin, V. Y. Shur, and A. L. Kholkin, "A comparative study of structural and electrical properties in lead-free BCZT ceramics: Influence of the synthesis method," *Acta Materialia*, vol. 155, pp. 331–342, Aug. 2018.

[62] Y. Tian, X. Chao, L. Wei, P. Liang, and Z. Yang, "Phase transition behavior and electrical properties of lead-free (Ba1xCax)(Zr0.1Ti0.9)O3 piezoelectric ceramics," *Journal of Applied Physics*, vol. 113, p. 184107, May 2013. Publisher: American Institute of Physics.

[63] M. M. Vijatović, J. D. Bobić, and B. D. Stojanović, "History and challenges of barium titanate: Part I," *Science of Sintering*, vol. 40, no. 2, pp. 155–165, 2008.

[64] S. Korkmaz and I. A. Kariper, "BaTiO3-based nanogenerators: fundamentals and current status," *Journal of Electroceramics*, Nov. 2021.

[65] V. Madhu Babu, J. Paul Praveen, and D. Das, "Synthesis and aging behaviour study of lead-free piezoelectric bczt ceramics," *Chemical Physics Letters*, vol. 772, p. 138560, 2021.

[66] A. R. West, "Solid state chemistry and its applications," 2014.

[67] University of Cambridge, "Barium titanate and phase changes." Available at https://www.doitpoms.ac.uk/tlplib/ferroelectrics/phase_changes.php.

[68] Y. Tian, S. Li, Y. Li, Y. Gong, X. Ji, S. Sun, and Q. Jing, "Diversiform electrical and thermal expansion properties of (1-x)ba0.95ca0.05ti0.94zr0.06o3–(x)dy lead-free piezoelectric ceramics influenced by defect complexes," *Journal of materials science*, vol. 53, no. 16, pp. 11228–11241, 2018.

[69] J. Wu, "BaTiO3-Based Piezoelectric Materials," in *Advances in Lead-Free Piezoelectric Materials* (J. Wu, ed.), pp. 247–299, Singapore: Springer, 2018.

[70] N. Pisitpipathsin, P. Kantha, S. Eitsayeam, G. Rujijanakul, R. Guo, A. S. Bhalla, and K. Pengpat, "Effect of BCZT on Electrical Properties and Bioactivity of 45S5 Bioglass," *Integrated Ferroelectrics*, vol. 142, pp. 144–153, Jan. 2013. Publisher: Taylor & Francis, _eprint: https://doi.org/10.1080/10584587.2013.780574.

[71] C. N. Elias, J. H. C. Lima, R. Valiev, and M. A. Meyers, "Biomedical applications of titanium and its alloys," *JOM (1989)*, vol. 60, no. 3, pp. 46–49, 2008.

[72] M. Özcan and C. Hämmerle, "Titanium as a Reconstruction and Implant Material in Dentistry: Advantages and Pitfalls," *Materials*, vol. 5, pp. 1528–1545, Aug. 2012.

[73] S. Kuroda, J. Kawakita, M. Watanabe, K. Kim, R. Molak, and H. Katanoda, "7 - current status and future prospects of warm spray technology," in *Future Development of Thermal Spray Coatings* (N. Espallargas, ed.), pp. 163–206, Woodhead Publishing, 2015.

[74] M. Niinomi, "Recent metallic materials for biomedical applications," *Metallurgical and Materials Transactions A*, vol. 33, no. 3, pp. 477–486, 2002.

[75] K. Prasad, O. Bazaka, M. Chua, M. Rochford, L. Fedrick, J. Spoor, R. Symes, M. Tieppo, C. Collins, A. Cao, D. Markwell, K. K. Ostrikov, and K. Bazaka, "Metallic biomaterials: Current challenges and opportunities," *Materials*, vol. 10, no. 8, 2017.

[76] AZo Materials, "Titanium alloys - ti6al4v grade 5," 2002. Available at https://www.azom.com/article.aspx?ArticleID=1547.

[77] R. Gaddam, B. Sefer, R. Pederson, and M.-L. Antti, "Study of alpha-case depth in ti-6al-2sn-4zr-2mo and ti-6al-4v," *IOP Conference Series: Materials Science and Engineering*, vol. 48, p. 012002, dec 2013.

[78] T. Lutz, J. Gerlach, and S. Mändl, "Diffusion, phase formation and segregation effects in ti6al4v after oxygen piii," *Surface and Coatings Technology*, vol. 201, no. 15, pp. 6690–6694, 2007. The Eighth International Workshop on Plasma-Based Ion Implantation and Deposition.

[79] G. M. Rodriguez, J. Bowen, M. Zelzer, and A. Stamboulis, "Selective modification of ti6al4v surfaces for biomedical applications," *RSC advances*, vol. 10, no. 30, pp. 17642–17652, 2020.

[80] "ISO 9693:2019 - Dentistry - Compatibility testing or metal-ceramic and ceramic-ceramic systems," standard, International Organization for Standardization, Geneva, CH, 2019.

[81] J. Bieniaś, B. Surowska, A. Stoch, H. Matraszek, and M. Walczak, "The influence of SiO2 and SiO2–TiO2 intermediate coatings on bond strength of titanium and Ti6Al4V alloy to dental porcelain," *Dental Materials*, vol. 25, pp. 1128–1135, Sept. 2009.

[82] S. Zinelis, X. Barmpagadaki, V. Vergos, M. Chakmakchi, and G. Eliades, "Bond strength and interfacial characterization of eight low fusing porcelains to cp Ti," *Dental Materials*, vol. 26, pp. 264–273, Mar. 2010.

[83] M. A. Aslan, C. Ural, and S. Arici, "Investigation of the effect of titanium alloy surface coating with different techniques on titanium-porcelain bonding," *The Journal of Prosthetic Dentistry*, vol. 115, pp. 115–122, Jan. 2016.

[84] S. S. Scherrer, U. Lohbauer, A. D. Bona, A. Vichi, M. J. Tholey, J. R. Kelly, R. v. Noort, and P. F. Cesar, "ADM guidance—Ceramics: guidance to the use of fractography in failure analysis of brittle materials," *Dental Materials*, vol. 33, no. 6, pp. 599–620, 2017.

[85] S. Nasrazadani and S. Hassani, "Chapter 2 - Modern analytical techniques in failure analysis of aerospace, chemical, and oil and gas industries," in *Handbook of Materials Failure Analysis with Case Studies from the Oil and Gas Industry* (A. S. H. Makhlouf and M. Aliofkhazraei, eds.), pp. 39–54, Butterworth-Heinemann, Jan. 2016.

[86] Y. Harada and Y. Ikuhara, "Chapter 1.1.1 - the latest analytical electron microscope and its application to ceramics," in *Handbook of Advanced Ceramics (Second Edition)* (S. Somiya, ed.), pp. 3–21, Academic Press, second edition ed., 2013.

[87] JEOL Ltd., "Energy table for EDS analysis." Available at https://www.unamur.be/services/microscopie/sme-documents/Energy-20table-20for-20EDS-20analysis-1.pdf.

[88] N. Kazantseva, P. Krakhmalev, I. Yadroitsev, A. Fefelov, A. Merkushev, M. Ilyinikh, N. Vinogradova, I. Ezhov, and T. Kurennykh, "Oxygen and nitrogen concentrations in the Ti-6Al-4V alloy manufactured by direct metal laser sintering (DMLS) process," *Materials Letters*, vol. 209, pp. 311–314, 2017.

Appendices

A Tables

In Table A.1 the weight and diameter before and after calcination of the pellets in the solid state synthesis of BCZT are given. α, β, and γ refers to the name of the powder batch.

Table A.1: Here all calcined pellets are listed with ID, weight before and after calcination (*bc* and *ac*), as well as diameter before and after calcination. A "-" is stated as the diameter after calcination when the pellet was broken after calcination.

Pellet ID	$\mathbf{m}_{bc}$ **[g]**	$\mathbf{D}_{bc}$ **[mm]**	$\mathbf{m}_{ac}$ **[g]**	$\mathbf{D}_{ac}$ **[mm]**
α-1	0.9870	25	0.7041	22.86
α-2	1.1111	25	0.8126	22.94
α-3	1.0181	25	0.8441	22.91
α-4	0.8548	25	0.8387	22.98
α-5	0.8525	25	0.7989	22.78
α-6	1.0462	25	0.8605	23.06
α-7	0.9694	25	0.7026	23.03
α-8	0.9749	25	0.7985	-
β-1	0.9445	25	0.7714	23.42
β-2	0.9490	25	0.7156	22.90
β-3	0.9338	25	0.7594	23.22
β-4	0.9367	25	0.7640	23.11
β-5	0.9185	25	0.7642	22.96
β-6	0.9255	25	0.7558	22.80
β-7	0.9384	25	0.7505	22.85
β-8	0.9117	25	0.7541	23.05
β-9	0.9185	25	0.7450	22.92
β-10	0.9295	25	0.7608	22.93
γ-1	0.9183	25	0.7481	17.53
γ-2	0.9159	25	0.7427	16.24
γ-3	0.9200	25	0.7542	16.00
γ-4	0.9035	25	0.7445	16.01
γ-5	0.9191	25	0.7467	15.53
γ-6	0.9048	25	0.7467	16.39
γ-7	0.9104	25	0.7426	16.10
γ-8	0.9072	25	0.7455	16.49
γ-9	0.9106	25	0.7418	16.49
γ-10	0.9018	25	0.7539	-

The β-BCZT powder was recalcined as a loose powder to achieve the correct composition. The recalcination was done twice, and in each recalcination the powder was divided into two platinum crucibles. The weight of the powder in each crucible

before and after recalcination are given in Table A.2. In the ID-column the 1 and 2 refers to first and second recalcination while A and B refers to the two crucibles.

Table A.2: Weight of β-BCZT powder before and after recalcination.

ID	$\mathbf{m}_{bc}$ [g]	$\mathbf{m}_{ac}$ [g]
β-1A	3.9110	3.7966
β-1B	3.0850	3.0069
β-2A	3.3505	3.3435
β-2B	3.0661	3.0570

As a part of the solid state synthesis 3 pellets of γ-BCZT powder was pressed and sintered. The weight, diameter and thickness of each pellet was recorded before and after sintering. These values are listed in Table A.3.

Table A.3: Dimensions of sintered pellets before and after sintering. Here the pellet ID, mass, diameter and thickness before sintering (bs), as well as mass, diameter and thickness after sintering (as) are listed.

Pellet ID	$\mathbf{m_{bs}}$ [g]	$\mathbf{D_{bs}}$ [mm]	$\mathbf{t_{bs}}$ [mm]	$\mathbf{m_{as}}$ [g]	$\mathbf{D_{as}}$ [mm]	$\mathbf{t_{as}}$ [mm]
Pγ-1	0.5068	10	2.37	0.4966	8.19	2.03
Pγ-2	0.5045	10	2.43	0.4988	8.22	2.07
Pγ-3	0.5017	10	2.26	0.4922	8.24	1.99

The density of the three pellets were measured using Archimedes' method. This method requires the mass of the dry pellet (m_1), mass of the pellet submerged in isopropanol (m_2), the weight of the wet pellet (m_3) and the temperature of the isopropanol. These values are listed for each of the pellets in Table A.4 below.

Table A.4: Here the pellet ID along with the weight of the dry pellet, the pellet submerged in isopropanol, and the wet pellet are listed. The temperature of the isopropanol was also recorded.

Pellet ID	$\mathbf{m}_1$ [g]	$\mathbf{m}_2$ [g]	$\mathbf{m}_3$ [g]	$\mathbf{T_{liq}}$ [°C]
Pγ-1	0.4966	0.4169	0.5035	19.5
Pγ-2	0.4988	0.4286	0.5072	20
Pγ-3	0.4922	0.4227	0.4999	20

In Table A.5 the thickness (D) of the metal substrate, of the bonder layer, and of the dentine layer are listed together with the sample ID, total sample thickness and the width of each sample. Each value is given with its standard deviation as the thickness was measured in three points. For some samples the thickness of the bonder layer is recorded as "-". This is because by mistake the thickness was not measured. When "-" is listed as the dentine thickness, total thickness or width the coating broke during the polishing and the dimensions were not measured.

Table A.5: Overview of all coating samples used in the project, together with the thickness of the substrate and the bonder layer, the total sample thickness and the width. The standard deviation of each thickness is also given.

ID	D_{metal} [mm]	D_{bonder} [mm]	D_{total} [mm]	Width [mm]
D-00-1	0.489 ± 0.006	0.033 ± 0.011	1.542 ± 0.029	3.000 ± 0.012
D-00-2	0.488 ± 0.005	0.048 ± 0.025	1.505 ± 0.010	2.992 ± 0.012
D-00-3	0.491 ± 0.002	0.058 ± 0.012	1.490 ± 0.027	3.027 ± 0.007
D-00-4	0.504 ± 0.002	0.014 ± 0.005	1.484 ± 0.017	3.049 ± 0.028
D-00-5	0.491 ± 0.004	0.036 ± 0.006	1.446 ± 0.010	3.019 ± 0.004
D-00-6	0.493 ± 0.004	0.043 ± 0.002	1.499 ± 0.014	2.994 ± 0.001
D-00-7	0.482 ± 0.003	0.026 ± 0.006	-	3.026 ± 0.015
D-00-8	0.500 ± 0.004	0.064 ± 0.026	1.463 ± 0.029	2.996 ± 0.003
D-00-9	0.496 ± 0.005	0.048 ± 0.007	1.475 ± 0.026	3.027 ± 0.010
D-00-10	0.492 ± 0.002	0.071 ± 0.018	-	3.034 ± 0.013
D-00-11	0.494 ± 0.003	0.020 ± 0.009	1.456 ± 0.030	3.038 ± 0.010
D-00-12	0.492 ± 0.002	0.027 ± 0.002	-	-
D-00-13	0.488 ± 0.003	0.027 ± 0.006	1.472 ± 0.012	2.958 ± 0.018
D-00-14	0.492 ± 0.004	0.027 ± 0.008	-	-
D-00-15	0.497 ± 0.005	0.038 ± 0.004	1.514 ± 0.006	2.952 ± 0.002
D-00-16	0.495 ± 0.003	0.035 ± 0.008	1.490 ± 0.012	2.973 ± 0.005
D-00-17	0.498 ± 0.004	0.023 ± 0.003	-	-
D-00-18	0.477 ± 0.004	0.035 ± 0.005	1.500 ± 0.004	2.999 ± 0.014
Dγ-30-1	0.499 ± 0.002	-	1.507 ± 0.004	2.994 ± 0.023
Dγ-30-2	0.487 ± 0.002	-	1.492 ± 0.020	2.943 ± 0.020
Dγ-30-3	0.493 ± 0.002	-	1.528 ± 0.018	3.016 ± 0.023
Dγ-30-4	0.495 ± 0.004	-	1.461 ± 0.020	2.982 ± 0.011
Dγ-30-5	0.494 ± 0.004	-	1.509 ± 0.006	3.013 ± 0.030
Dγ-30-6	0.501 ± 0.003	-	1.509 ± 0.006	3.013 ± 0.030
Dγ-30-7	0.500 ± 0.007	-	-	-
Dγ-30-8	0.490 ± 0.003	-	-	-
Dγ-30-9	0.496 ± 0.007	-	1.501 ± 0.021	3.038 ± 0.024
Dγ-30-10	0.510 ± 0.003	-	1.473 ± 0.012	2.995 ± 0.038
Dγ-30-11	0.492 ± 0.004	0.020 ± 0.002	1.489 ± 0.009	2.985 ± 0.028
Dγ-30-12	0.492 ± 0.007	0.020 ± 0.001	-	-
Dγ-30-13	0.483 ± 0.003	0.023 ± 0.005	-	-
Dγ-30-14	0.487 ± 0.005	0.034 ± 0.006	1.513 ± 0.003	3.379 ± 0.578
Dγ-30-15	0.480 ± 0.004	0.019 ± 0.002	1.515 ± 0.004	2.992 ± 0.024
Dγ-30-16	0.489 ± 0.005	0.017 ± 0.001	1.496 ± 0.003	3.016 ± 0.032
Dγ-40-1	0.495 ± 0.004	0.034 ± 0.005	1.506 ± 0.007	2.996 ± 0.006
Dγ-40-2	0.490 ± 0.005	0.037 ± 0.009	1.514 ± 0.008	3.013 ± 0.016
Dγ-40-3	0.472 ± 0.011	0.031 ± 0.007	1.500 ± 0.006	3.009 ± 0.010
Dγ-40-4	0.495 ± 0.002	0.028 ± 0.002	1.495 ± 0.005	3.028 ± 0.009
Dγ-40-5	0.490 ± 0.005	0.024 ± 0.002	1.448 ± 0.024	3.024 ± 0.002
Dγ-40-6	0.487 ± 0.005	0.024 ± 0.007	1.486 ± 0.015	3.036 ± 0.007

Continued on next page

Table A.5 *continued from previous page*

ID	D_{metal} [mm]	D_{bonder} [mm]	D_{total} [mm]	Width [mm]
Dγ-40-7	0.496 ± 0.002	0.038 ± 0.003	1.478 ± 0.033	3.005 ± 0.006
Dγ-40-8	0.491 ± 0.007	0.022 ± 0.009	1.499 ± 0.003	3.029 ± 0.013
Dγ-40-9	0.493 ± 0.001	0.022 ± 0.008	1.493 ± 0.005	3.039 ± 0.015
Dγ-40-10	0.501 ± 0.002	0.021 ± 0.007	1.487 ± 0.003	3.054 ± 0.016
Dγ-40-11	0.500 ± 0.002	0.025 ± 0.004	1.504 ± 0.004	3.008 ± 0.016
Dγ-40-12	0.494 ± 0.003	0.025 ± 0.008	-	-
Dγ-40-13	0.497 ± 0.005	0.025 ± 0.001	-	-
Dγ-50-1	0.496 ± 0.005	0.018 ± 0.002	1.471 ± 0.010	3.013 ± 0.004
Dγ-50-2	0.501 ± 0.005	0.031 ± 0.008	1.471 ± 0.025	3.025 ± 0.012
Dγ-50-3	0.486 ± 0.005	0.031 ± 0.018	1.443 ± 0.022	3.040 ± 0.006
Dγ-50-4	0.489 ± 0.006	0.025 ± 0.006	1.486 ± 0.020	3.038 ± 0.012
Dγ-50-5	0.487 ± 0.006	0.20 ± 0.005	1.473 ± 0.024	2.996 ± 0.000
Dγ-50-6	0.501 ± 0.007	-0.004 ± 0.057	1.406 ± 0.011	2.964 ± 0.005
Dγ-50-7	0.491 ± 0.006	0.045 ± 0.010	1.394 ± 0.030	3.012 ± 0.003
Dγ-50-8	0.489 ± 0.002	0.027 ± 0.004	1.468 ± 0.019	3.012 ± 0.009
Dγ-50-9	0.491 ± 0.002	0.026 ± 0.003	1.501 ± 0.008	3.045 ± 0.006
Dγ-50-10	0.469 ± 0.008	0.021 ± 0.007	1.474 ± 0.030	3.009 ± 0.004
Dβ-30-1	0.471 ± 0.002	-	1.485 ± 0.007	3.075 ± 0.016
Dβ-30-2	0.483 ± 0.002	-	1.503 ± 0.005	2.995 ± 0.046
Dβ-30-3	0.484 ± 0.003	-	1.503 ± 0.006	2.997 ± 0.022
Dβ-30-4	0.487 ± 0.002	0.021 ± 0.004	1.500 ± 0.001	3.018 ± 0.033
Dβ-30-5	0.500 ± 0.005	0.023 ± 0.010	1.503 ± 0.003	3.025 ± 0.004
Dβ-30-6	0.486 ± 0.005	0.071 ± 0.038	1.502 ± 0.003	2.967 ± 0.009
Dβ-30-7	0.485 ± 0.002	0.012 ± 0.004	1.507 ± 0.003	3.009 ± 0.001
Dβ-30-8	0.493 ± 0.005	0.021 ± 0.006	-	-
Dβ-30-9	0.497 ± 0.008	0.018 ± 0.002	-	-
Dβ-30-10	0.500 ± 0.004	0.033 ± 0.005	-	-
Dβ-30-11	0.489 ± 0.008	0.011 ± 0.001	1.483 ± 0.014	3.039 ± 0.007
Dβ-30-12	0.501 ± 0.001	0.011 ± 0.004	-	-
Dβ-30-13	0.484 ± 0.005	0.019 ± 0.011	1.491 ± 0.009	2.952 ± 0.029
Dβ-30-14	0.491 ± 0.004	0.033 ± 0.014	1.512 ± 0.003	3.006 ± 0.002
Dβ-30-15	0.479 ± 0.000	0.025 ± 0.003	-	-
Dβ-30-16	0.480 ± 0.003	0.030 ± 0.002	-	-
Dβ-30-17	0.501 ± 0.001	0.019 ± 0.002	1.512 ± 0.003	2.956 ± 0.006
Dβ-40-1	0.503 ± 0.003	0.009 ± 0.001	1.508 ± 0.005	3.026 ± 0.024
Dβ-40-2	0.488 ± 0.010	0.019 ± 0.015	1.503 ± 0.007	3.015 ± 0.037
Dβ-40-3	0.487 ± 0.000	0.015 ± 0.002	1.495 ± 0.009	3.011 ± 0.058
Dβ-40-4	0.485 ± 0.001	0.032 ± 0.014	1.504 ± 0.003	3.030 ± 0.027
Dβ-40-5	0.486 ± 0.004	0.019 ± 0.006	1.496 ± 0.016	3.036 ± 0.019
Dβ-40-6	0.482 ± 0.002	0.028 ± 0.008	1.488 ± 0.012	3.014 ± 0.009
Dβ-40-7	0.500 ± 0.005	0.029 ± 0.010	1.506 ± 0.006	3.000 ± 0.005
Dβ-40-8	0.486 ± 0.004	0.023 ± 0.009	-	-

Continued on next page

Table A.5 *continued from previous page*

ID	$\mathbf{D_{metal}}$ **[mm]**	$\mathbf{D_{bonder}}$ **[mm]**	$\mathbf{D_{total}}$ **[mm]**	**Width [mm]**
Dβ-40-9	0.501 ± 0.003	0.012 ± 0.002	1.507 ± 0.008	3.022 ± 0.010
Dβ-40-10	0.495 ± 0.002	0.024 ± 0.005	1.504 ± 0.007	3.027 ± 0.001
Dβ-40-11	0.498 ± 0.004	0.033 ± 0.005	1.498 ± 0.002	3.022 ± 0.020
Dβ-40-12	0.484 ± 0.006	0.041 ± 0.015	1.501 ± 0.011	3.011 ± 0.041
Dβ-50-1	0.484 ± 0.001	0.021 ± 0.002	1.501 ± 0.004	2.959 ± 0.006
Dβ-50-2	0.486 ± 0.002	0.019 ± 0.003	1.500 ± 0.009	2.991 ± 0.006
Dβ-50-3	0.494 ± 0.003	0.026 ± 0.001	1.507 ± 0.003	2.971 ± 0.029
Dβ-50-4	0.498 ± 0.003	0.031 ± 0.002	1.507 ± 0.003	2.990 ± 0.021
Dβ-50-5	0.494 ± 0.003	0.024 ± 0.001	1.501 ± 0.002	2.996 ± 0.011
Dβ-50-6	0.505 ± 0.004	0.030 ± 0.004	1.502 ± 0.012	2.993 ± 0.026
Dβ-50-7	0.499 ± 0.005	0.034 ± 0.003	1.489 ± 0.011	2.980 ± 0.003
Dβ-50-8	0.486 ± 0.001	0.029 ± 0.004	-	-
Dβ-50-9	0.496 ± 0.003	0.026 ± 0.007	1.497 ± 0.011	2.951 ± 0.016
Dβ-50-10	0.479 ± 0.004	0.026 ± 0.007	1.496 ± 0.006	2.977 ± 0.017
Dβ-50-11	0.489 ± 0.005	0.030 ± 0.004	1.504 ± 0.005	2.967 ± 0.025
Dβ-50-12	0.489 ± 0.003	0.025 ± 0.005	1.503 ± 0.008	2.994 ± 0.005

B Calculations

B.1 Precursor Amounts

The aim of the solid state synthesis of BCZT was to obtain a powder with the following composition: $(Ba_{0.85}Ca_{0.15})(Zr_{0.1}Ti_{0.9})O_3$. It was therefore necessary to calculate the needed amount of each precursor. The molar mass of the precursors and the final composition are given in Table B.1. Here an example calculation where the aim was 12 g of BCZT is shown.

Table B.1: Molar mass of the precursors and the wanted composition.

Compound	***M*** **[g/mol]**
$BaCO_3$	197.34
$CaCO_3$	100.09
ZrO_2	123.22
TiO_2	79.87
$(Ba_{0.85}Ca_{0.15})(Zr_{0.1}Ti_{0.9})O_3$	222.94

First it is necessary to calculate the number of moles that 12 g of BCZT constitutes,

$$n_{\mathrm{BCZT}} = \frac{\mathrm{m}}{M} = \frac{12}{222.94} = 0.0538\mathrm{mol} \tag{B.1}$$

where m is the mass and M is the molar mass. Based on this and the final composition it is possible to calculate the needed moles and mass of each precursor. The calculation of needed $BaCO_3$ is shown in Equation B.2 and Equation B.3, the same method applies to the remaining precursors. First the moles of $BaCO_3$, $\mathrm{n}_{\mathrm{BaCO_3}}$, is calculated using the result from Equation B.1 and that 85% of the cations in the final composition should be Ba.

$$n_{\mathrm{BaCO_3}} = 0.85 \cdot n_{\mathrm{BCZT}} = 0.85 \cdot 0.0538\mathrm{mol} = 0.0458\mathrm{mol} \tag{B.2}$$

Then the mass of $BaCO_3$ can be calculated as shown in Equation B.3,

$$m_{\mathrm{BaCO_3}} = n_{\mathrm{BaCO_3}} \cdot M_{\mathrm{BaCO_3}} = 0.0458\mathrm{mol} \cdot 197.34\mathrm{g/mol} = 9.0305\,\mathrm{g} \tag{B.3}$$

The same calculations can then be done for the other three precursors. The results of these calculations are given in Table B.2.

B.2 Final Composition of BCZT Powders

The final composition of the BCZT powders has been calculated based on the precursor amounts. The actual mass that was used of each precursor for the synthesis

Table B.2: Calculated moles and mass of the precursors.

Compound	n **[mol]**	**m [g]**
$BaCO_3$	0.0458	9.0305
$CaCO_3$	0.0081	0.8163
ZrO_2	0.0054	0.6634
TiO_2	0.0484	3.8769

are listed in Table B.3 together with the moles, and the resulting percentages each ion makes up in the final product. Since the calculations are the same for each precursor, an example calculation of $BaCO_3$ in the γ-BCZT powder is shown in the following equations. First the used moles of $BaCO_3$ is calculated based on the molar mass and the used mass of $BaCO_3$,

$$n_{\mathrm{BaCO_3}} = \frac{m_{\mathrm{BaCO_3}}}{M_{\mathrm{BaCO_3}}} = \frac{8.9572}{197.34} = 0.0454\mathrm{mol} \tag{B.4}$$

The same calculation for $CaCO_3$ for the γ-BCZT powder results in $n_{\mathrm{CaCO_3}} = 0.0081\mathrm{mol}$. The Ba-ions and Ca-ions add up to 100% of the cations, thus the ratio of the two cations can be calculated using the moles of each cation. First the total moles of cations is calculated,

$$n_{\mathrm{cations}} = n_{\mathrm{BaCO_3}} + n_{\mathrm{CaCO_3}} = 0.0454\mathrm{mol} + 0.0081\mathrm{mol} = 0.0535\mathrm{mol} \tag{B.5}$$

Then the ratio of the cations can be calculated, here the calculation for fraction of $BaCO_3$, $f_{\mathrm{BaCO_3}}$ is shown.

$$f_{\mathrm{BaCO_3}} = \frac{n_{\mathrm{BaCO_3}}}{n_{\mathrm{cations}}} = \frac{0.0454}{0.0535} = 0.8479 \tag{B.6}$$

The same method has been applied to all 4 precursors for both the β-BCZT and the γ-BCZT powder. The results are listed in Table B.3. This shows that the β-BCZT powder has the following composition: $(Ba_{0.8487}Ca_{0.1513})(Zr_{0.0999}Ti_{0.9001})O_3$ and the γ-BCZT has this composition: $(Ba_{0.8479}Ca_{0.1521})(Zr_{0.1}Ti_{0.9})O_3$

Table B.3: List of all used precursors, the mass used and calculated moles used for each powder. The fraction of each precursor in each of the BCZT powders is also listed.

Compound	$\mathbf{m}_\beta$ **[g]**	$\boldsymbol{n}_\beta$ **[mol]**	**X,**β **[-]**	$\mathbf{m}_\gamma$ **[g]**	$\boldsymbol{n}_\gamma$ **[mol]**	**X,**γ **[-]**
$BaCO_3$	7.4697	0.0379	0.8487	8.9572	0.0454	0.8479
$CaCO_3$	0.6755	0.0067	0.1513	0.8150	0.0081	0.1521
ZrO_2	0.5492	0.0045	0.0999	0.6643	0.0054	0.1000
TiO_2	3.2069	0.0402	0.9001	3.8769	0.0485	0.900

B.3 Force for Pressing Pellets - Conversion from MPa to kN

Pellets were pressed for both calcination and sintering in the solid state synthesis of BCZT. In both cases the pellets were pressed using a force of 10 MPa, however the digital reader connected to the uniaxial press only showed force in kN. Therefore the force had to be converted from MPa to kN. The pellets prepared for calcination had a diameter of 25 mm while the pellets for sintering had a diameter of 10 mm. The conversions for both these sizes are shown in Equation B.7 and Equation B.8, respectively.

$$F = \frac{\pi D^2[\text{mm}] \cdot \text{MPa}}{4000} = \frac{\pi \cdot 25^2 \cdot 10}{4000} = 4.9087\,\text{kN} \tag{B.7}$$

$$F = \frac{\pi D^2[\text{mm}] \cdot \text{MPa}}{4000} = \frac{\pi \cdot 10^2 \cdot 10}{4000} = 0.79\,\text{kN} \tag{B.8}$$

B.4 Density and Porosity of Pellets

The densities and porosities of the BCZT pellets were measured geometrically and using Archimedes' method. The theoretical density is based on the mass and the volume of the pellet, and is calculated as

$$\rho_t = \frac{m}{V} \tag{B.9}$$

, where m is the mass and V is the volume. The volume of of the pellet is calculated as

$$V = \pi \cdot r^2 \cdot h = \pi \cdot \left(\frac{d}{2}\right)^2 \cdot h \tag{B.10}$$

For pellet Pγ-1 the apparent density is

$$\rho_{a,1} = \frac{m}{\pi \cdot \left(\frac{d}{2}\right)^2 \cdot h} = \frac{0.4966\text{g}}{\pi \cdot \left(\frac{0.819\text{cm}}{2}\right)^2 \cdot 0.203\text{cm}} = 4.644\text{g/cm}^3 \tag{B.11}$$

The density of the immersion liquid, in this case isopropanol, needs to be calculated before the bulk density can be calculated. The density of the isopropanol can be found from the following correlation between density and temperature;

$$\rho_{liq} = -0.0009\text{T} + 0.80018 \tag{B.12}$$

where T [℃] is the temperature of the isopropanol. For T = 19.5 °C, the density is $\rho_{liq} = 0.7843\,\text{g/cm}^3$ The bulk density is calculated based on the weight of the dry

pellet (m_1), the pellet submerged in isopropanol (m_2), and the wet pellet (m_3) as well as the density of the isopropanol.

$$\rho_b = \frac{m_1}{m_3 - m_2} \cdot \rho_{liq} \tag{B.13}$$

The bulk density of Pγ-1 is then

$$\rho_{b,1} = \frac{0.4966\text{g}}{0.5035\text{g} - 0.4169\text{g}} \cdot 0.7843\,\text{g/cm}^3 = 4.497\,\text{g/cm}^3 \tag{B.14}$$

The apparent porosity, π_a is calculated from the three weight measurements of each pellet,

$$\pi_a = \frac{m_3 - m_1}{m_3 - m_1} \cdot 100 \tag{B.15}$$

The apparent porosity, also referred to as the open porosity, of Pγ-1 is

$$\pi_{a,1} = \frac{0.5035\,\text{g} - 0.4966\,\text{g}}{0.5035\,\text{g} - 0.4169\,\text{g}} \cdot 100 = 7.968\,\text{vol\%} \tag{B.16}$$

Finally, the true porosity, π_t is calculated from the theoretical and bulk density of the pellet. The true porosity is also known as the total porosity.

$$\pi_t = \frac{\rho_t - \rho_b}{\rho_t} \cdot 100 \tag{B.17}$$

The true porosity of Pγ-1 is then

$$\pi_{t_1} = \frac{5.57\,\text{g/cm}^3 - 4.497\,\text{g/cm}^3}{5.57\,\text{g/cm}^3} \cdot 100 = 19.26\,\text{vol\%} \tag{B.18}$$

Finally, the closed porosity (π_c) can be calculated based on the true and the apparent porosity.

$$\pi_c = \pi_t - \pi_a = 19.260\% - 7.968\% = 11.293\% \tag{B.19}$$

B.5 ISO 9693:2019 - De-bonding/Crack Initiation test

The bond strength of the coatings was measured in the de-bonding/crack initiation test as described in ISO 9693:2019. The *TestExpert III* software that was used to conduct these measurements measures the force and the deflection, in Newton and millimeter respectively. In order to get the bond strength in MPa it is therefore

necessary to calculate the bond strength from the fracture force, F_{fail} [N]. The ISO-standard lists two methods for this calculation, here the numerical calculation has been used. The main equation for this calculation is

$$\tau_b = k \cdot F_{\text{fail}} \tag{B.20}$$

, where τ_b is the bond strength, k is a coefficient and F_{fail} is the fracture force. The coefficient k is based on the Young's modulus E_Z [GPa] and the thickness d_Z [mm] of the metal substrate. k can be read of a graph but in the numerical calculation-method k is calculated for three thicknesses and for Young's modulus. From this one gets three coefficients k_1, k_2 and k_3. The general equation for these are given in the following three equations. k_1 is based on $d_{Z,1} = 0.44$ mm, k_2 is based on $d_{Z,2} = 0.5$ mm and k_3 is based on $d_{Z,3} = 0.56$ mm.

$$k(1) = 1.818 \cdot 10^{-5} \cdot E_Z^2 - 1.873 \cdot 10^{-2} \cdot E_Z + 7.802 \tag{B.21}$$

$$k(2) = 1.695 \cdot 10^{-5} \cdot E_Z^2 - 1.521 \cdot 10^{-2} \cdot E_Z + 6.131 \tag{B.22}$$

$$k(3) = 1.614 \cdot 10^{-5} \cdot E_Z^2 - 1.3 \cdot 10^{-2} \cdot E_Z + 4.986 \tag{B.23}$$

A parabola with coefficients A, B, and C is used to approximate the relationship between k and d_Z. The equations for coefficients A, B, and C are given below. In these equations k_1, k_2, k_3, $d_{Z,1}$, $d_{Z,2}$ and $d_{Z,3}$ are redefined as S1, S2, S3, D1, D2 and D3, respectively.

$$A = \frac{1}{\text{DET}} \cdot (D3 \cdot S2 - D2 \cdot S3 + D1 \cdot S3 - D3 \cdot S1 + D2 \cdot S1 - D1 \cdot S2) \tag{B.24}$$

$$B = \frac{1}{\text{DET}} \cdot (D2^2 \cdot S3 - D3^2 \cdot S2 + D3^2 \cdot S1 - D1^2 \cdot S3 + D1^2 \cdot S2 - D2^2 \cdot S1) \tag{B.25}$$

$$C = \frac{1}{\text{DET}} \cdot (S1 \cdot D2 \cdot D3 \cdot (D2 - D3) + S2 \cdot D3 \cdot D1 \cdot (D3 - D1) + S3 \cdot D1 \cdot D2 \cdot (D1 - D2)) \tag{B.26}$$

, where DET is given by Equation B.27:

$$\text{DET} = D2 \cdot D3 \cdot (D2 - D3) + D3 \cdot D1 \cdot (D3 - D1) + D1 \cdot D2 \cdot (D1 - D2) \tag{B.27}$$

The bond strength can then be calculated as

$$\tau_b = F_{\text{fail}} \cdot (A \cdot d_Z^2 + B \cdot d_Z + C) \tag{B.28}$$

As an example the bond strength of DY-40-4 has been calculated using this method. All the coefficients are listed in Table B.4. Young's modulus for the substrate is taken from Table 2.3, the substrate thickness is listed in Table A.5, and the fracture force is listed in Table 4.4.

Table B.4: Here the measured and calculated values that are used in the final calculation of bond strength for sample Dγ-40-4 are listed. In the first row Young's modulus, the substrate thickness and the measured fracture force are given. In the second row the three k coefficients are listed. In the third row the calculated value of DET, coefficient A, B and C are listed.

$\mathbf{E}_Z$ **[GPa]**	$\mathbf{d_Z}$ **[mm]**	$\boldsymbol{F}_{\mathbf{fail}}$ **[N]**	
114	0.495	5.54	
$\boldsymbol{k}$**(1)**	$\boldsymbol{k}$ **(2)**	$\boldsymbol{k}$**(3)**	
5.903	4.617	3.714	
DET	**A**	**B**	**C**
-0.000432	53.07	-71.32	27.01

Based on these coefficients and constants, the bond strength of DY-40-4 can be calculated as

$$\tau_b = F_{\text{fail}} \cdot (A \cdot d_Z^2 + B \cdot d_Z + C) = 5.54 \cdot (53.07 \cdot 0.495^2 - 71.32 \cdot 0.495 + 27.01) = 26.1\text{MPa} \tag{B.29}$$

C SEM Images

C.1 Solid-State Synthesis of α-BCZT

During the solid-state synthesis of BCZT powder the first batch, α, was scrapped due to wrong composition, particle size and mechanical losses. When the particle size of the powder was within the desired size range the total loss of powder resulted in not enough α-BCZT left for both characterisation, coatings and pellets. The SEM images taken of the powder during the synthesis are given in Figure C.1. The powder was imaged to confirm particle size distribution and to look at the morphology of the powder. The powder was first imaged after the first calcination, then again after the second calcination, and finally after an additional round of ball milling.

For the first four images the powder was added to a piece of carbon tape placed on a stub by carefully placing the tape-covered side into a small pile of powder. Any excess powder was then brushed off. This method might have broken some of the soft agglomerates. For the final images the powder was suspended in ethanol and a droplet was added to the carbon tape. This method probably resulted in more representative images.

In Figure C.1a, Figure C.1c and Figure C.1e larger agglomerates and chunks from broken pellets can be seen. These are mixed with a finer powder. In Figure C.1f the small particles are smaller than 1 µm.

C.2 Mixing of Porcelain Powder and BCZT

SEM images were taken of the BCZT/Dentin powder mixes and of dentin while at NIOM to confirm whether the mixing method resulted in a fairly homogeneous powder mixture or not. The images are shown in Figure C.2, where Figure C.2a and Figure C.2b show the dentin porcelain powder as it is delivered from the supplier. Figure C.2c and Figure C.2d show the distribution between 30/70 wt% γ-BCZT/dentin powder when mixed with a mortar and pestle. The distribution between 50/50 wt% β-BCZT/dentin powder is shown in Figure C.2e and Figure C.2f. The powders were applied to carbon tape by placing the tape covered side of the stub into a pile of powder. The excess powder was blown off with compressed air.

The difference in particle size between the γ-BCZT and β-BCZT powders is very apparent in Figure C.2c and Figure C.2e. The ligther particles in these images are BCZT. It is easy to see that the γ-BCZT has a smaller particle size than the β-BCZT powder. The dentin powder is more similar in particle size to the β-BCZT than the γ-BCZT. The dentin powder consists of both small and large particles, which is visible in Figure C.2a . From these images one can also see that the powder mixes are not entirely homogeneous.

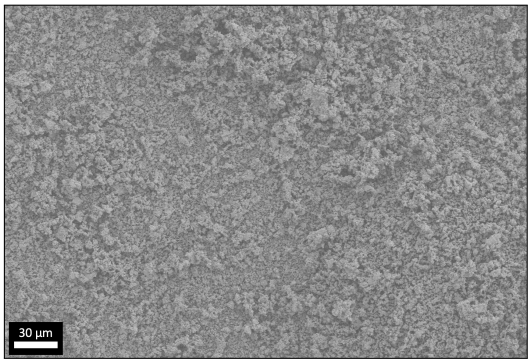

(a) SEM image of α-BCZT powder after the first calcination, taken at 1 000X magnification.

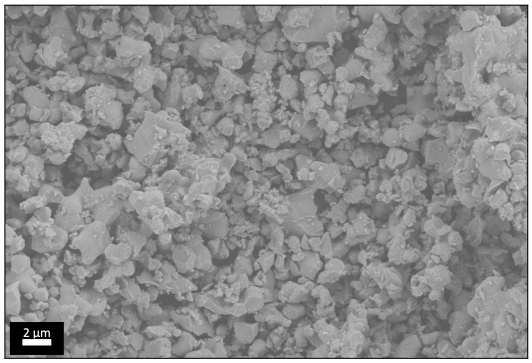

(b) SEM image of α-BCZT powder after the first calcination, taken at 10 000X magnification.

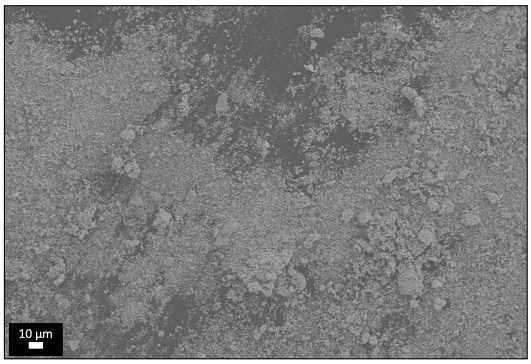

(c) SEM image of α-BCZT powder after the second calcination, taken at 1 000X magnification.

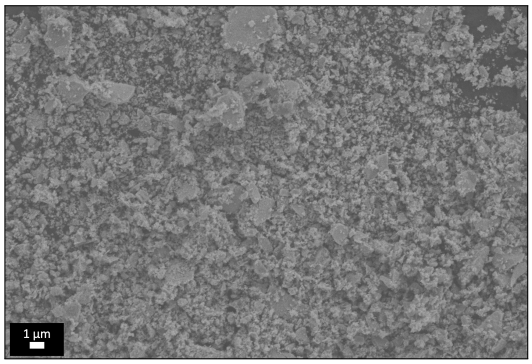

(d) SEM image of α-BCZT powder after the second calcination, taken at 1 000X magnification.

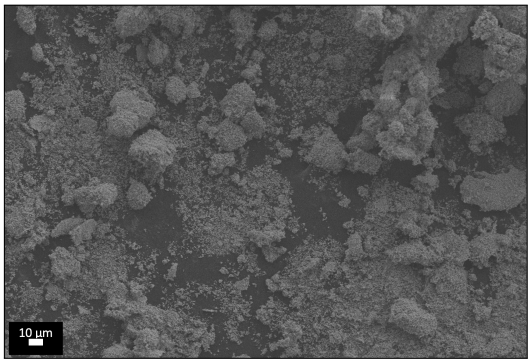

(e) SEM image of α-BCZT powder after the second calcination and an additional 4 hours of milling, taken at 1 000X magnification.

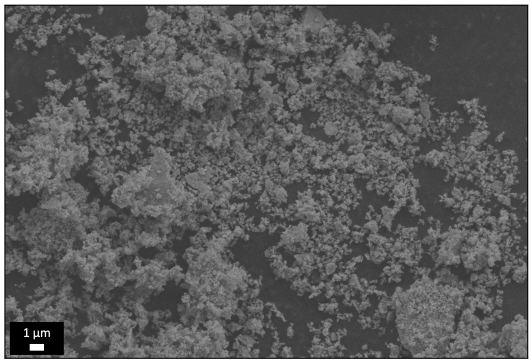

(f) SEM image of α-BCZT powder after the second calcination and an additional 4 hours of milling, taken at 10 000X magnification.

Figure C.1: SEM images of α-BCZT, taken at 1 000X and 10 000X magnification. The images were taken after the first calcination, after the second calcination and after an additional 4 hours of milling.

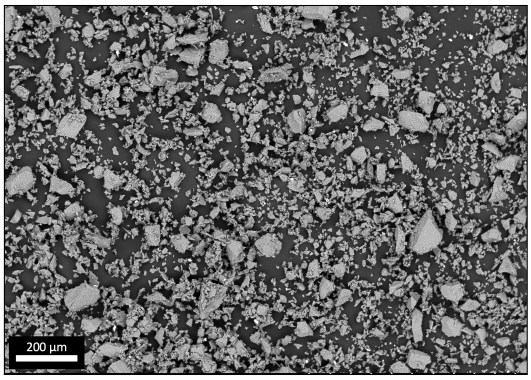

(a) SEM image of the dentin porcelain powder, taken at 100X magnification.

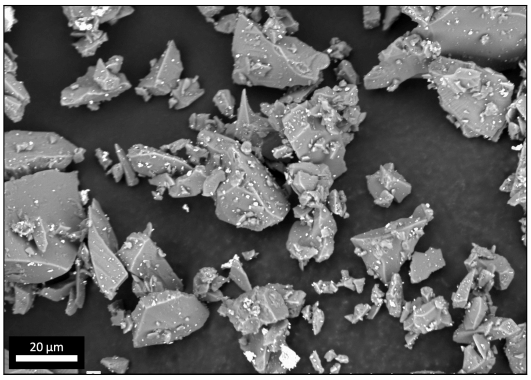

(b) SEM image of the dentin porcelain powder, taken at 1 000X magnification.

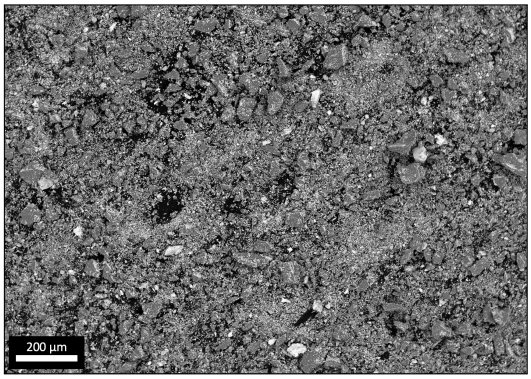

(c) SEM image of the 30/70 wt% γ-BCZT/Dentin powder mix, taken at 100X magnification.

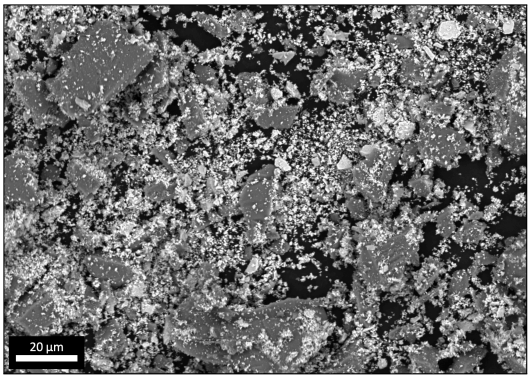

(d) SEM image of the 30/70 wt% γ-BCZT/Dentin powder mix, taken at 1 000X magnification.

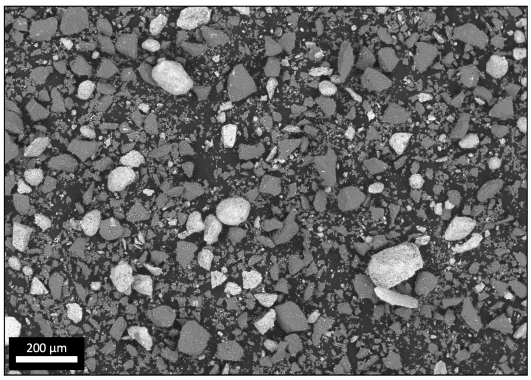

(e) SEM image of the 50/50 wt% β-BCZT/Dentin powder mix, taken at 100X magnification.

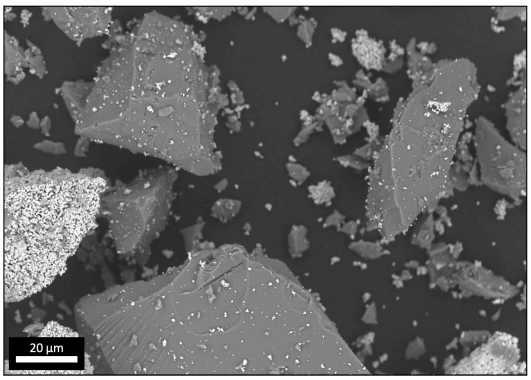

(f) SEM image of the 50/50 wt% β-BCZT/Dentin powder mix, taken at 1 000X magnification.

Figure C.2: SEM images of dentin porcelain powder, of 30/70 wt% γ-BCZT/Dentin powder mix, and of 50/50 wt% β-BCZT/Dentin powder mix.

C.3 Fractured Samples

In this section the SEM images of the fractured samples are given. The imaged samples are D-00-1 (Figure C.3), Dβ-40-1 (Figure C.4), Dβ-50-1 (Figure C.5), Dγ-30-1 (Figure C.6), Dγ-40-2 (Figure C.7), and Dγ-50-1 (Figure C.8). Additionally, Dβ-30-4 was imaged. These images can be found in Figure 4.22.

All the fractures are very similar, going from one end of the coating and various distances into the coating. There is a gap between the lifted coating and the remaining substrate. In most images it is also possible to see that some of the coating is left on the substrate. In Figure C.5b some plastic deformation is visible. It looks like a strand of porcelain has been pulled on and broken during the fracturing process.

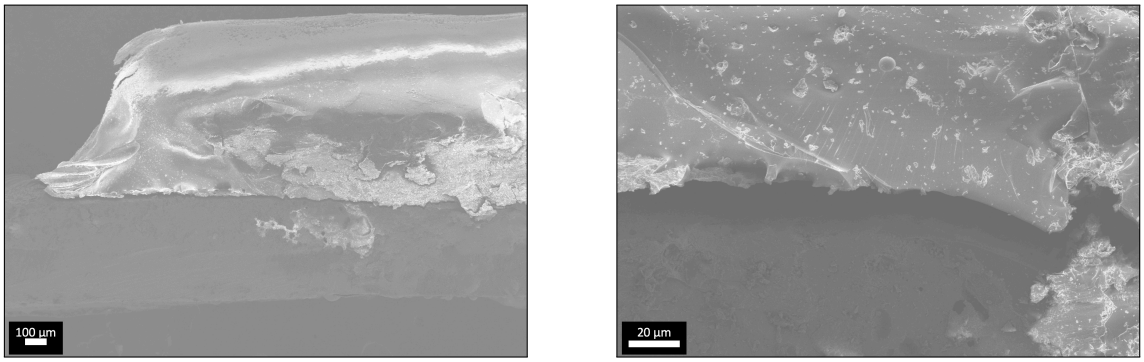

(a) Taken at 150X magnification. **(b)** Taken at 1 750X magnification.

Figure C.3: SEM images of the side profile of D-00-1, showing the fracture resulting from the de-bonding test.

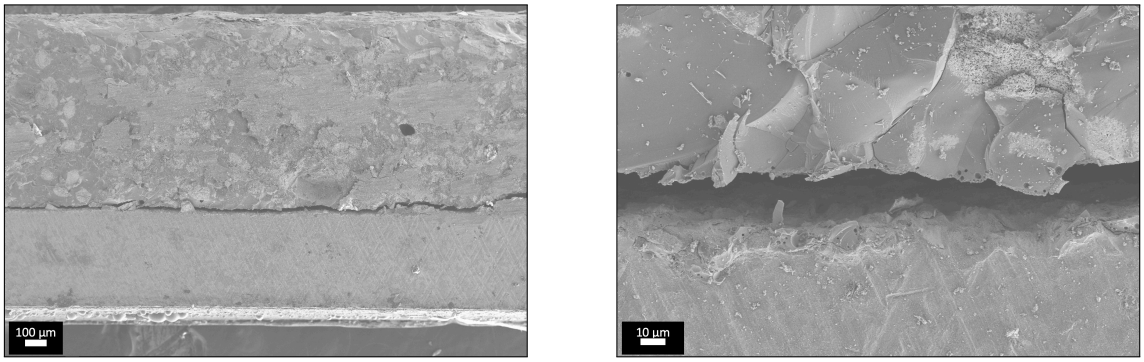

(a) Taken at 150X magnification. **(b)** Taken at 1 750X magnification.

Figure C.4: SEM images of the side profile of Dβ-40-1, showing the fracture resulting from the de-bonding test.

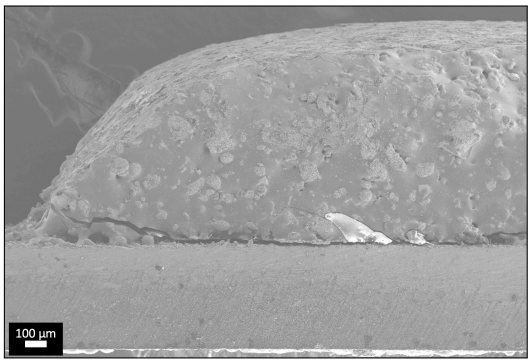

(a) Taken at 150X magnification.

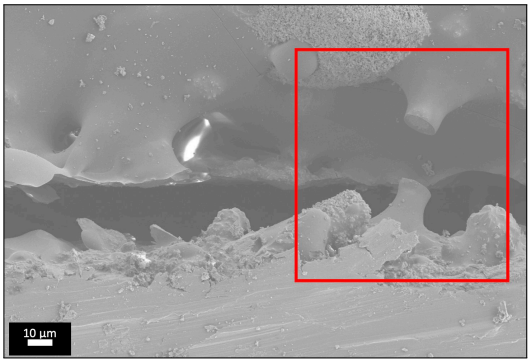

(b) Taken at 1 750X magnification.

Figure C.5: SEM images of the side profile of Dβ-50-1, showing the fracture resulting from the de-bonding test.

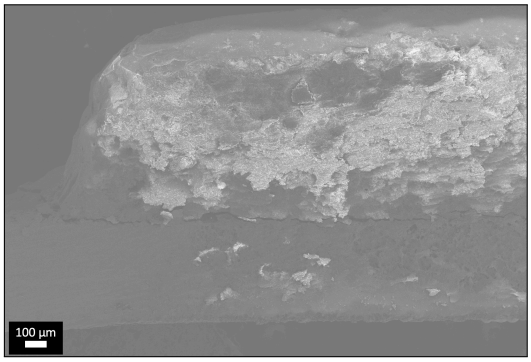

(a) Taken at 150X magnification.

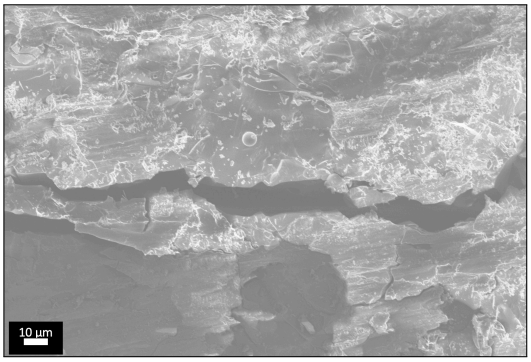

(b) Taken at 1 750X magnification.

Figure C.6: SEM images of the side profile of Dγ-30-1, showing the fracture resulting from the de-bonding test.

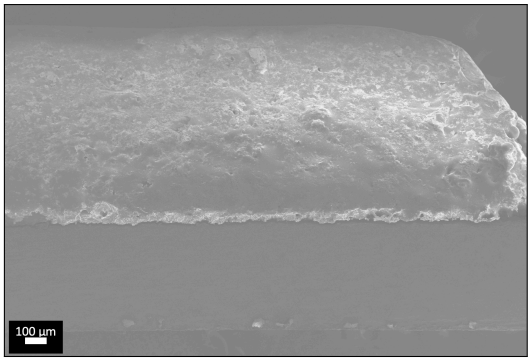

(a) Taken at 150X magnification.

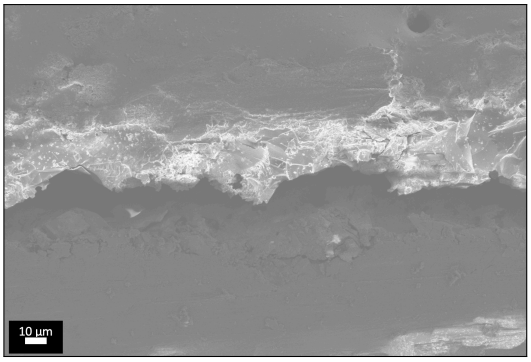

(b) Taken at 1 750X magnification.

Figure C.7: SEM images of the side profile of Dγ-40-2, showing the fracture resulting from the de-bonding test.

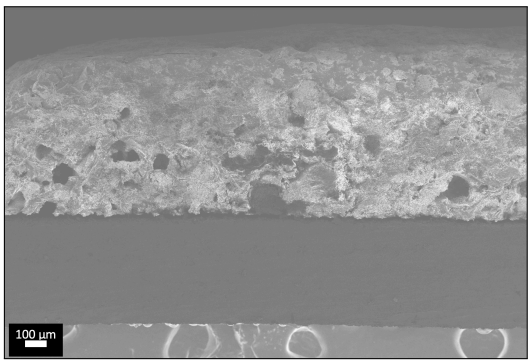

(a) Taken at 150X magnification.

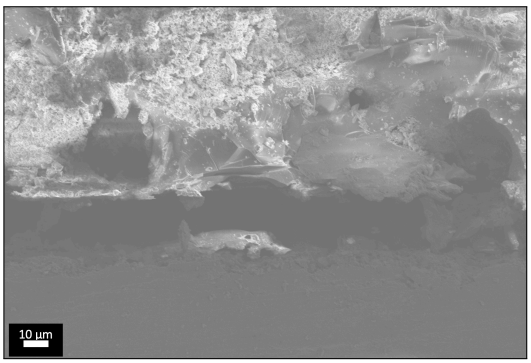

(b) Taken at 1 750X magnification.

Figure C.8: SEM images of the side profile of Dγ-50-1, showing the fracture resulting from the de-bonding test.

C.4 BCZT Pellets

SEM images of Pγ-1 and Pγ-2 are given in Figure C.9. These images better show the topography of the grains on the surface of the pellets. The grains have a wave-like pattern going in different directions. The patterns are not as visible on every grain. There are also small gaps along some of the grain boundaries. The grains are of different sizes and shapes in both pellets, but the pellets overall look quite similar in these images.

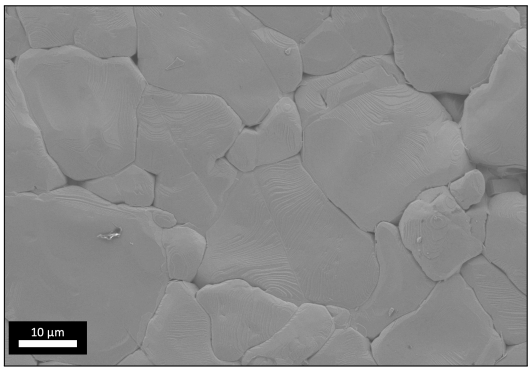

(a) SEM image of Pγ-1, taken at 4000X magnification.

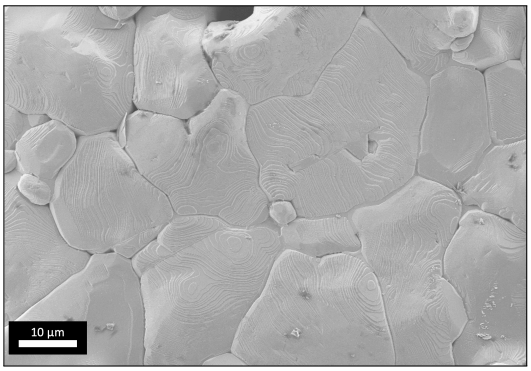

(b) SEM image of Pγ-2, taken at 4000X magnification.

Figure C.9: SEM images of Pγ-1 and Pγ-2, taken at 4000X magnification.

D EDS Analysis

Representative results from the multipoint EDS analysis are given in this appendix. For each sample a multipoint analysis was performed with at least one point in each of the components of the samples. These components are the substrate, the bonder-layer, the BCZT and the dentin phase. SEM images showing the placement of the different points are given in Figure D.1 - D.5 for sample D-00-8, Dβ-30-7 and Dγ-30-11, respectively. The tables generated by the EDS software for these samples are given in Figure D.2, D.4 and D.6, respectively.

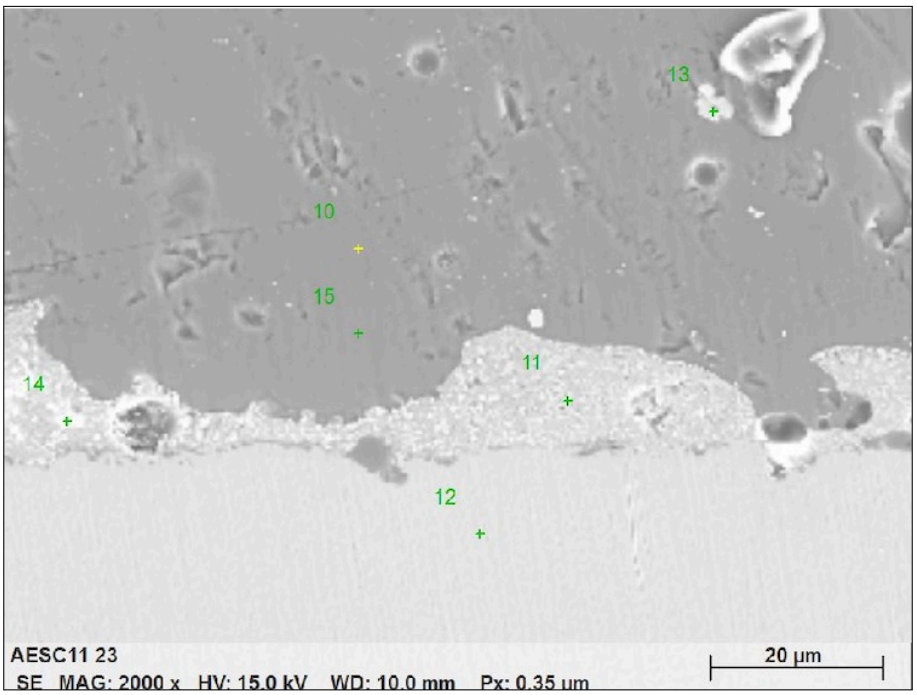

Figure D.1: SEM image showing the points analysed with EDS on sample D-00-8.

Spectrum: 10

El	AN	Series	Net	unn. C [wt.%]	norm. C [wt.%]	Atom. C [at.%]	Error (1 Sigma) [wt.%]
O	8	K-series	50074	23,01	31,77	44,18	2,74
Si	14	K-series	311379	29,38	40,55	32,12	1,25
N	7	K-series	3094	3,51	4,84	7,69	0,63
Na	11	K-series	28183	3,91	5,40	5,23	0,27
Ca	20	K-series	25121	4,71	6,51	3,61	0,17
Al	13	K-series	32413	3,08	4,26	3,51	0,17
K	19	K-series	27999	4,20	5,80	3,30	0,16
F	9	K-series	183	0,08	0,11	0,13	0,06
Zr	40	L-series	1307	0,27	0,38	0,09	0,04
Mg	12	K-series	447	0,05	0,07	0,06	0,03
Ba	56	L-series	511	0,19	0,26	0,04	0,04
V	23	K-series	134	0,04	0,06	0,02	0,03
Ti	22	K-series	0	0,00	0,00	0,00	0,00
C	6	K-series	0	0,00	0,00	0,00	0,00
P	15	K-series	0	0,00	0,00	0,00	0,00
Total:				72,44	100,00	100,00	

(a) Quantitative measurement of the dentine phase (point 10) in sample D-00-8.

Spectrum: 11

El	AN	Series	Net	unn. C [wt.%]	norm. C [wt.%]	Atom. C [at.%]	Error (1 Sigma) [wt.%]
O	8	K-series	54857	11,50	66,68	79,55	1,37
Si	14	K-series	21962	1,18	6,85	4,66	0,08
F	9	K-series	1733	0,72	4,15	4,17	0,17
V	23	K-series	11179	1,79	10,35	3,88	0,08
N	7	K-series	1637	0,39	2,26	3,08	0,10
Ti	22	K-series	9059	1,27	7,39	2,94	0,06
Na	11	K-series	2831	0,29	1,69	1,40	0,05
K	19	K-series	912	0,07	0,39	0,19	0,03
Ca	20	K-series	433	0,04	0,23	0,11	0,03
Mg	12	K-series	12	0,00	0,01	0,00	0,00
Zr	40	L-series	0	0,00	0,00	0,00	0,00
Ba	56	L-series	0	0,00	0,00	0,00	0,00
Al	13	K-series	0	0,00	0,00	0,00	0,00
C	6	K-series	0	0,00	0,00	0,00	0,00
Total:				17,25	100,00	100,00	

(b) Quantitative measurement of the bonder layer (point 11) in sample D-00-8

Spectrum: 12

El	AN	Series	Net	unn. C [wt.%]	norm. C [wt.%]	Atom. C [at.%]	Error (1 Sigma) [wt.%]
Ti	22	K-series	399309	94,22	80,68	81,68	2,74
Al	13	K-series	51400	6,38	5,46	9,81	0,32
Ba	56	L-series	44129	13,79	11,81	4,17	0,43
N	7	K-series	2046	0,94	0,81	2,79	0,20
V	23	K-series	3527	0,92	0,79	0,75	0,06
Si	14	K-series	1513	0,17	0,14	0,25	0,03
Mg	12	K-series	839	0,13	0,11	0,22	0,03
Na	11	K-series	383	0,08	0,07	0,15	0,03
Ca	20	K-series	624	0,09	0,07	0,09	0,03
F	9	K-series	36	0,03	0,02	0,06	0,04
K	19	K-series	295	0,04	0,03	0,04	0,03
Zr	40	L-series	0	0,00	0,00	0,00	0,00
C	6	K-series	0	0,00	0,00	0,00	0,00
O	8	K-series	0	0,00	0,00	0,00	0,00
Total:				116,79	100,00	100,00	

(c) Quantitative measurement of the substrate (point 12) in sample D-00-8.

Figure D.2: Selected quantitative results from EDS analysis of D-00-8. The analysed points are from (a) the dentine phase, (b) the bonder layer, and (c) the metal substrate.

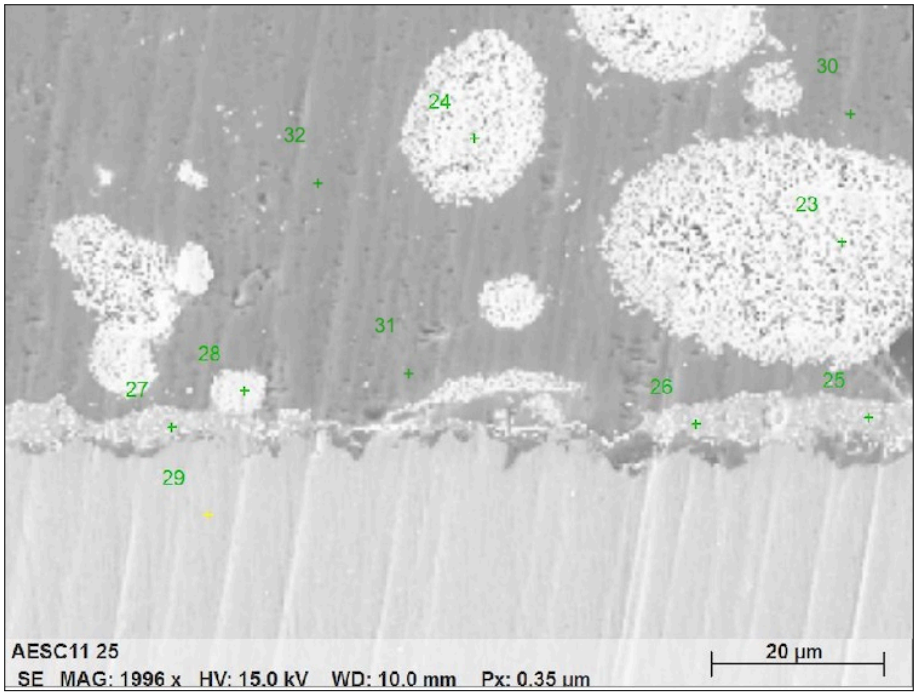

Figure D.3: SEM image showing the points analysed with EDS on sample Dβ-30-7.

Spectrum: 23

El	AN	Series	Net	unn. C [wt.%]	norm. C [wt.%]	Atom. C [at.%]	Error (1 Sigma) [wt.%]
Ti	22	K-series	89075	21,16	22,59	27,15	0,64
Ba	56	L-series	176965	56,89	60,73	25,45	1,66
O	8	K-series	15424	6,44	6,87	24,72	0,88
C	6	K-series	6844	2,79	2,98	14,29	0,44
Ca	20	K-series	20232	3,06	3,27	4,69	0,12
Si	14	K-series	5351	0,96	1,03	2,10	0,07
Zr	40	L-series	9127	2,36	2,52	1,59	0,12
		Total:		93,67	100,00	100,00	

(a) Quantitative measurement of BCZT particles (point 23) in sample Dβ-30-7.

Spectrum: 32

El	AN	Series	Net	unn. C [wt.%]	norm. C [wt.%]	Atom. C [at.%]	Error (1 Sigma) [wt.%]
O	8	K-series	68128	24,98	37,04	51,76	2,91
Si	14	K-series	319484	26,76	39,68	31,59	1,14
Na	11	K-series	28996	3,68	5,46	5,31	0,26
Al	13	K-series	41081	3,28	4,86	4,03	0,18
Ca	20	K-series	24224	4,62	6,85	3,82	0,17
K	19	K-series	27601	4,12	6,11	3,49	0,15
		Total:		67,44	100,00	100,00	

(b) Quantitative measurement of the dentine phase (point 32) in sample Dβ-30-7.

Spectrum: 26

El	AN	Series	Net	unn. C [wt.%]	norm. C [wt.%]	Atom. C [at.%]	Error (1 Sigma) [wt.%]
O	8	K-series	74127	29,21	34,89	73,99	3,38
La	57	L-series	92569	35,00	41,80	10,21	1,04
Sr	38	L-series	76843	16,36	19,54	7,57	0,69
C	6	K-series	2046	1,79	2,13	6,03	0,36
Al	13	K-series	5730	0,80	0,95	1,20	0,07
Na	11	K-series	2601	0,57	0,68	1,00	0,06
		Total:		83,73	100,00	100,00	

(c) Quantitative measurement of the bonder layer (point 26) in sample Dβ-30-7.

Spectrum: 29

El	AN	Series	Net	unn. C [wt.%]	norm. C [wt.%]	Atom. C [at.%]	Error (1 Sigma) [wt.%]
Ti	22	K-series	394788	74,12	82,88	72,04	2,16
C	6	K-series	4803	2,35	2,62	9,09	0,39
V	23	K-series	33815	7,44	8,32	6,80	0,24
Al	13	K-series	40670	3,94	4,40	6,79	0,21
N	7	K-series	3957	1,59	1,78	5,28	0,29
		Total:		89,44	100,00	100,00	

(d) Quantitative measurement of the substrate (point 29) in sample Dβ-30-7.

Figure D.4: Selected quantitative results from EDS analysis of Dβ-30-7. The analysed points are from (a) BCZT particles, (b) the dentine phase, (c) the bonder layer, and (d) the metal substrate.

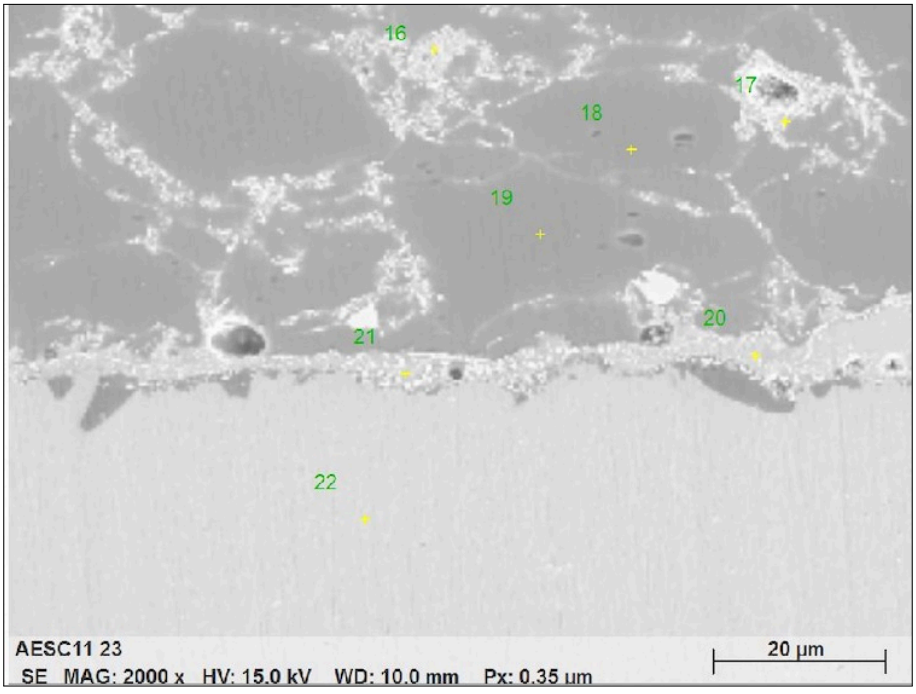

Figure D.5: SEM image showing the points analysed with EDS on sample Dγ-30-11.

Spectrum: 16

El	AN	Series	Net unn. C [wt.%]	norm. C [wt.%]	Atom. C [at.%]	Error (1 Sigma) [wt.%]
O	8	K-series	35378	13,82	14,60	43,54	1,70
Ti	22	K-series	69379	17,24	18,22	18,15	0,53
Ba	56	L-series	146471	49,22	52,01	18,07	1,44
Si	14	K-series	47013	5,54	5,85	9,94	0,26
Ca	20	K-series	19274	3,14	3,32	3,95	0,12
Na	11	K-series	5221	1,18	1,24	2,58	0,10
Zr	40	L-series	16774	3,28	3,47	1,81	0,15
Al	13	K-series	4901	0,66	0,70	1,23	0,06
K	19	K-series	4044	0,56	0,59	0,72	0,05
		Total:	94,64	100,00	100,00		

(a) Quantitative measurement of BCZT particles (point 16) in sample Dγ-30-11.

Spectrum: 18

El	AN	Series	Net unn. C [wt.%]	norm. C [wt.%]	Atom. C [at.%]	Error (1 Sigma) [wt.%]
O	8	K-series	63568	24,47	35,48	50,69	2,86
Si	14	K-series	308522	27,70	40,17	32,70	1,18
Na	11	K-series	25361	3,38	4,89	4,87	0,24
Al	13	K-series	39461	3,39	4,91	4,16	0,18
K	19	K-series	28880	4,31	6,26	3,66	0,16
Ca	20	K-series	23281	4,35	6,31	3,60	0,16
Ba	56	L-series	3750	1,37	1,98	0,33	0,07
		Total:	68,96	100,00	100,00		

(b) Quantitative measurement of the dentine phase (point 18) in sample Dγ-30-11.

Spectrum: 19

El	AN	Series	Net unn. C [wt.%]	norm. C [wt.%]	Atom. C [at.%]	Error (1 Sigma) [wt.%]
O	8	K-series	65102	25,33	36,73	51,70	2,95
Si	14	K-series	316063	27,91	40,47	32,45	1,18
Na	11	K-series	26867	3,52	5,11	5,01	0,25
Ca	20	K-series	24113	4,60	6,68	3,75	0,17
K	19	K-series	28824	4,37	6,34	3,65	0,16
Al	13	K-series	31985	2,74	3,98	3,32	0,15
Ba	56	L-series	1266	0,47	0,69	0,11	0,05
		Total:	68,95	100,00	100,00		

(c) Quantitative measurement of the bonder layer (point 20) in sample Dγ-30-11.

Spectrum: 22

El	AN	Series	Net unn. C [wt.%]	norm. C [wt.%]	Atom. C [at.%]	Error (1 Sigma) [wt.%]
Ti	22	K-series	420532	77,97	90,21	78,35	2,27
Al	13	K-series	52144	5,29	6,12	9,43	0,27
C	6	K-series	4663	2,33	2,69	9,32	0,39
N	7	K-series	2077	0,84	0,98	2,90	0,18
		Total:	86,43	100,00	100,00		

(d) Quantitative measurement of the substrate (point 22) in sample Dγ-30-11.

Figure D.6: Selected quantitative results from EDS analysis of Dγ-30-11. The analysed points are from (a) BCZT particles, (b) the dentine phase, (c) the bonder layer, and (d) the metal substrate.

E Particle Size Analysis Results

The particle size distribution (PSD) of α-BCZT was measured three separate times. Once after the first calcination (Figure E.1a), then after the second calcination (Figure E.1b), and finally after the final ball milling (Figure E.1c). Each time five measurement were made in rapid succession to ensure reproducible results. All the PSD measurements can be seen in Figure E.1.

In Figure E.1a there is one peak around 1 µm and one broader peak around 200 µm. The latter decreases in vol% as the number of measurements increases. This might have been caused by agglomerates sinking to the bottom of the testing chamber and not being measured as the times increases. After the second calcination the PSD is broader and bimodal. In this case the distribution also changes as time passes. Lastly, the PSD after the final ball milling is more narrow, with a mean particle size less than 1 µm. These measurements are also more stable.

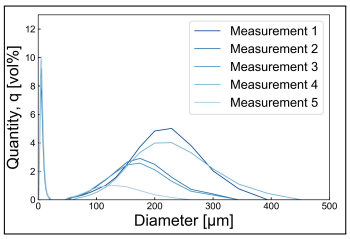

(a) The particle size distribution of α-BCZT powder after the first calcination.

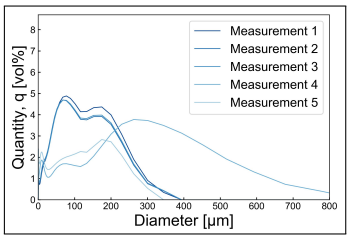

(b) The particle size distribution of α-BCZT powder after the second calcination.

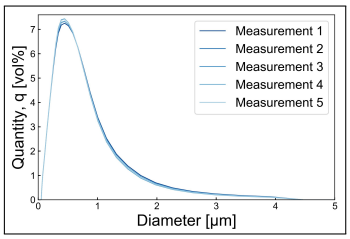

(c) The particle size distribution of α-BCZT powder after the final ball milling.

Figure E.1: The particle size distribution of α-BCZT after the first calcination, the second calcination, and the final ball milling.

The particle size distribution of β-BCZT was measured twice, once after the first calcination and then after the final recalcination. The results of these measurements are given in Figure E.2. The first calcination resulted in a mean particle size around 200 µm, with some unsteadiness in the measurements. After the final calcination the distribution became broader, now including even smaller particles than before. The mean particle size is still around 200 µm.

All five measurements of the PSD of γ-BCZT are given in Figure E.3. The mean particle size is around 1 µm, with some particles as big as 10 µm in diameter.

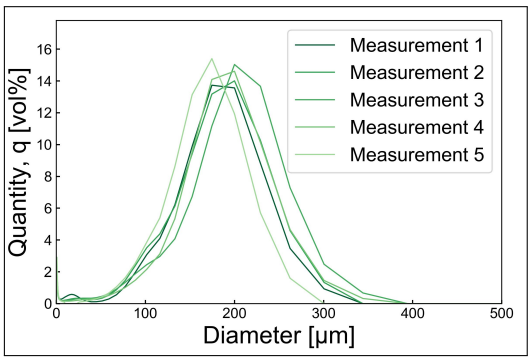

(a) The particle size distribution of β-BCZT powder after the first calcination.

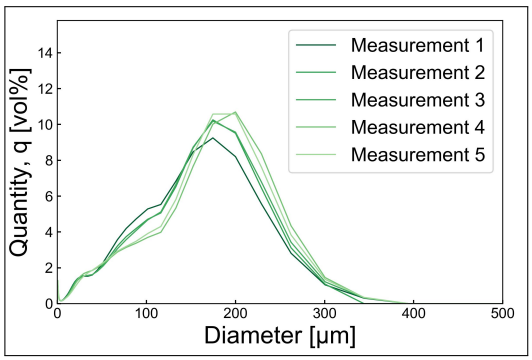

(b) The particle size distribution of β-BCZT powder after the final recalcination.

Figure E.2: The particle size distribution of β-BCZT powder after the first calcination and after the final recalcination.

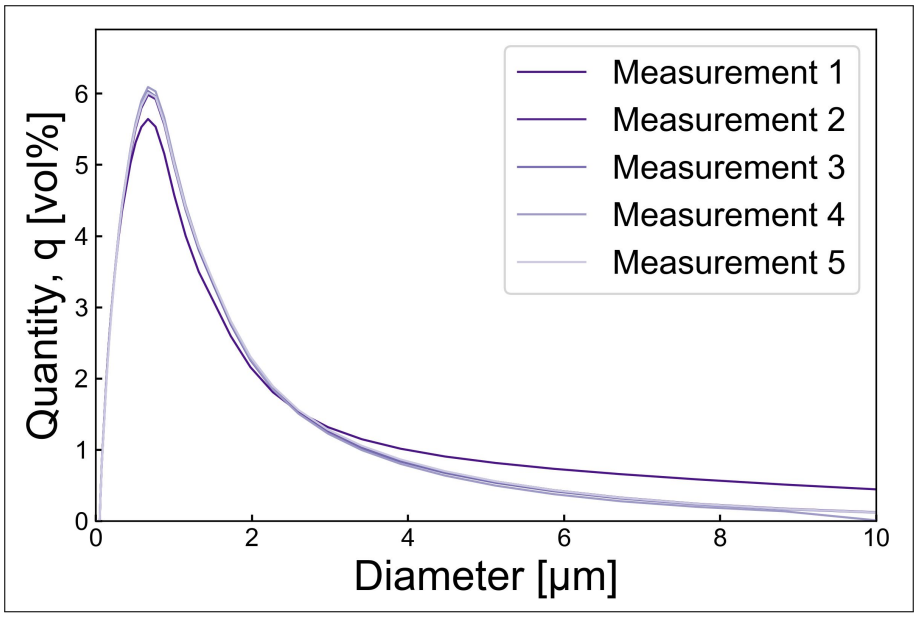

Figure E.3: Particle size distribution of γ-BCZT powder.

F De-Bonding/Crack Initiation Testing

In Figure F.1, F.2 and F.3 the deflection curves from the de-bonding testing are given for each sample. A fracture was measured by the software when there was a 5% decline in force. Where the deflection curve has no such decline the test was manually stopped and the bond strength was not calculated for the sample.

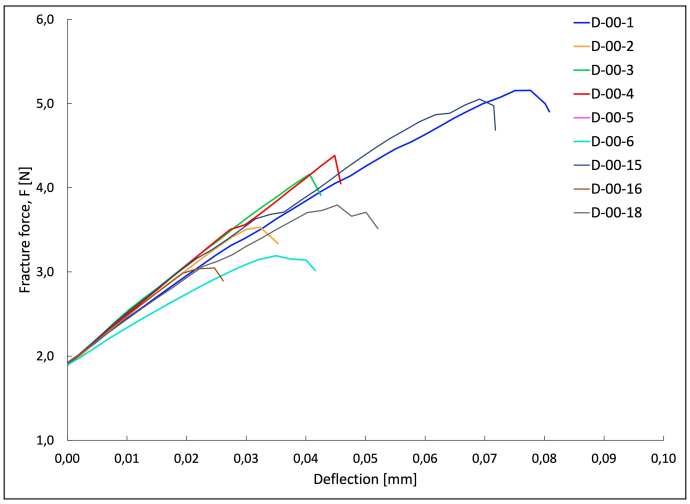

Figure F.1: The deflection curves for coatings with 0 wt% BCZT from the de-bonding/crack initiation test.

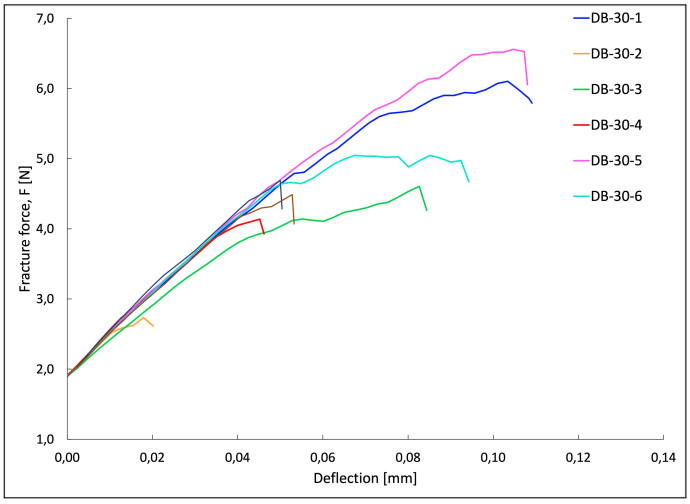

(a) Deflection curves for samples with 30 wt% β-BCZT.

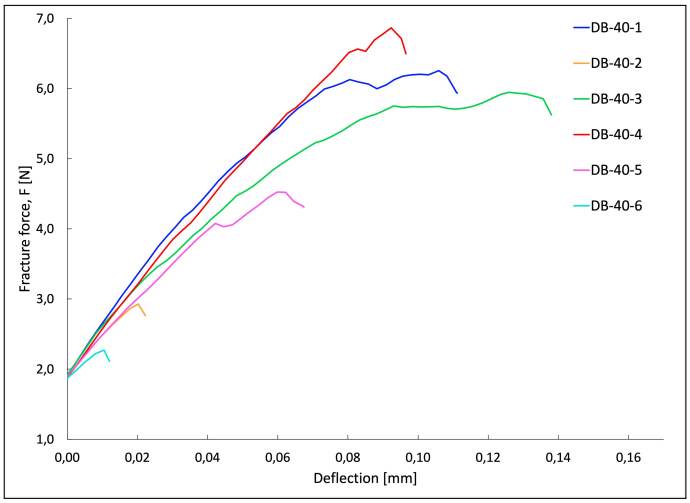

(b) Deflection curves for samples with 40 wt% β-BCZT.

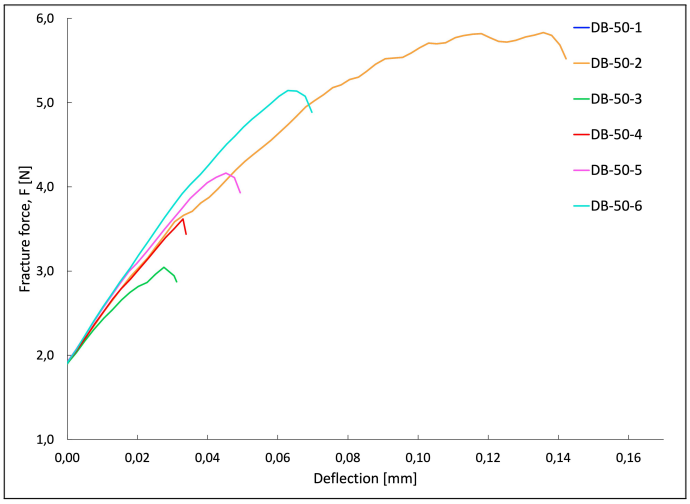

(c) Deflection curves for samples with 50 wt% β-BCZT.

Figure F.2: The deflection curves for coatings with β-BCZT from the de-bonding/crack initiation test.

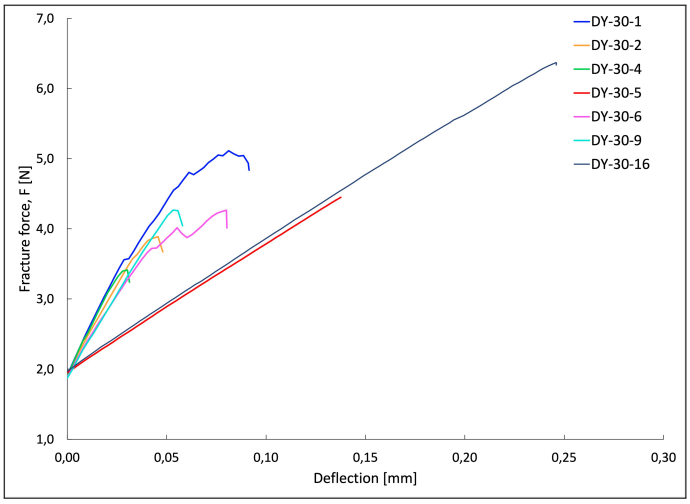

(a) Deflection curves for samples with 30 wt% γ-BCZT.

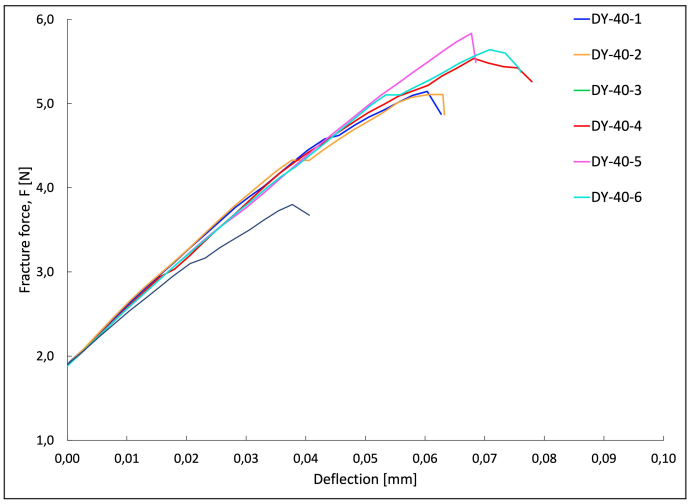

(b) Deflection curves for samples with 40 wt% γ-BCZT.

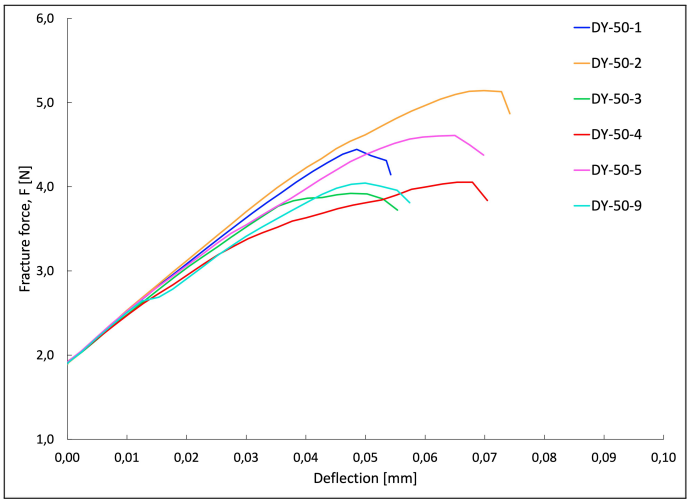

(c) Deflection curves for samples with 50 wt% γ-BCZT.

Figure F.3: The deflection curves for coatings with γ-BCZT from the de-bonding/crack initiation test.

G XRD Analysis

G.1 α-BCZT Powder

A XRD analysis was done on the α-BCZT powder after the first and second calcination to characterise the composition of the powders. The resulting diffractograms are shown in Figure G.1. After the first calcination there are multiple peaks that do not match with the BCZT (PDF) and multiple peaks show peak splitting. After the second calcination a lot of the unwanted peaks are gone, there is also less peak splitting. However, there are still some peaks present that do not belong to BCZT showing that the powder is not pure BCZT.

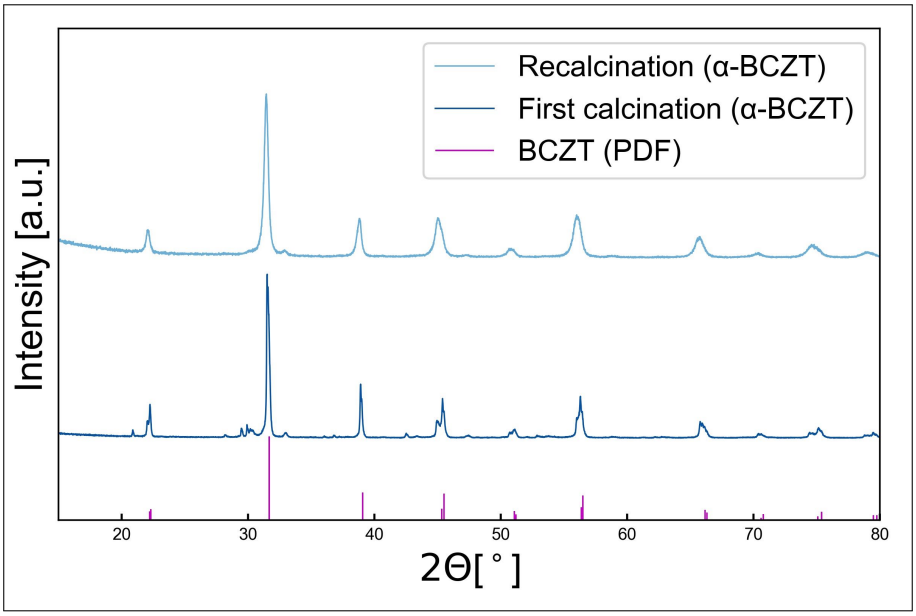

Figure G.1: Diffractograms from XRD analysis of α-BCZT powder after the first and second calcination.

G.2 Precursor Analysis

Because of the unknown peaks in the diffractogram for β-BCZT a XRD analysis was performed on each of the precursor powders used in the solid-state synthesis. This was done to determine whether the peaks originated from the precursors or from secondary, unwanted reactions. In Figure G.2 the diffractograms for the precursors are plotted together with the diffractogram for the final composition of β-BCZT to better compare the different peaks.

None of the precursors match with the unidentified peaks, suggesting that the precursors have either reacted completely during the calcination or they are present in smaller amounts than the instrument is able to measure.

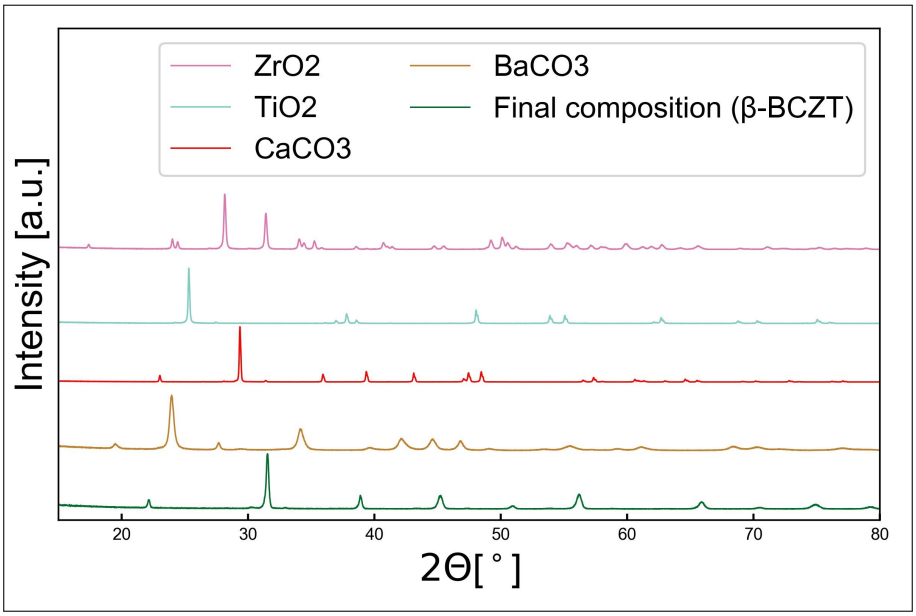

Figure G.2: Diffractograms from XRD analysis of the precursors and β-BCZT.

Martha Seim Gunstad

Development of Piezoelectric Composite Ceramic Coatings on Metal Substrates for Biomedical Applications

NTNU
Norwegian University of
Science and Technology